RELAXATION AND CROSS SECTION EFFECTS IN VALENCE BAND PHOTOEMISSION SPECTROSCOPY

Contents

RELAXATION AND CROSS SECTION EFFECTS IN VALENCE BAND PHOTOEMISSION SPECTROSCOPY

Fenton Read McFeely

Materials and Molecular Research Division
Lawrence Berkeley Laboratory
and
Department of Chemistry
University of California
Berkeley, California 94720

ABSTRACT

Various problems relating to the interpretation of valence band x-ray photoemission (XPS) spectra of solids are discussed. The experiments and calculations reported herein deal with the following questions: 1) To what extent to many-body effects manifest themselves in an XPS valence band spectrum, and thus invalidate a direct comparison between the photoemission energy distribution, I(E), and the density of states, N(E), calculated on the basis of ground-state one-electron theory. 2) The effect of the binding-energy-dependent photoemission cross section on I(E) at XPS energies. 3) In favorable cases indicated by 1) and 2) we examine the effect of the interaction of the crystal field with the apparent spin-orbit splittings of core levels observed in XPS spectra. 4) The use of tight binding band structure calculations to parameterize the electronic band structure from XPS and other data is described. 5) The use of high energy angle-resolved photoemission on oriented single crystals to gain orbital symmetry information is discussed. 6) The evolution of the shape of the photoemission energy distribution (of polycrystalline Cu) as a function of photon energy from $50 \leq h\omega \leq 175$ is discussed.

INTRODUCTION

One of the most fundamental pieces of information one can obtain about a crystal is the energy density of its occupied electronic states. This density of states is given by

$$N(E) = \sum_i \delta(E - E_i)$$

where the summation index i runs over all the occupied orbitals of the system. Having stated the objective, only two obstacles block the golden road to enlightment.

1) N(E), as defined, is impossible to measure experimentally.

2) N(E), as defined, does not exist.

As is evident from the fact that this thesis apparently continues, these difficulties are not so serious as they might first appear. The quantity N(E) does not exist because the one-electron states E_i defining it are not true eigenstates of the crystal Hamiltonian, but rather the eigenstates of an approximate Hamiltonian (e.g. the Hartree-Fock Hamiltonian or, in practice, some approximation to it).

It is with respect to this approximation of separability into one-electron states that N(E) is defined. The one-electron orbitals do, however, have a physical interpretation; if the self-consistent field in which the N electrons move is uneffected by the removal of an electron from orbital i, the energy required to remove it is $|E_i|$. This result is known as Koopmans' theorem. If Koopmans' theorem is an adequate approximation, N(E) is equal to the density of ionization potentials of the crystal, and it is ionization potentials that are

measured by photoemission spectroscopy. Chapter I deals with the importance of deviations from Koopmans' theorem behavior (which are generally referred to as Relaxation effects) in XPS valence band spectra.

Unfortunately, XPS spectra are not direct measures of the energy densities of ionization potentials in question. Within the one-electron approximation the intensity of a photoemission spectrum at initial state energy E_i and photon energy $\hbar\omega$ is given by

$$I(E_i, \hbar\omega) = \sum_{i,F} \delta(E - E_i) \quad \delta(E - E_i - \hbar\omega) \quad |W_{iF}|^2$$

where W_{iF} is the dipole matrix element connecting an occupied initial state i with an empty final state F at energy $E_i + \hbar\omega$. In this equation we have further neglected the details of the propagation of the excited electron to the surface of the crystal and its escape into vacuum.

It is thus clear that even within the "frozen orbital" approximation, the photoemission intensity represents a convolution of occupied and unoccupied densities of states, weighted by matrix elements. In Chaper II experiments are presented and discussed for photoemission in the high-energy, or XPS, limit. Here the density of final states is effectively constant and comparisons of I(E) with theoretical N(E) curves allows the extraction of orbital symmetry information for the solid. In Chapter III the effects of the angular dependence of W_{iF} in experiments performed on oriented single crystals in the high energy limit are discussed, and in Chapter IV we discuss the nature of the onset of this limit for angular integrated experiments.

In Chapters V and VI we discuss two related problems. First we consider the effect of the crystal field on the apparent spin-orbit splitting of core level peaks. Second we attempt, with the aid of other data, to use the XPS spectrum to "work backwards" and determine a reasonable model for the band structure of Pb.

The specific experimental details of each experiment is discussed in the chapter pertaining to it. For a general description of the apparatus used, the reader is referred to the thesis of S. P. Kowalczyk.

I. MANY-BODY EFFECTS IN X-RAY PHOTOEMISSION FROM MAGNESIUM*

Abstract

X-ray photoemission experiments were performed on samples of magnesium and aluminum prepared with atomically clean surfaces in ultra-high vacuum. Core-level binding energies were in excellent agreement with x-ray emission data. Asymmetries in core-level peaks were observed and are compared with theory. The Mg KLL Auger spectrum showed kinetic energies higher than the literature values. Many-body effects, in the form of extra-atomic relaxation, were present in core levels and Auger lines. Both KL_1V and $KL_{23}V$ Auger peaks of Mg were observed. Many-body effects were also manifest as rich plasmon satellite structure accompanying every primary peak. The valence-band spectrum was compared with x-ray emission data and with the $KL_{23}V$ peak. The spectra were interpreted in terms of energy-level diagrams rather than one-electron "levels". It is argued that valence-band spectra obtained by different methods can be compared most directly among states with the same number of core holes. A hierarchical classification of hole states is suggested. The effect of the degree of localization of the hole-state on the relaxation energies in metals is discussed and shown to be small. Finally it was observed that in several light metals the energies required to remove a valence-band electron or a unipositive ion core are about equal.

---

* Work performed in collaboration with L. Ley, S. P. Kowalczyk, J. O. Jenkin, and D. A. Shirley, published in Phys. Rev. B11, 600 (1974).

A. Introduction

Photoemission from a metal is manifestly a many-body process, but the observed spectral features are usually labeled in terms of one-electron quantum numbers. When interpreting photoemission spectra it is important not to take the one-electron labels so literally as to neglect the omnipresent many-electron effects. Accordingly this chapter, which reports a high-resolution x-ray photoemission study of magnesium (and a partial study of aluminum) under ultra-high vacuum conditions, is cast in a format that emphasizes the interplay between one-electron and many-electron aspects of each spectral feature. The advantage of this complementary point of view is underscored in most instances by superior agreement between theory and experiment when both aspects are considered.

Experimental procedures and results are given in Section B. "One-electron" binding energies of core levels are discussed in Section C, with emphasis on many-electron relaxation effects. Asymmetries of these peaks are discussed and compared with theory. Auger peaks, which involve two-hole states, are discussed in Section D, with relaxation effects again stressed. In Section E the valance band densities of states from photoemission, x-ray emission, and KLB spectra are compared. Finally, hole-state localization is reported in Section F.

B. Experimental Procedures and Results

These x-ray photoemission experiments were carried out in a Hewlett-Packard 5950A ESCA Spectrometer that had been modified for ultra-high-vacuum operation. Samples with atomically clean surfaces were prepared by vacuum evaporation of 99.95% pure magnesium or 99.99% pure aluminum

in a sample preparation chamber having a base pressure of 3×10^{-9} Torr, followed by rapid transfer in vacuo to the analyzer chamber, which was maintained at 6×10^{-11} Torr, as measured on a nude Bayard-Alpert ion gauge. Photoemission was achieved by irradiating the sample with monochromatized $AlK\alpha_{1,2}$ x-rays (1486.6 eV).

Spectra covering the electron kinetic-energy range 200-1500 eV were taken first to insure sample purity. In addition to photoelectron lines expected from the atomic levels of Mg, there were KLL and KLV Auger lines in the 1050-1250 eV region. Also present were characteristic energy loss (plasmon) satellites associated with every line. The full-energy spectrum provided an effective in-situ chemical analysis of the first few atomic layers of the sample: i.e., those from which the electrons that appear in the full-energy lines are ejected. The absence of any lines that could be attributed to Mg indicated the absence of any impurities in high concentrations. A careful study of the kinetic energy regions where the C(1s) and O(1s) peaks would be expected allowed us to set upper limits of 0.3 monolayers on the amount of each of these two elements present. Additional evidence for the surface cleaniness of the sample comes from two sources: the observation of a well-formed surface plasmon peak and the absence of oxide satellites on core-level peaks. Similar comments apply to the Al sample. Only the positions and shapes of the Al 2s and 2p core levels will discussed in this chapter, for comparison with the Mg results. Characteristic binding energies or kinetic energies are given and discussed separately in the appropriate sections below.

C. Core-Level Spectra

The 1s, 2s, and 2p spectra of Mg are shown in Fig. 1. The core-level binding energies relative to the Fermi energy are denoted E_B^F. They are set out in Table I. Also given are values from an atomic energy level compilation by Bearden and Burr[1] and the $E_B^F(2p)$ value of 49.5 ± 0.1 eV which we have read from the x-ray spectrum published by Neddermeyer[2] (the ±0.1 eV error was assigned by us: it is our estimate of the uncertainty entailed in defining the Fermi energy E_F). The values of E_B^F from Ref. 1 are less accurate than ours, but more importantly they are higher by from 0.85 to 2.4 eV for the 1s, 2s, and 2p levels, while Neddermeyer's value for $E_B^F(2p)$ agrees within the 0.1 eV errors. We believe that this difference can be attributed to oxidation of the surface of the magnesium samples used in the earlier photoemission experiments from which Bearden and Burr's values were derived. Siegbahn, et al.,[3] emphasized the importance of this problem for active metals, and indicated that shifts of ∿2 eV in binding energy may be observed on oxidation. The recent photoemission results of Tejeda et al.[4] on clean surfaces agree with ours.

A good test of the accuracy of the photoemission binding energies is given by comparing them with x-ray energies in magnesium. X-ray energies are measured on bulk material and are therefore not sensitive to surface oxidation. An energy-level diagram that illustrates the connection between x-ray emission and x-ray photoemission energies is shown in Fig. 2. This diagram depicts the hole-state energy-level spectrum that is generated by ejecting an electron from a 1s, 2s, 2p, or valence-band orbital in magnesium. The levels are the true many-particle

energy levels of the system, with many-body relaxation energies, etc., included. The energies of these levels above the ground state are equal to the one-electron binding energies relative to the "vacuum level", E_B^V. Since the binding energy of an electron at the Fermi energy E_F is just the work function, ϕ, it follows that the binding energy of a core level i relative to E_F is given by

$$E_B^F(i) = E_B^V(i) - \phi \quad . \tag{1}$$

In our experiments the Fermi edge was clearly evident in the valence-band spectrum, so $E_B^F(i)$ was measured directly.

The energies of characteristic x-rays are given by the differences between pairs of binding energies. Thus, for example,

$$\begin{aligned} \Delta E(K\alpha_{12}) &= E_B^V(1s) - E_B^V(2p) \\ &= E_B^F(1s) - E_B^F(2p) \quad . \end{aligned} \tag{2}$$

Thus x-ray photoemission energies can be compared directly with x-ray emission energies. The values of E_B^F obtained in this work show excellent agreement with x-ray values, as indicated by columns 6 and 7 of Table I. Thus all three of our core-level energies for Mg--1s, 2s, and 2p--are in complete agreement with x-ray values.

The Al 2s and 2p binding energies agree only fairly well with x-ray values. This is attributed in part to the difficulty of assigning a consistent Fermi energy, and probably in part to an erroneous x-ray value for the 2s-2p transition.

The effect of surface oxidation on apparent core-level energies is illustrated in the right side of Fig. 2. The more positive environment of core-hole states in oxidized magnesium atoms increases the binding energies of these states relative to the reference energy E_F. The latter is unshifted in the surface-oxidized sample if no charge buildup occurs. Thus the apparent binding energies will be too large, as observed in the earlier Mg work (Table I, column 3).

Figure 3 shows the conventional ground-state one-electron "energy-level" diagram that has been used traditionally in discussing both x-ray emission and photoemission data.[5a,b] Since these one-electron "levels" do not really exist, this type of diagram is of course only an approximation to reality. As such, it can be very useful in discussing gross structure, such as the identities of transitions. In explaining subtle effects such as chemical shifts or many-body relaxation energies, however, in both of which the final state plays a large role, diagrams such as Fig. 3 are inadequate or even misleading. The reader can easily verify this statement by attempting to interpret the results reported in this chapter using Fig. 3. We therefore advocate using diagrams like Fig. 2, which depict the true energy levels of the system. Parratt[5c] has discussed this point in more detail.

The measured core-level binding energies are in good agreement with theory. To make the comparison we must first add to $E_B^F(i)$ the measured work functions ϕ = 3.7 eV for Mg and 4.2 eV for Al[6] to obtain the "vacuum" binding energy $E_B^V(i)$, according to Eq. (1). The values of $E_B^V(i)$ so obtained are listed in Table II. Theoretical core-level binding energies for free atoms, $E_B^A(i)$, are also listed. These values were calculated by

by Siegbahn, et al.[7] using an optimized Hartree-Fock-Slater approach devised by Rosén and Lindgren.[8] As relativistic hole-state calculations, these $E_B^A(i)$ values contain every sizable effect except electron correlation. A fairly accurate estimate of correlation effects on the 1s and 2s binding energies can be obtained by simply using results of Verhaegen, et al.[9] and of Moser, et al.,[10] for neon binding energies. Atomic binding energies of Mg and Al corrected in this way for correlation in the 1s and 2s cases, are listed as $E_B^A(i,corr)$ in Table II. These estimates of the atomic binding energies are believed to be accurate to 1.0 eV or better.

Comparison of the best estimates of the core-level binding energies in free atoms, $E_B^A(i,corr)$ (Table II, Col. 3) with the experimental values $E_B^V(i)$ for metallic Mg and Al (Table II, Col. 6) shows the latter to be lower by 4-8 eV. This is attributable to a <u>many-body</u> effect: the extra-atomic relaxation of conduction-band states toward the core-hole state during photoemission to form a semi-localized exciton state in which the positive charge of the hole is shielded.[11] A theoretical model that estimates the core-level binding-energy shift due to extra-atomic relaxation in terms of atomic two-electron integrals was described earlier.[12] Application of this model to Mg, for example, gives the estimates of extra atomic relaxation energies due to the hole-state polarization potential

$$\langle 1s|V_p^{ea}|1s\rangle_{Mg} \cong [F^0(1s,3p) - \tfrac{1}{6}\,G^1(1s,3p)]_{Al}$$

$$\langle 2s|V_p^{ea}|2s\rangle_{Mg} \cong [F^0(2s,3p) - \tfrac{1}{6}\,G^1(2s,3p)]_{Al}$$

$$\langle 2p|V_p^{ea}|2p\rangle_{Mg} \cong [F^0(2p,3p) - \tfrac{1}{6}\,G^0(2p,3p) - \tfrac{1}{15}\,G^2(2p,3p)]_{Al} \quad .$$

Similar expressions apply to Al. The binding energy shifts are then given by

$$E_B^V(\text{theo}) \cong E_B^A - \frac{1}{2}\langle V_p \rangle \quad . \tag{3}$$

Relaxation-energy shifts, estimated using this model and Mann's integrals,[13] are given in Table II, column 4. Column 5 lists theoretical estimates of E_B^V in Mg metal, after correction for this many-body screening effect. These values are to be compared to the experimental results in column 6. Considering the estimated accuracy of ±1.0 eV in $E_B^A(\text{corr})$ and the approximate nature of our relaxation model, the agreement is gratifying. Comparison of columns 3, 5, and 6 in Table II underlines the importance of extra-atomic relaxation and supports the above model as a reasonably accurate method for estimating the size of this effect.

D. Auger Spectra

1. The KLL Auger Spectrum

Figure 5 shows the rich KLL Auger Spectrum of Mg, observed in the 1050-1250 eV kinetic energy range. This spectrum is superficially very different from the KLL Auger spectrum of Mg reported by Siegbahn, et al.[14] The differences can easily be understood, however, as arising from a rich plasmon spectrum present in Fig. 4 but absent in the earlier work, plus a shift of +5 eV in kinetic energy in our spectrum. This result is expected because the earlier work did not employ ultra high vacuum; thus the Mg surface must have been oxidized. This would account for both the absence of plasmons and the lower kinetic energies in the earlier work.

Using the relative kinetic energies reported for the various Auger peaks by Siegbahn, et al.,[14] together with the known plasmon energies and relative intensities (see Sec. VI), it is possible to locate all five Auger peaks corresponding to those reported by Siegbahn, et al. The KL_2L_3 (^1D), KL_1L_2 (^1P) and KL_2L_2 (^1S) assignments are obvious, while the KL_1L_1 (^1S) and KL_1L_3 (^3P) assignments follow from the anomalous intensities of the plasmon peaks with which they coincide. Derived energies are given in Table IV. Also given are the earlier values of Siegbahn, et al.[14] and a set of theoretical values that they calculated for free atomic Mg.

In comparing Auger energies in a metal with free-atom values, the relation

$$E^F(KLL) = E^A(KLL) + \phi + R_e(TA) \quad , \tag{4}$$

is expected to hold for each Auger component.[15] Here

$$E^A(KLL) = E^A(K) - E^A(LL) \quad ,$$

is the energy difference between the initial K-hole state and the final LL-hole state in the free atom, $E^F(KLL)$ is the Auger kinetic energy relative to E_F, and $R_e(TA)$ is the total Auger extra-atomic relaxation energy that results from differences in the screening-energy shifts of the two-hole and one-hole states that arise in the metal, as indicated in Fig. 6. Rearranging Eq. (4) we have

$$\begin{aligned} R_e(TA) &= E^F(KLL) - \phi - E^A(KLL) \\ &= E^V(KLL) - E^A(KLL) \quad , \end{aligned} \tag{5}$$

where $E^V(KLL)$ represents the Auger energy relative to the vacuum level. Values of $R_e(TA)$ derived from this relation are listed in Table III.

To estimate theoretical values of $R_e(TA)$ we can use the model described by Kowalczyk, et al.,[15] in which the screening energy was approximated by atomic two-electron integrals. Applying that model to magnesium, we estimate $R_e(TA)$ as

$$R_e(TA)_{Mg} \cong 2\, f\ (2p\ 3p)_{Si} - \frac{1}{2}\, f\ (1s\ 3s)_{Al} \quad . \tag{6}$$

Here the equivalent-cores approximation has been used to estimate the two-electron integrals in the presence of core-level holes. This equation applies specifically to KLL' lines in which both the L and L' holes have 2p character. Other, similar, equations would describe $R_e(TA)$ for 2s-hole cases. In Eq. (6) the f terms describe two-electron multiplet interactions, as discussed in detail elsewhere. They have the form

$$f(2p\ 3p) = F^0(2p\ 3p) - \frac{1}{6}\, G^0(2p\ 3p) - \frac{1}{15}\, G^2(2p\ 3p) \quad , \tag{7}$$

etc. Mann's two-electron integrals were used for numerical estimates of $R_e(TA)$. Results are given in the last column of Table III. These theoretical estimates are larger than the experimental values by factors of 1.3 to 1.8. This level of agreement is similar to that found earlier for other elements.[15] It indicates that the screening model is qualitatively correct, but that the screening valence electrons are, as expected, less localized in the metal than in the free atom.

2. KLV Auger Lines

Two additional low-intensity groups of peaks were observed slightly above the KLL group in kinetic energy (Fig. 5). We interpret these as

arising from the KL_1V and $KL_{2,3}V$ Auger transitions plus their plasmon satellites. The mean $KL_{2,3}V$ transition energy is 1251.1 eV. Combining this with the one-electron K,L_{23}, and valence-band binding energies, we have[15]

$$E^F(KL_{2,3}V) = E_B^F(K) - E_B^F(L_{23}) - E_B^F(V) - f(2p_c 3s_v) + R_e \quad . \quad (8)$$

Here $f(2p_c 3s_v)$ is the interaction energy between the 2p core hole and the 3s (valence-band) hole, and R_e is the extra-atomic relaxation energy arising from the interaction with the 3s hole of the screening charge attracted by the 2p hole, or vice versa. It is <u>not</u> the same as $R_e(TA)$, because part of $R_e(TA)$ is included in the empirical core-level binding energies. In fact $R_e \cong \frac{2}{3} R_e(TA)$.[15] Using $E^F(KL_{2,3}V) = 1251.1$ eV, $E_B^F(K) = 1303.0$ eV, $E_B^F(L_{23}) = 49.4$ eV, and $E_B^F(V) = 2.5$ eV (an average value), we find

$$R_e - f(2p_c 3s_v) = 0.0 \text{ eV} \quad .$$

This result states that interaction energy between a 2p and a 3s hole in the $KL_{23}V$ final state is equal to that between one of these holes and the screening charge. It is not clear <u>a priori</u> to what extents the 3s hole and the screening charge are localized, but this result shows that the two must be localized to a similar degree. If both were completely localized in 3s atomic orbitals, then $f(2p_c 3s_v)$ would be given by

$$f(2p_c 3s_v) \cong [F^0 - \tfrac{1}{6} G^1(2p\ 3s)]_{Al} = 12.5 \text{ eV} \quad ,$$

where Mann's integrals[13] were used for the numerical estimate. If the

3s hole and the screening charge were completely delocalized, R_e and $f(2p_c 3s_v)$ would of course be much smaller.

There is independent evidence for the localized nature of the screening charge accompanying a 2p hole in Mg. In an earlier discussion[11] and (more accurately) from Table II, we found that the Mg(2p) binding energy was reduced by 3.2 eV in the metal relative to the free atom. This is interpreted as arising from dynamic extra-atomic relaxation due to screening. The corresponding static term would be twice as large, i.e., $R_e \cong 6.4$ eV. The large size of this term--about half the above atomic estimate--indicates that the screening charge associated with a 2p hole state in Mg is "semilocalized", in agreement with earlier conclusions.[11] Thus $f(2p_c 3s_v) \cong 6.4$ eV in the $KL_{23}V$ final state, implying that the valence-band hole in this state is also partially localized on the Auger-active atom.

E. Comparison of Valence-Band Spectra

It is instructive to compare the shapes of the $KL_{23}V$ Auger peak with that of the valence-band peak in the x-ray photoemission spectrum and with the L_{23} x-ray emission profile, as all three peak shapes are determined by the valence-band density of states. To facilitate this comparison we note that the local density of states "on" a magnesium atom will be different when there is a core hole present than in the unperturbed metal. The excited hole states of the system can therefore be classified naturally according to the number of core hole states and valence-shell hole states present. This is illustrated in Fig. 6, in which states are labeled according to the type of hole present (e.g., $\bar{1}s$) and the core- and valence-hole "quantum numbers" C and V. The

valence-band (local) density-of-states profile will be different for the C = 1 states than for C = 0 states because the core hole attracts a screening charge. We shall denote the density of states in the C = 1 level as $\rho_1(E)$ and in the C = 0 levels as $\rho(E)$. In this notation the selection rules are $\Delta(C + V) = 0$ for x-ray transitions and $\Delta(C + V) = +1$ for photoemission and Auger emission, with the former going upward and the latter downward in energy. The transitions with which we are concerned in Mg are shown in Fig. 7.

Valence-band photoemission to the $\overline{3}s(01)$ state proceeds within the C = 0 manifold: therefore it can in principle measure $\rho(E)$, in the approximation that effects such as cross-section variation across the band and differential final-state relaxation may be ignored. By this agrument the experimental spectrum of the Mg valence bands (Fig. 7 top panel) should give a good representation of $\rho(E)$. We shall defer a discussion of whether or not it does, pending the outcome of cross-section calculations currently underway. We note that the experimental spectrum does not have the simple shape that would naively be expected on the free-electron model; viz, a monotonic increase of intensity with energy to E_F and a sharp drop at E_F.

The $L_{2,3}$ x-ray emission spectrum of Neddermeyer[2] is reproduced in Fig. 7 (middle panel). The sharp peak at E_F in this spectrum has been variously attributed to a many-body effect--the Mahan anomaly--or to (one-electron) band-structure effects. There is no evidence whatever for such a peak in the photoemission spectrum (the 0.55 eV FWHM instrumental resolution of our spectrometer would broaden such a peak if it were present, but could not obscure it completely). This does not

necessarily mean that the peak could not be a band-structure effect, because the "local density-of-states" profile studied in the XPS experiment is that of the C = 0 states, with no core hole present. If variations in relaxation energy and cross-section effects across the band can be ignored, XPS would therefore yield $\rho(E)$. Under similar assumptions XES would give $\rho_1(E)$, since C = 1 in the initial state (the 2p hole state) in this case.

A better comparison can be made between the L_{23} XES spectrum (Fig. 7, middle panel) and a $KL_{2,3}V$ Auger line (Fig. 7, lower panel). In the $KL_{23}V$ Auger transition, both initial and final states belong to the C = 1 manifold. Thus, again neglecting cross-section and relaxation variation across the band, this line should measure $\rho_1(E)$, as does the XES spectrum.

The $KL_{23}V$ peak has approximately the same width as the other valence-band peaks (6-7 eV). Like them, it is relatively steep on the high-kinetic-energy (Fermi edge) side. It shape differs in detail from those of the XPS and XES peaks, however. It shows no strong evidence for a peak at the Fermi edge (a shoulder is present), thus suggesting that the XES peak is a collective effect rather than a density-of-states effect. In addition, the $KL_{2,3}V$ Auger peak is more peaked about 2 eV below the Fermi edge than are the XPS or XES peaks. We interpret this as evidence that the 2p hole state tends to attract valence states and concentrate them on the host Mg atom, yielding a peak in the density of states. It would be premature to interpret the valence-band spectra in Fig. 7 further at this time. We can, however, conclude that the x-ray anomaly probably arises from causes other than the density of

states, that $\rho_1(E)$ differs from $\rho(E)$, showing the effect of screening of the 2p hole on the valence band, and that cross-section variation is important.

F. On Hole-State Localization

It is instructive to compare the valence-electron binding energies in free atoms with those in the corresponding metals. We wish to focus particularly on the question of hole-state localization and extra-atomic relaxation energy effects in the metals. The energy-level diagram appropriate for this comparison is shown in Fig. 8, for the particular case of sodium, a simple monovalent itinerant-electron metal. Optical atomic data[16] have been combined with the cohesive energy,[17] the work function,[18] and the valence bandwidth in constructing this figure.

Let us consider two features of Fig. 8, both of which obtain for metals generally: (1) The average binding energy of the least-bound electron is substantially less in the metal than in the free atom; i.e., $\overline{E_B^V} < E_B^A$, and (2) It takes about as much energy to remove an electron from the metal as it does a unipositive ion core; i.e. $\overline{E_B^V} \cong \overline{E_B^V}(M^+)$. Before proceeding, let us define $\overline{E_B^V}$, the average valence-electron binding energy relative to the vacuum level.

For monovalent metals $\overline{E_B^V}$ presents no problem; it is simply the work function, ϕ, plus the additional energy that it takes to reach the average energy in the valence-band final-state peak. For a free-electron band this gives

$$\overline{E_B^V} = \phi + (2/5)\ (E_0 - E_F) \quad .$$

Here E_0 is the binding energy of the most tightly-bound valence electron state (analogous to the "bottom" of the band in a one-electron initial-state description), and $E_0 - E_F$ is the total spectral (i.e., final-state) band width.

For divalent or trivalent free-electron metals such as Mg or Al a fairly consistent definition of $\overline{E_B^V}$ could be obtained by integrating the final-state valence-band profile (density of states) from E_F up to the energy at which 1/4 or 1/6, respectively, of the density-of-states area is used up. This is a somewhat arbitrary procedure. Its approximate validity can be appreciated by considering a limiting case in which the individual valence bands were nonoverlapping. In that case the least-bound orbital in the free atom would correspond to the valence band nearest E_F. With this approach the coefficient of $E_0 - E_F$ in the above equation would become 0.17 for divalent and 0.11 for trivalent free-electron metals.

We can now quantitatively evaluate the first observation above--that $\overline{E_B^V} < E_B^A$ for valence electrons in several light metals. The results are displayed in Table V. The difference $E_B^A - \overline{E_B^V}$ is always positive and ranges from 2 to 6 eV. Wigner and Bardeen[19] explained the magnitude of the work function (and thus this difference) in 1935. Their arguments were based on free-electron description and the Wigner-Seitz sphere model, and they considered only alkalis, obtaining good agreement with experiment. An interesting discussion of this model has been given by Haug.[20] Recently Lang and Kohn[21] have presented a theory for the work function based on an inhomogeneous electron gas model with pseudopotential corrections, and with surface effects treated carefully. Their theory predicted

work functions of simple metals well (to within 5-10%) and those of noble metals fairly well (within 15-30%). Thus the decrease in valence electron binding energy from atoms to metals, or alternatively the value of the work function, is adequately explained on a free-electron model.

The second observation about--that $\overline{E_B^V} \cong E_B^{\overline{V}}(M^+)$, is deduced by comparing empirical values of E_B^V and $E_c + E_B^A$. Since the latter sum is the energy required to remove an ion core M^+ and a valence electron from the metal, it follows that $E_B(M^+) = E_c + E_B^A - \overline{E_B^V}$, at least for an infinite solid. That $E_B(M^+) \cong \frac{1}{2}(E_c + E_B^A)$ as shown in Table V is less expected. It is satisfying in a rather qualitative way, referring to a model of free-electron metals on the "jellium" level, that ion cores and valence electrons should have nearly equal binding energies, because a positive or a negative charge is being removed from the jellium in the two cases.

On reflection the reason for this binding-energy similarily is not so obvious. Valence-electron emission from a simple metal is usually understood as being accompanied by negligible relaxation enery among the remaining electrons, because the electron leaves a smeared-out free-electron Bloch state. By contrast the ion core is manifestly localized, and its departure must be accompanied by substantial rearrangement of the remaining electrons.

Direct comparisons can also be made of the differences between core-level electron binding energies in atoms and metals,

$$\Delta E_B(\text{core}) = E_B^A(\text{core}) - E_B^V(\text{core}) \quad ,$$

and the differences between valence-electron binding energies,

$$\Delta E_B(v) = E_B^A(v) - E_B^V(v) \quad .$$

Such comparisons show that the "solid-state shifts", ΔE_B, decrease in a gradual manner in going from core to valence orbitals. There is no abrupt change in ΔE_B, nor does it approach zero for valence electrons. Since the core-level shifts were attributed to relaxation of the valence-electron gas to screen the localized final-state core hole, one might be tempted to infer (incorrectly) from the above variation of ΔE_B that valence band holes were also localized, whereas Wigner and Bardeen[19] obtained good values for the work function by assuming the opposite--that the valence-electron hole is completely delocalized.

Before explaining this apparent contradiction, let us make two general observations. First, the distinction between core electrons and (free) valence electrons is somewhat arbitrary. Some bands in most metals should show properties intermediate between the two extremes. Second, if similar values of $\Delta E_B(v)$ or ϕ can be estimated using either localized- or delocalized-hole-state models, then agreement of experiment with these estimates does not carry implications about the degree of localization of the hole state. Although the Wigner-Bardeen[19] model, based on a hole in a free electron gas, produced work functions in good agreement with experiment, this does not necessarily imply that the hole state is delocalized. Even if the hole state is delocalized the "solid-state shift" will be about the same as for a localized hole, as we shall show below.

Let us first compute the work functions for several simple metals on the assumption that the valence-shell hole states are completely localized on single atoms. Referring to the energy-level diagram in Fig. 8, the expression for ϕ in an alkali metal is

$$\phi = E_c + E_B^A(v) - E_R - (\overline{E_{VB}} - E_F) \quad . \tag{9}$$

Here the cohesive energy per atom appears because the removal of one valence electron from a monovalent metal effectively breaks one atom's bonds. The $E_B^A(v)$ term, which can be obtained from optical data, gives the energy required to remove a valence electron from an atom considered alone. The extra-atomic relaxation energy, E_R, has been discussed earlier, particularly in connection with core hole states. These three terms taken together give the average energy of the valence bands or levels, $\overline{E}_{VB}$. Since the complete valence-electron photoemission spectrum is usually available, the difference $(\overline{E}_{VB} - E_F)$ can be obtained empirically and subtracted to obtain the work-function energy ϕ. Assuming the valence-band hole to reside on a single atom, we can estimate the extra-atomic relaxation energy from atomic integrals as

$$E_R(\mathrm{Na}) \cong \frac{1}{2} F^0(3s,3s) \quad ,$$

for sodium, for example. Here the valence-band hole is assumed to be shielded by s-band valence electrons. The factor of 1/2 arises because this is a dynamic relaxation process. Table V gives work functions calculated on this model. The results for monovalent metals agree quite well with experiment. Also given in Table V are values calculated by Lang and Kohn[21] on an itinerant electron model.

For polyvalent metals this simple model can give qualitatively reasonable results, but it is not clear what fraction of the cohesive energy should be included in the expression for ϕ. If all of E_c is included, the values of ϕ estimated for Mg and Al (Table V) are about

one eV too high. If only a fraction of E_c is included the agreement would be improved.

It is no accident that this model gives estimates of ϕ very similar to those obtained from the Wigner-Bardeen model. In fact the terms in the expressions for ϕ in the two models can be related term by term, and it is instructive to do so. Equation (9) of the Wigner-Bardeen paper is, in their original notation,

$$\phi = I + H - \frac{2}{3} F - 0.6\ e^2/r_s + 0.458\ e^2/3r_s - e^2 r_s f'(r_s) + eD \quad . (10)$$

Here their I and H are identical to our $E_B^A(v)$ and E_c, respectively. F is the mean kinetic energy of an electron above the bottom of the band. Since the band width is $\frac{5}{3}$ F, the $\frac{2}{3}$ F term is just the energy difference between the mean energy and the Fermi energy. This is exactly equivalent to our $(\bar{E}_{VB} - E_F)$ term, which measures the difference between the mean binding energy and that of the least-bound electron. The $0.6\ e^2/r_s$ and $0.458\ e^2/3r_s$ terms are Coulomb and exchange energies, respectively. The correlation energy term, in $f'(r_s)$, is not included in our simple approach (it could be), but it is small. Estimates of $e^2 r_s f'(r_s)$ for Na based on the Wigner-Bardeen model and the Böhm-Pines model give 0.11 eV and 0.14 eV, respectively. Finally the surface term eD, although interesting, is also relatively small. It could be included in our simple model but we shall omit it for brevity. Wigner and Bardeen[19] set D = 0. Lang and Kohn[21] have discussed the eD term in detail.

With the last two terms in Eq. (10) neglected and the first three identified with three in Eq. (8) the agreement of these two expressions for ϕ rests on the similarity between the remaining term in each; i.e.,

between E_R and $0.447\ e^2/r_s$ ($= 0.6\ e^2/r_s - 0.458\ e^2/3r_s$). Both of these terms are made up of Coulomb and exchange contributions. The first describes the dynamic relaxation energy associated with valence-band electrons relaxing to shield an electron hole localized on a single atom. By analogy one would expect the second to be the dynamic relaxation energy of the valence band electrons relaxing to shield an itinerant electron hole (a "Coulomb hole" for the Coulomb energy and a "Fermi hole" for the exchange energy). That this is a valid interpretation can easily be shown by re-deriving the Wigner-Bardeen result using this picture. We shall do so for the Coulomb energy. First we note the E_R for the localized-hole model is readily obtained as a matrix element of the "polarization potential" $V_p = V^* - V$ of Hedin and Johansson,[22] where V^* is the Coulomb potential with the hole present and V is the potential with the state occupied. Specifically,

$$E_R = \frac{1}{2} \langle i|V_p|i \rangle \quad ,$$

where i denotes the eigenstate of the electron in question. Applying this approach to the free-electron model and using the expression $3e^2/r_s - e^2r^2/2r_s^3$ as the potential due to the s sphere, we find, on integrating over the s sphere, a Coulombic relaxation energy

$$\frac{1}{2}\left[\int_0^{r_2} 4\pi r^2 (3e^2/2r_s - e^2r^2/2r_s^3)dr\right]\left[4\pi r_s^3/3\right]^{-1} = 0.6e^2/r_s \quad .$$

This is of course the result given by Wigner and Bardeen, but derived from the point of view of relaxation of the valence-electron gas toward the itinerant hole state.

A numerical comparison of the relaxation energies calculated on the two models is very encouraging. For Na, the values are

Localized 3s hole state:

$$E_R = \frac{1}{2} F^0(3s,3s)_{\text{Atomic Na}} = 2.93 \text{ eV} \quad .$$

Delocalized hole state:

$$E_R = 0.6\ e^2/r_s - 0.458\ e^2/3r_s = 3.05 \text{ eV} \quad .$$

Similar agreement is obtained for other alkali metals (Table VI).

We may summarize this section by noting that the binding energy accompanying the removal of a charged particle from a metal contains a many body term--the relaxation energy arising from polarization of the electron gas toward (or away from) the resultant hole. This relaxation energy amounts to a few electron volts and is not strongly dependent on whether the particle is a (monovalent) ion core, a core electron, or a valence electron. From the similarity of the last two cases we can draw two important conclusions: (1) Differential relaxation across the valence band is likely to be small in metals. Therefore this effect should not cause large discrepancies between initial densities of state and photoemission spectra. (2) Relaxation energies are not strongly dependent on the degree of localization of the hole state, and therefore vary not only continuously, but little, from core- to valence-electron states. Explanation of the work function in terms of relaxation of the electron gas about a "Coulomb hole" closes a possible conceptual hiatus between core-electron binding energies, which are well-known to have a contribution from extra-atomic relaxation, and valence-electron binding energies,

which are sometimes regarded as having no relaxation contribution because the valence electrons are delocalized in the initial state. We do not suggest that valence-electron holes in simple metals are in fact localized; the above discussion simply shows that the existence of a relaxation-energy term, and the value of the work function has little bearing on this question.

REFERENCES

1. J. A. Bearden and A. F. Burr, Rev. Mod. Phys. 39, 125 (1967); J. A. Bearden, Rev. Mod. Phys. 39, 78 (1967).

2. H. Neddermeyer, in "Electronic Density of States", NBS Special Publication 323 (1971), p. 313.

3. K. Siegbahn, C. Nordling, A. Fahlman, R. Nordberg, K. Hamrin, J. Hedman, G. Johansson, T. Bergmark, S.-E. Karlsson, I. Lindgren, and B. J. Lindberg, ESCA - Atomic, Molecular and Solid State Structure by Means of Electron Spectroscopy, Nova Acta Regiae Soc. Sci. Upsaliensis Ser. IV, Vol. 20 (1967), Appendix 1.

4. J. Tejeda, M. Cardona, N. J. Shevchik, D. W. Langer, and E. Schönherr, Phys. Stat. Sol. (b) 58, 189 (1973).

5. (a) D. H. Tomboulian, in Handbuch der Physik, ed. by S. Flügge (Springer-Verlag, Berlin, 1957), Vol. XXX, p. 258. (b) Reference 3, p. 36. (c) L. G. Parratt, Rev. Mod. Phys. 31, 616 (1959).

6. American Institute of Physics Handbook, Third Edition (McGraw-Hill, 1972), pp. 9, (172-180).

7. Reference 3, Appendix 2.

8. A. Rosén and I. Lindgren, Phys. Rev. 176, 114 (1968).

9. G. Verhaegen, J. J. Berger, J. P. Desclaux, and C. M. Moser, Chem. Phys. Letters 9, 479 (1971).

10. C. M. Moser, R. K. Nesbet, and G. Verhaegen, Chem. Phys. Letters 12, 230 (1971).

11. L. Ley, S. P. Kowalczyk, F. R. McFeely, R. A. Pollak, and D. A. Shirley, Phys. Rev. B8, 2392 (1973).

12. Reference 11, Sec. IV, especially Eq. (14) and (15).

13. J. B. Mann, "Atomic Structure Calculations. I. Hartree-Fock Energy Results for the Elements Hydrogen to Lawrencium", Los Alamos Scientific Laboratory Report LASL-3690 (1967).

14. Reference 3, p. 152.

15. S. P. Kowalczyk, L. Ley, F. R. McFeely, R. A. Pollak, and D. A. Shirley, Phys. Rev. B9, 381 (1974).

16. C. E. Moore, "Atomic Energy Levels", NBS Circular 467, Volume I (U.S. Department of Commerce, 1949), p. 106.

17. L. Brewer, in High-Strength Materials, ed. by V. F. Zackay (John Wiley and Sons, Inc., New York, 1965), p. 12.

18. Reference 6, p. 280.

19. E. Wigner and J. Bardeen, Phys. Rev. 48, 84 (1935).

20. Albert Haug, Theoretical Solid State Physics (Pergamon Press, Oxford, 1972).

21. N. D. Lang and W. Kohn, Phys. Rev. B3, 1215 (1971).

22. L. Hedin and G. Johansson, J. Phys. B 2, 1336 (1969).

Table I. Magnesium and aluminum core-level binding energies and differences (in eV).

nℓ	E_B^F This work	Ref. 1	E_B^F Ref. 2	Ref. 4	$E_B(n\ell) - E_B(L_{2,3})$ This work	$E_B(n\ell) - E_B(L_{2,3})$ x-ray, Ref. 1	$E_B(n\ell) - E_B(L_{23})$ Ref. 3
Mg 1s	1303.0(1)	1305.4(4)	--	1303.0(2)	1253.6(1)	1253.60(2)	1256
Mg 2s	88.55(10)	89.4(4)	--	88.5(2)	39.15(10)	39.2(1)	38
Mg 2p	49.4(1)	51.4(5)	49.5(1)	49.6(2)	--	--	--
Al 2s	117.99(6)	117.7(4)	--	--	45.15(9)	42.80(15)	44.7
Al 2p	72.84(6)	73.1(5)	--	--	--	--	--

Table II. Comparison of core level binding energies in Mg and Al with theory.[a]

nℓ	$E_B^A(n\ell)$[b]	$E_B^A(n\ell,\text{corr})$[c]	$\frac{1}{2}\langle n\ell\|v_p\|n\ell\rangle$[d]	$E_B^V(n\ell,\text{theory})$	$E_B^V(n\ell,\text{expt})$
Mg 1s	1312	1312.6	5.1	1307.5	1306.7(1)
Mg 2s	97.7	96.6	4.9	91.7	92.25(10)
Mg 2p	56.3	--	4.9	51.4	53.1(1)
Al 1s	1569	1569.6	6.3	1563.3	1562.4(5)[e]
Al 2s	128	126.9	6.0	120.9	122.2(2)
Al 2p	80.6	--	6.0	74.6	77.0(2)

[a] All energies are given in eV.

[b] From Ref. 7.

[c] Using correlation corrections for neon from Refs. 9 and 10.

[d] See Ref. 12.

[e] From x-ray absorption data by K. Langer, Soft X-Ray Band Spectrum, ed. by D. J. Fabian (Academic Press, 1968), p. 62. Error estimate is ours.

Table III. KLL Auger energies in magnesium (in eV).

Transition	E^F(KLL) Ref. 14	E^F(KLL) This work	E^V(KLL) This work	E^A(KLL) Ref. 26	R_e(TA)	R_e(TA) Theo.
KL_1L_1 (^1S)	1101	1106.0(3)	1102.3(3)	1088	14.3	18.9
KL_1L_2 ($^1P_1$)	1135	1139.8(2)	1136.1(2)	1123	13.1	18.9
KL_1L_3 ($^3P_{0,1,2}$)	1150	1154.3(6)	1150.6(6)	1137	13.6	18.9
KL_2L_2 (^1S)	1175	1179.8(2)	1176.1(2)	1165	11.1	18.9
KL_2L_3 (^1D)	1180	1185.3(2)	1181.6(2)	1171	10.6	18.9
KL_3L_3 ($^3P_{0,2}$)	not obs.	not obs.	--	1175	--	18.9

Table IV. Valence-electron binding energies in atoms and solids (in eV).

Element, nℓ	$E_B^A(n\bar{\ell})$[a]	E_c[b]	$e\phi$[c]	$\overline{E_B^V}$[d]	$\frac{1}{2}(E_B^A + E_c)$	$E_B(M^+)$	$\overline{E_B^V}$(corr)[e]	E_R(expt)[f]	E_R(theo)[g]
Li 2s	5.39	1.66	2.4	3.4	3.53	3.65	1.7	3.7	3.1
Na 3s	5.14	1.11	2.3	3.34	3.13	2.92	2.78	2.4	2.9
Mg 3s	7.64	1.52	3.7	4.86	4.58	4.30	4.09	3.5	2.9
Al 3p	5.98	3.35	4.2	4.9	4.67	4.43	3.8	2.2	3.5

[a] Reference 28.

[b] Obtained from ΔH_V (in Ref. 29) by $E_c = \Delta H_V - RT$.

[c] Reference 6.

[d] Derived from x-ray emission data (e.g. Ref. 5) and photoemission results as described in text.

[e] Corrected for (bond energy) ÷ (number of valence electrons).

[f] $E_B^A - \overline{E_B^V}$(corr).

[g] See text and Ref. 11.

Table V. Calculated and experimental work functions (in eV) of Li, Na, Mg, and Al.

	Φ_{loc} [a]	$\Phi_{non\text{-}local}$ [b]	Φ_{expt} [c]
Li	2.95	3.37, 2.33	2.4
Na	2.31	2.83	2.3
Mg	5.10	4.05(0001 face)	3.7
Al	4.63	3.97	4.2

[a] From Eq. (9).

[b] From Ref. 33. An average of values for crystal faces is quoted here, except for Mg.

[c] From Ref. 6.

Table VI. Relaxation energies accompanying valence-electron ionization in alkali metals, based on localized and nonlocalized hole models. Energies are in eV.

Metal (ns)	$E_R(\text{loc}) \cong \frac{1}{2} F^0(ns\ ns)$ [a]	$E_R(\text{itin}) = 0.447\ e^2/r_s$ [b]
Li(2s)	3.18	3.71
Na(3s)	2.93	3.05
K(4s)	2.34	2.45
Rb(5s)	2.18	2.32
Cs(6s)	1.95	2.16

[a] Using Mann's integrals (Ref. 13).

[b] Wigner-Bardeen model, with r_s values from Ref. 33.

FIGURE CAPTIONS

Fig. 1. The 1s, 2s, and 2p x-ray photoemission spectra of atomically clean Mg metal, showing plasmon structure. Binding energies are given relative to E_F.

Fig. 2. The x-ray energy level diagram for magnesium metal and for surface-oxidized magnesium. Photoemission transitions are drawn on the left and x-ray emission lines are shown with arrows pointing down. Oxidation of the surface removes electrons from Mg atoms, creating a more positive environment for core-hole final states in photoemission and raising their energies as shown relative to E_F.

Fig. 3. The one-electron "energy-level" diagram that is conventionally used for discussing x-ray emission and photoemission.

Fig. 4. The KLL and KLV Auger spectrum of atomically clean Mg metal. In the KLL spectrum only primary peak designations are given. In some cases these coincide or overlap with plasmon peaks.

Fig. 5. Effect of extra-atomic relaxation energies on one- and two-hole states in Mg KLL Auger transitions is depicted. The energy-level scale is only schematic, and shifts that cancel between the atom and metal are not shown. The extra-atomic screening energy of the two-hole state should be about four times that of the one-hole state.

Fig. 6. Schematic comparison of shapes of $KL_{23}V$ Auger peaks with XPS spectrum and L_{23} emission spectra. The various states involved are classified using C and V "quantum numbers" as explained in Sec. E of text.

Fig. 7. Upper panel: XPS valence band of Mg (this work).
Middle panel: L_{23} x-ray emission spectrum (from Ref. 2).
Lower panel: Mg $KL_{2,3}$ Auger spectrum (this work).

Fig. 8. Energy-level diagram relating the binding energy of a 3s electron in atomic Na to that of a 3s atom in the metal valence band.

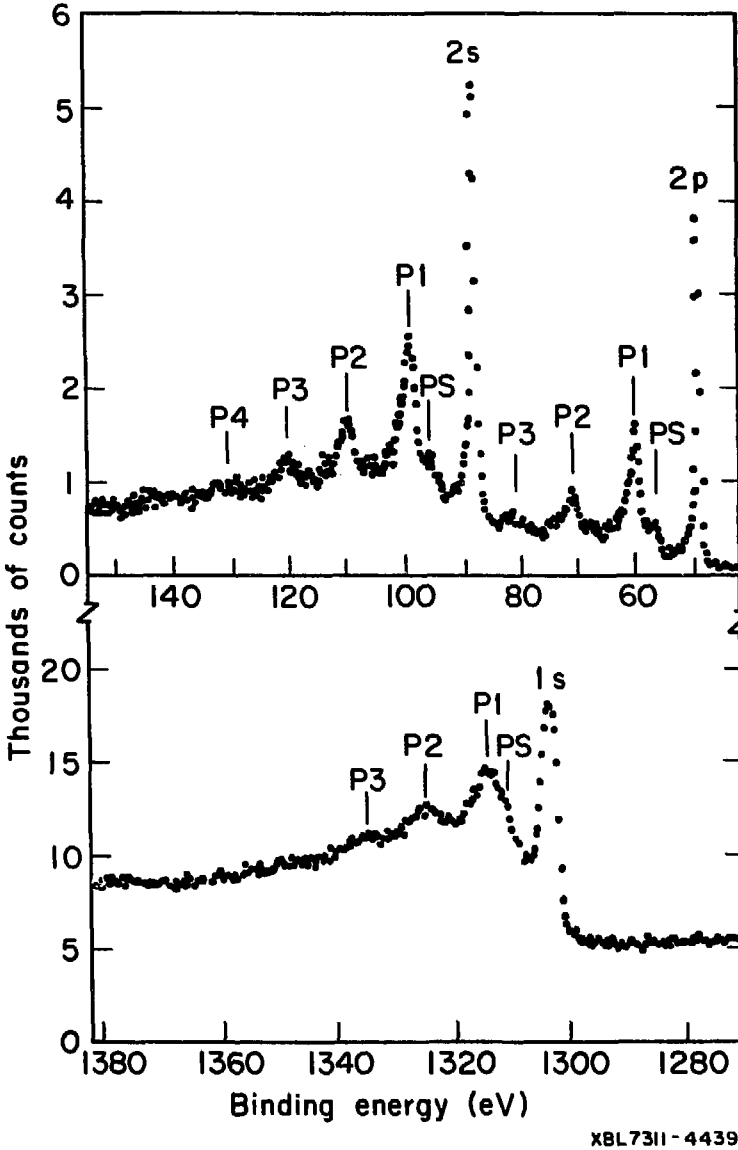
Thousands of counts
Binding energy (eV)
2s
2p
P1
P2
P3
P4
PS
1s
XBL7311-4439

Fig. 1

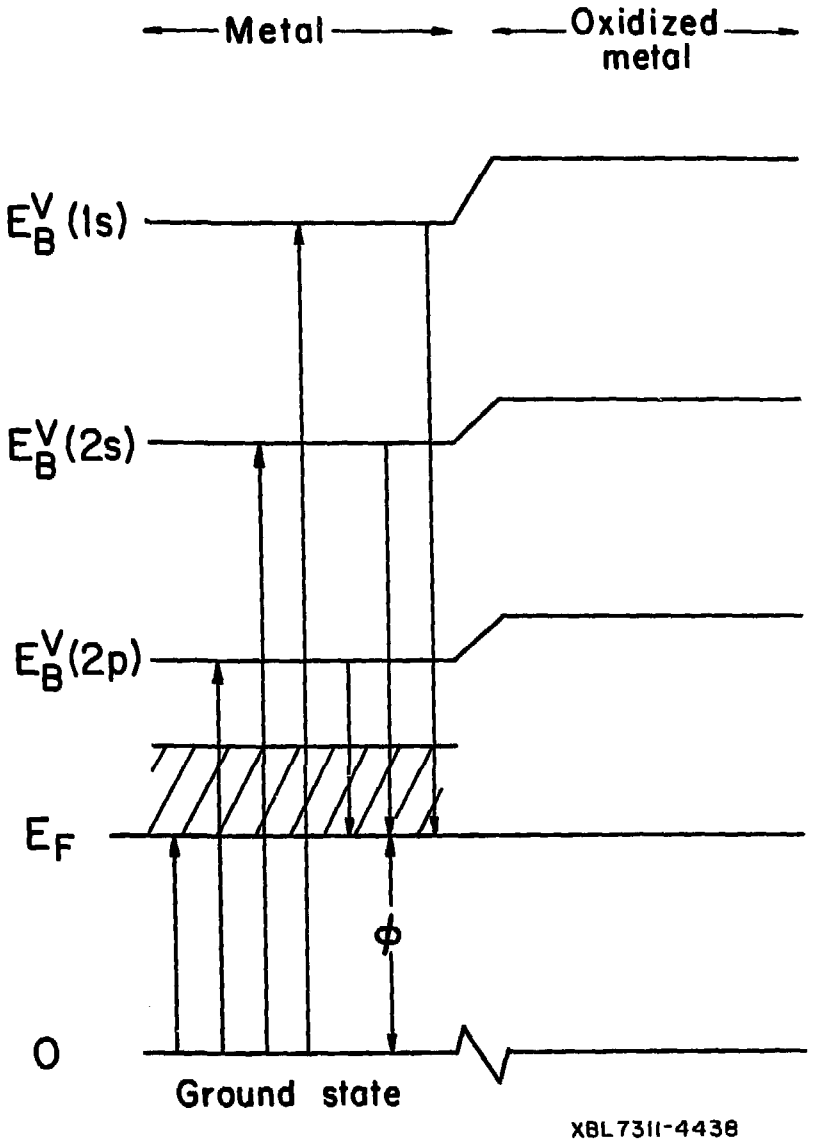
Metal
Oxidized metal
E_B^V (1s)
E_B^V(2s)
E_B^V(2p)
E_F
ϕ
0
Ground state
XBL7311-4438

Fig. 2

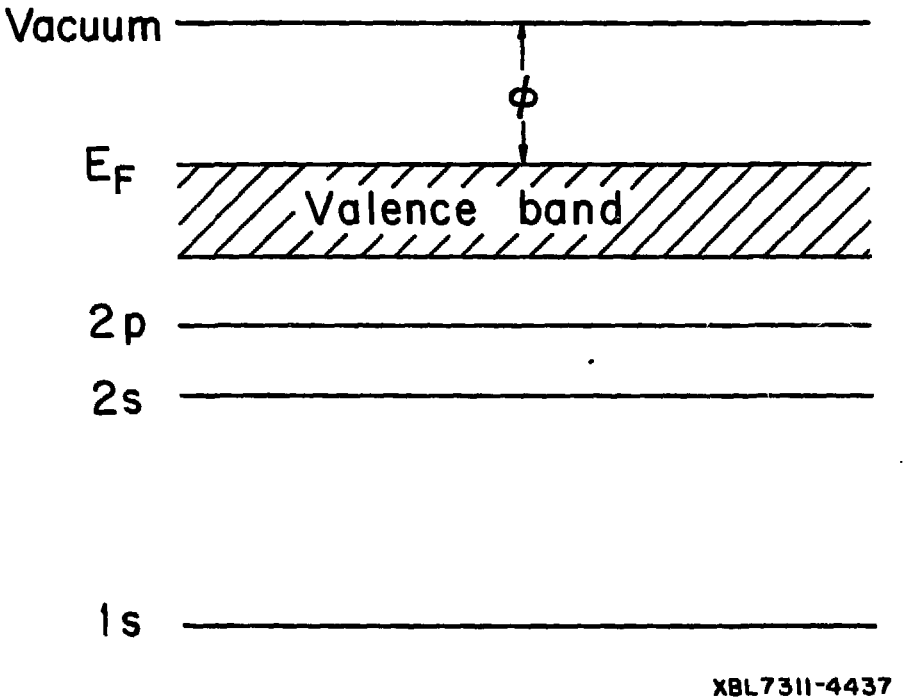

Fig. 3

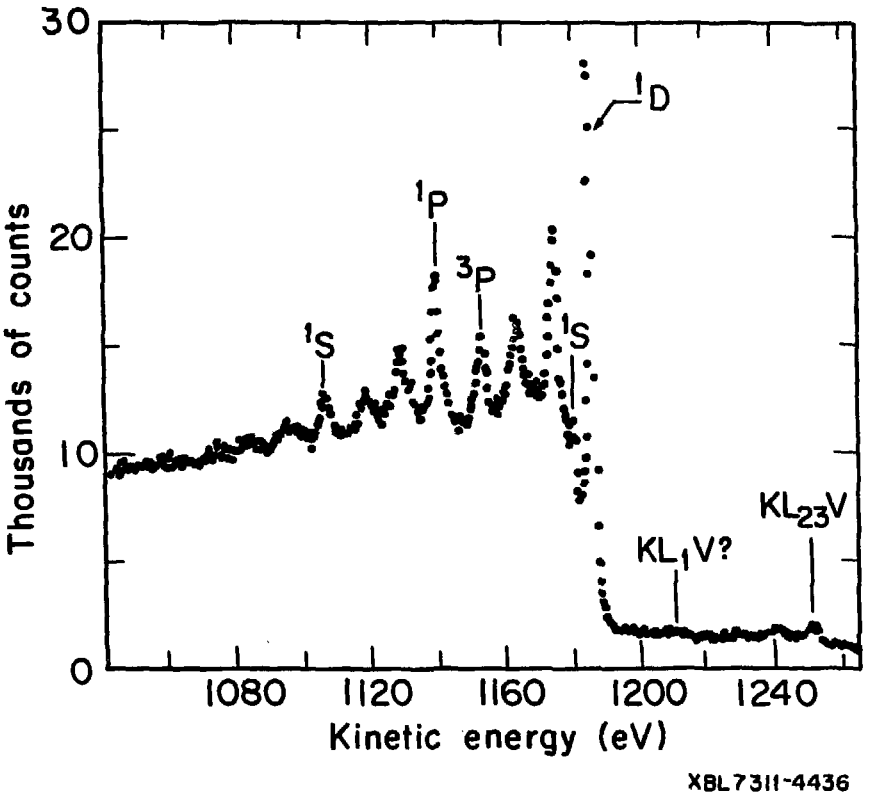
30
20
10
0
Thousands of counts
1080
1120
1160
1200
1240
Kinetic energy (eV)
^1S
^1P
^3P
^1S
^1D
KL_1V?
$KL_{23}V$
XBL7311-4436

Fig. 4

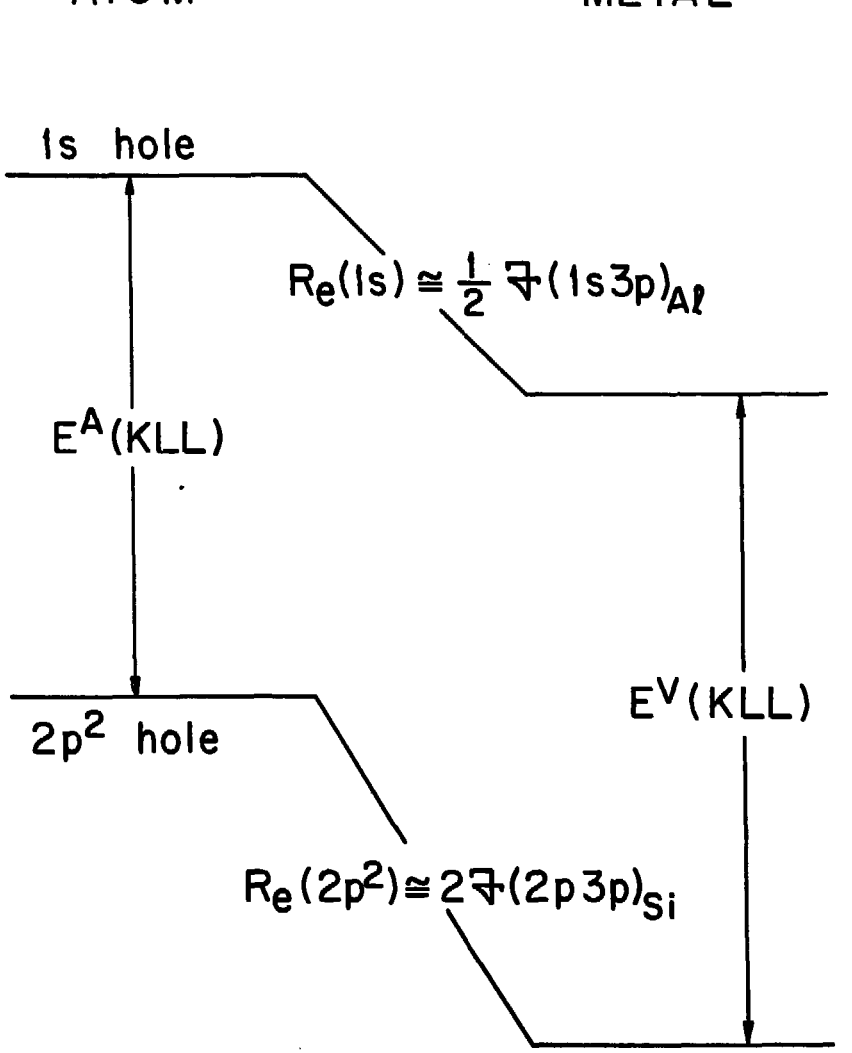

Fig. 5

XBL7311-4435

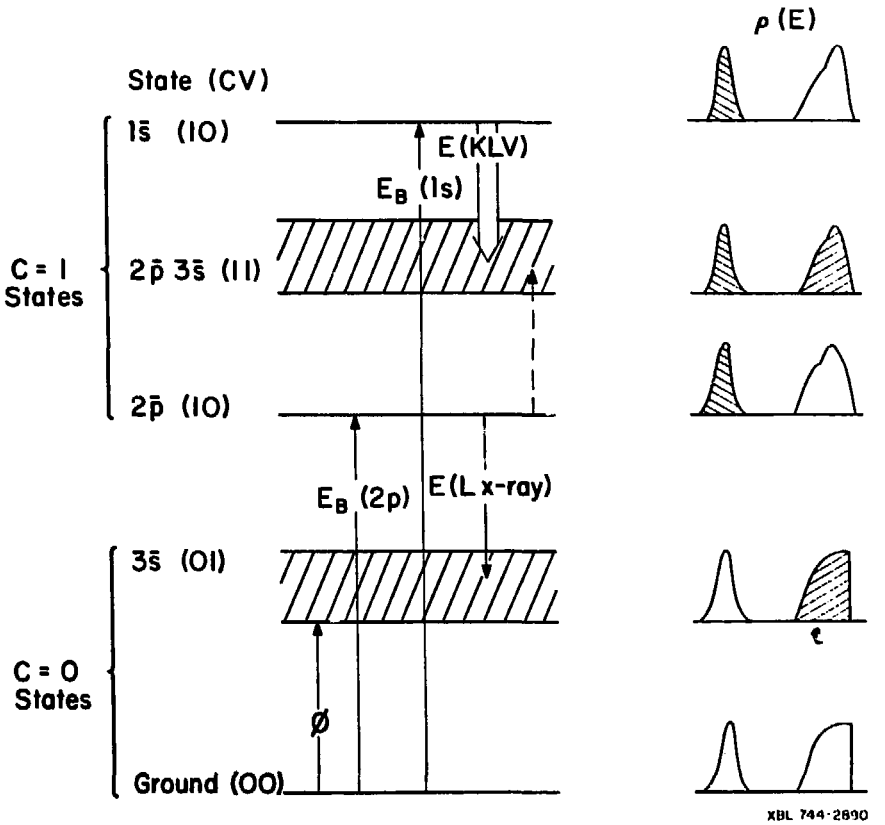
ρ (E)
State (CV)
1s̄ (10)
E(KLV)
E_B (1s)
C = 1 States
2p̄ 3s̄ (11)
2p̄ (10)
E_B (2p)
E(L x-ray)
3s̄ (01)
C = 0 States
Ø
Ground (00)
e
XBL 744-2890

Fig. 6

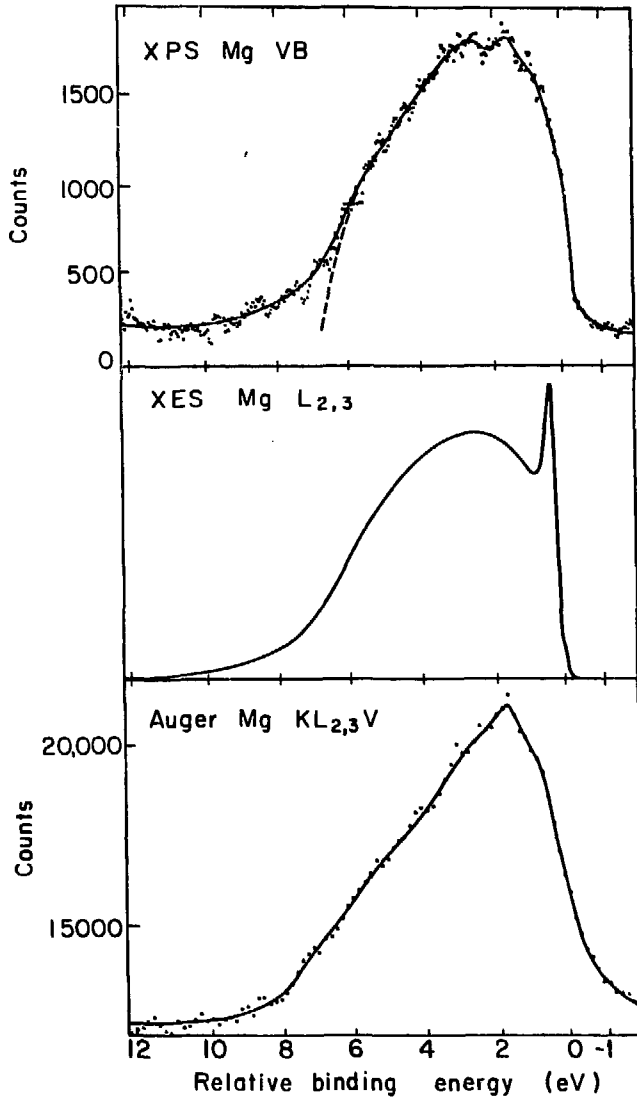
XPS Mg VB
1500
1000
500
0
Counts
XES Mg $L_{2,3}$
Auger Mg $KL_{2,3}V$
20,000
15000
Counts
12
10
8
6
4
2
0
-1
Relative binding energy (eV)

Fig. 7

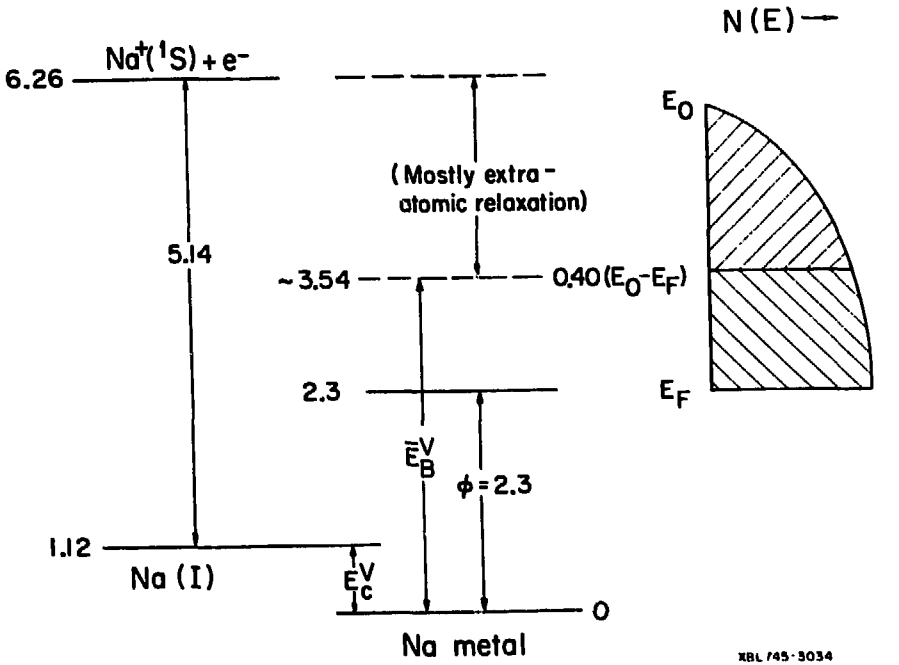
N(E)
6.26
Na+(1S) + e-
(Mostly extra-atomic relaxation)
5.14
~3.54
0.40(E0-EF)
2.3
E0
EF
EVB
ϕ = 2.3
1.12
Na (I)
EVC
0
Na metal
XBL 745-3034

Fig. 8

II. X-RAY PHOTOEMISSION STUDIES OF DIAMOND, GRAPHITE, AND GLASSY CARBON VALENCE BANDS *

Abstract

The high-resolution x-ray photoemission (XPS) spectra of the total valence bands of atomically clean diamond, graphite, and glassy carbon, obtained with monochromatized Al K_α radiation, are reported and discussed. By comparing valence-band and carbon-1s photoelectron kinetic energies, the XPS valence-band spectra I'(E) of diamond and graphite were rigorously affixed to the same energy scale as earlier K x-ray emission spectra, I(E). The two spectra--I'(E) and I(E)--have very different energy dependences of intensity because selection rules and cross-section ratios render I(E) sensitive only to 2p character and I'(E) far more sensitive to 2s character. Taken together, I'(E) and I(E) show that the fractional p character in the diamond valence band increases from ∿16% at the bottom of the band to ∿92% at the top, with an average hybridization of $\sim s^{1.2}p^{2.8}$. The spectra agree well with the density of states of Painter, et al., but indicate a valence bandwidth of 24.2(10) eV rather than their 20.8 eV. The C(1s) binding energy of 284.63(20) eV in graphite agrees well with a recent theoretical estimate of 284.4(3) eV by Davis and Shirley. Analysis of I'(E) and I(E) for graphite resolves the valence bands cleanly into σ and π bands, with the spectrum I'(E) of the former resembling that of diamond, but with a stronger 2s admixture (sp^2 versus sp^3). The XPS cross-section of the (p_z) π bands was very low as expected by symmetry. The bandwidth of 24(1) eV somewhat exceeded Painter and Ellis's calculated value of 19.3 eV. Glassy carbon showed an I'(E) between those

of diamond and graphite, consistent with an amorphous lattice containing both trigonal and tetrahedral bonds.

A. Introduction

The element carbon is in many respects unique among the group IV elements in its solid-state properties. In its diamond modification it structurally resembles the small-band-gap tetrahedral semiconductors silicon, germanium, and grey tin, while it is a very good insulator, in contrast to these materials. At ordinary temperature and pressure, however, the thermodynamically stable form of carbon is not diamond, but graphite, a semi-metallic form without an analog in the group IV series. It is of interest to compare the valence bands of the two forms of carbon because the different coordination--trigonal in graphite and tetrahedral in diamond--suggests substantial differences in their chemical bonding. While the simple tight-binding description of these two forms in terms of sp^2 and sp^3 bonding must be greatly modified to provide a realistic band structure, vestiges of s and p character in the bands should still be manifest through cross-section modulation in the photoemission spectrum. This effect was discussed in an earlier paper on the photoemission spectrum of diamond.[1] In the present paper the valence band x-ray photoemission spectra of graphite and glassy carbon are reported. These spectra, together with the earlier diamond spectrum, are compared and discussed in terms both of valence-band densities of states and the relative effects of cross-section modulation in the three lattices. Comparisons are made with the lower-resolution XPS studies of several forms of carbon by Thomas, et al.[2].

Experimental procedures are given in Sec. B. Results are presented in Sec. C and discussed in Sec. D. Conclusions are given in Sec. E.

B. Experimental

The diamond sample was a single crystal,[3] and the graphite sample was part of a crystal used previously as an x-ray monochromator.[4] The glassy carbon sample was in the form of a polished disc-shaped ingot.[5] In order to prevent contamination by hydrocarbons and/or oxygen, the samples were cleaved or fractured under dry nitrogen in a glove bag and inserted directly into a Hewlett-Packard 5950A ESCA spectrometer at 8×10^{-9} Torr without exposure to the atmosphere. They were then irradiated with monochromatized Al Kα irradiation (1486.6 eV) and the ejected photoelectrons were energy-analyzed.

Energy conservation gives for the apparent binding energy of an electron

$$E_B^{APP} = h\nu - K - e\phi_{sp} + e\psi \quad ,$$

where K is the measured kinetic energy of the photoelectron, ϕ_{sp} is the spectrometer work function and ψ is the Volta potential due to charging of the sample. The factors governing the magnitude of the Volta potential and its effect on the spectra have been discussed by Ley et al.[6] We note here that in our spectrometer, sample charging merely shifts the apparent binding energies by a constant amount and does not detectably broaden the spectral features.

The problem of obtaining an adequate reference level for the assignment of binding energies in these samples is especially difficult. In a large band-gap insulator such as diamond, appreciable charging (~6 eV) occurs. Attempts to reference the binding energies relative to the Fermi

energy of a thin layer of gold evaporated onto the sample surface have proved to be inadequate, because the position of the Fermi energy determined in this way may not be intrinsic or reproducible.[6] All binding energies in diamond are therefore given with respect to an arbitrary zero point. This point was chosen to be the top of the valence bands, obtained by a linear extrapolation of the region of maximum negative slope on the leading edge of the valence bands to the background count level. Since the onset of photoemission is sharp, this point could be located with reasonable precision.

Graphite is a semimetal and thus has no band gap. The intrinsic conductivity prevents it from charging and the Fermi level is well defined at the top of the valence band. A Fermi edge was indeed observed in our spectra and binding energies are given with respect to it; however, the low intensity in this region leads to unavoidable inaccuracies in this assignment.

Glassy carbon is in principle an even more difficult case, since it does not have a well-defined band structure. Furthermore its photoemission intensity at low binding energies is even lower than in the case of graphite. In order to have a well-defined reference energy for the purposes of our discussion, we aligned the centroids of the strongest valence-band peaks in graphite and glassy carbon and adopted the assigned position of E_F in graphite as the zero of energy in glassy carbon.

C. Results

In Fig. 1 are shown the spectra of diamond, crystalline graphite, microcrystalline graphite, and glassy carbon. The intensity curves $I'(E)$ have been obtained from the raw spectra by the application of a correction

for inelastic scattering. The correction was made by assuming that the inelastic loss spectrum could be approximated from a discrete loss structure determined by folding a response function obtained from the inelastic structure of the C 1s line with the valance band structure.

An inspection of the spectra in Fig. 1 reveals that all four samples display the same gross structure. Each spectrum shows: (1) a fairly broad, intense peak located between 16 and 21 eV, hereafter referred to as peak I, (2) a narrower, less intense peak located at about 10 to 15 eV (peak II) and (3) a very broad and decidedly weaker structure, extending from 10 to 13 eV to the cutoff energy ("peak" III). There are, however, easily noticeable and significant differences in the spectra. Peak I in diamond is less dominant than its analog in graphite and glassy carbon. In addition, peak III arises sharply in diamond while in graphite it tails off slowly toward low binding energies. Also, in graphite there is a well-defined minimum between peaks I and II, which persists even in the microcrystalline sample. This minimum is less pronounced in glassy carbon. In the next section the factors accounting for these differences are discussed, and they are shown to arise from both density-of-states and photoemission cross-section effects.

The spectra reported by Thomas et al.[2] agreed with ours in broad outline. Their valence bands were typically $\sim$8eV wider than ours and they showed no evidence of peak II in most cases. The excess width probably arose from a cruder scattering correction which systematically produces this effect: they subtracted a presumed background rather than inverting a response function. The absence of peak II in their spectra may be a consequence of surface contamination, inhomogeneous broadening

due to a spread in the Volta potential, or simply lower resolution. The interpretation given below is based entirely on our spectra.

D. Discussion

To interpret the spectra in Fig. 1 properly, it is first necessary to consider the various factors which contribute to the photoemission intensity. The photoemission intensity at a given energy E may be written as

$$I(E) \propto \rho^{i}(E)\ \rho^{f}(\hbar\omega - E)\ \sigma(\hbar\omega,E) \quad , \tag{1}$$

where $\rho^{i}(E)$ is the density of initial states in the crystal, $\rho^{f}(\hbar\omega - E)$ is the density of final states of the system including the final state of the photoelectron, and σ is the cross-section for the process. A one-electron transition model is of course assumed in this discussion. At ~1480 eV the conduction bands of these crystals are expected to be very free-electron like and thus featureless, reducing the intensity expression to

$$I(E) \propto \rho^{i}(E)\ \sigma(\hbar\omega,E) \quad . \tag{2}$$

In carbon, the cross-section term is extremely important, as $\sigma(\hbar\omega,E)$ is a very strong function of E in the valence-band region.

It can be shown[7,8] that the cross section for photoemission from a state ψ_k may be written as

$$\sigma_k \propto |\langle \psi_k | P\omega(q) \rangle|^2 \quad , \tag{3}$$

where P (q) denotes a plane wave of wavevector q. In deriving this expression, it is necessary to assume the electric dipole approximation,

the Born-Oppenheimer approximation, a frozen orbital approximation for the photoemission process, and finally that the continuum state of the photoelectron may be represented by a plane wave. This last approximation is rather dubious in principle since it violates the fundamental requirements of orthogonality. However, at large q the error introduced by it should not be serious.

The only problem remaining in the calculation of σ_k is our lack of knowledge about the band state ψ_k, which is the object of study. Since atomic cross sections may be determined unambiguously either by experiment or calculation, we shall adopt the approach of relating the band state cross sections to their atomic components. This is in principle a difficult undertaking, since the free atom states are eigenstates of the angular momentum, while the band states are eigenstates of the linear momentum. However, Block's theorem states that an eigenfunction of the n^{th} band of momentum $\hbar k$ may be written

$$\psi_{nk}(\vec{r}) = u_{n\vec{k}}(\vec{r})\, e^{i\vec{k}\cdot\vec{r}} \quad , \tag{4}$$

where $\vec{k}$ lies within the first Brillouin zone and $u_{n\vec{k}}(\vec{r})$ is a function with the periodicity of the lattice, depending only parametrically on $\vec{k}$.

For the case of a linear one-dimensional lattice with lattice constant a, $-\pi/a < k \leq \pi/a$. Since $\lambda = 2\pi/k$ the minimum wavelength of the phase factors in Eq. (4) will be $\lambda_{min} = 2a$. The extension to three-dimensional lattices is clear. The importance of this result lies in the form of the overlap integral (3). This integral can be large if the curvature of the plane wave matches that of the Bloch state. Since the de Broglie wavelength of an electron ejected from the valence bands

is ~0.32 Å, there can be no significant contribution from the phase factor of the Bloch state. The overwhelming contribution to this integral must come, then, from the overlap of the plane-wave with $u_{n\vec{k}}(r)$, the periodic part of the Bloch function.

In the limit of totally non-interacting electrons in a lattice, the $u_{n\vec{k}}(r)$ reduce to the atomic functions, losing their parametric dependence on $\vec{k}$. In the actual crystal, $u_{n,\vec{k}}(r)$ will resemble some linear combination of atomic functions to a very high degree near the nuclei, since in these regions the perturbation due to the presence of the other atoms is relatively small. Furthermore, it is precisely in this region near the nuclei that the radial nodes in the wavefunction can match the curvature of the plane wave, yielding a large contribution to the integral. Therefore, a band constructed from states of the type $\psi_k = \phi_{2s}(r)\, e^{i\vec{k}\cdot\vec{r}}$, for example, should be expected to show qualitatively the same cross-section behavior as an assembly of non-interacting 2s states. One can therefore regard the cross section of the band state as the sum of the cross sections of its principal atomic components. Thus if a band is formed largely out of atomic s and p orbitals the photoemission cross section should reflect the relative extent of the s and p character of the band.

In carbon, the effect of cross-section modulation in the valence bands is particularly large. The valence bands arise mostly from the 2s and 2p atomic states, and the cross section ratio for photoemission by Al $K\alpha_{12}$ x-rays is $\sigma(2s)/\sigma(2p) \approx 13$.[9] The reason for this large ratio is that the 2s atomic function has one radial node while the 2p state has no radial nodes. The great increase in curvature provided by the

2s node allows for much larger overlap with the $\lambda \approx 0.32$ Å plane-wave-like final state. With these effects in mind the valence band spectra of each form of carbon can now be examined.

1. Diamond

The XPS spectrum of diamond has been discussed earlier[1] in connection with cross-section modulation and the theoretical density of states given by Painter, et al.[10] We shall briefly discuss this spectrum again here for two reasons. First, it provides a useful framework for understanding the glassy carbon results; and second, we have recently realized that the valence-band spectrum can be nicely related to the x-ray emission spectrum in a way that obviates the necessity of establishing a fiducial energy such as E_F or the top of the valence bands. Figure 2 shows our XPS spectrum I'(E), the K-emission spectrum $I(E)/\nu^2$ of Wiech and Zöpf,[11] and the density of states[10] $\rho(E)$ of diamond. The abcissa is the K x-ray emission energy, E(1s - v), to which we have referred the valence-band XPS spectrum in a completely rigorous way by using the relation

$$E(1s - v) = E_B(1s) - E_B(\text{valence}) \quad ,$$

where the two quantities E_B are binding energies with any common reference. Our reference was the Fermi energy of an evaporated gold layer.[1] Thus, for example, the sharp middle peak of the XPS valence-band spectrum (peak II) falls at 271.2 eV on the E(1s - v) scale, the difference between $E_B^F(1s) = 284.44(7)$ eV and $E_B^F(II) = 13.2(2)$ eV.[1]

Although the above relation is rigorous and straightforward, there exists in the literature a strong tendency to discuss x-ray emission and XPS results in terms of initial-state one-electron orbital energies, ε.

Since orbital energies are computational artifacts rather than observables, confusion may arise in the comparison of XPS and x-ray emission spectra due to the presence of (different) many-body relaxation effects. This problem need never arise, however, if the total energies of the system are considered. Figure 3 shows the energy-level structure of the diamond lattice according to this description. Because x-ray emission connects the two states that are studied by photoemission--the 1s hole state and the valence-band hole state, the energies should match up, and indeed this appears to be the case in Fig. 2. Referring to that figure we note that feature E in the x-ray spectrum corresponds quite well to our peak I, and peak D to our peak II. Peak B and shoulder C can be interpreted as corresponding to the broad "peak" III in the XPS spectrum. Especially pleasing is the agreement between the positions of the top of the valence band, obtained by extrapolating peaks B and III. These fall at energies of 283.7 eV (peak III) and 283.9 eV (peak B). The valence-band peak energies in diamond therefore appear to be on a very firm experimental basis. The energy dependence of the intensities of the x-ray emission and XPS spectra, $I(E)$ and $I'(E)$, are very different, however, To interpret this observation let us relate $I(E)$ and $I'(E)$ to the electronic band structure of diamond.

With two atoms per unit cell, diamond has eight valence electrons filling four bands. The lowest band, which is wide and s-like, gives rise to peak 1 in the density of states,[11] to peak I in the XPS spectrum, and probably to feature E in the x-ray emission spectrum. The high cross-section of the C(2s) orbital for photoemission at this energy[1] greatly enhances the prominence of peak I, while feature E in $I(E)/\nu^2$ is

suppressed because the 1s → 2s transition is forbidden in the K-emission spectrum.

The second valence band is degenerate with band 1 along the line X-Z-W in the Brillouin zone.[10] It contains a strong mixture of s and p character. Because peak II in I'(E) and peak D in $I(E)/\nu^2$ arise largely from this second band, they are enhanced (suppressed) to an intermediate extent relative to peak 2 in ρ(E) by cross-section modulation.

More dramatic changes of intensity are observed in peaks III and B. This is attributable to the stronger p character of bands 3 and 4, which largely comprise peak 3 in ρ(E). For 2p electrons K x-ray emission is completely allowed, while the cross-section for x-ray photoemission is lower by a factor of 13 than that of a 2s electron.

Although the agreement between the XPS spectrum and ρ(E) as given by Painter, et al.,[10] was described earlier as "excellent",[1] there was at that time some uncertainty as to how the relative energies of I'(E) and ρ(E) should be compared. With the additional support of the x-ray emission spectrum $I(E)/\nu^2$, and particularly in view of the agreement between $I(E)/\nu^2$ and I'(E), we can make a more critical comparison of theory and experiment. To do this we aligned peak 2 in ρ(E) with peaks D and II, which agreed well with one another (although ρ(E) has the same size energy scale in Fig. 2 as do $I(E)/\nu^2$ and I'(E), the transition energy on the abcissa of course does not apply to ρ(E)). The theoretical ρ(E) histogram then appears to be somewhat narrower than the experimental curves, both overall and with regard to the energy separation between characteristic features. Thus the total valence bandwidth is 24.2 ± 1.0 eV experimentally, with most of the uncertainty

arising from the extrapolation of I'(E) to zero intensity at the bottom of the bands. Even after scattering corrections are made, valence-band XPS spectra tend to show "tailing" at the low-energy end. We believe that this arises from imperfect scattering corrections rather than valence-band structure because theoretically the first band decreases smoothly and parabolically in energy as it approaches the band minimum at Γ in the Brillouin zone and thus $\rho(E)$ should decrease rapidly. Accordingly we have sketched in a dashed line in Fig. 2 that represents what we believe to be the shape of I'(E) if scattering were fully accounted for. This line intersects the abcissa at an energy of 259.6 eV with an estimated accuracy of 1 eV or better. The bandwidth of (24.2 ± 1.0) eV was obtained by subtracting this energy from that of the top of the bands, 283.8 ± 0.1 eV. The calculations of Painter, et al.[10] gave a bandwidth of about 20.8 eV. In Table I the energies of several features are listed, using the top of the valence band as reference.

In a more qualitative vein it is of interest to derive information about s-p hybridization from the diamond valence-band spectrum. The tetrahedral structure of diamond leads naturally to attempts to describe its bonding in terms of sp^3 hybridization. While this approach has some validity at Γ in the Brillouin zone, the crystal symmetry requires the linear momentum $\vec{k}$, rather than angular momentum, should be a good quantum number. For this reason an atomic-orbital basis set, and especially one that is limited to 2s and 2p functions, is inadequate to describe the valence bands. Still, both XPS and K x-ray emission are most sensitive to those parts of the valence-band wavefunctions nearest the nucleus where they are most like atomic functions. These

methods are thus expected to give as good an index of 2s or 2p character as is available. The XPS spectrum I'(E) was compared to ρ(E) alone earlier to give a rough measure of s and p character across the valence-band region. With the additional intensity information and more reliable reference energy provided by the x-ray emission data, we can now carry this analysis further.

First we make the qualitative observation that, while Fig. 2 indicates mainly s character at the bottom of the valence bands and mainly p character at the top, there is clear evidence for considerable s-p mixing throughout. The finite value of $I(E)/\nu^2$ in feature E denotes some p character. On the other hand, the ratio

$$\frac{(I'(E)/\rho(E))_{\text{peak I}}}{(I'(E)/\rho(E))_{\text{peak III}}} \approx 5 \quad ,$$

is significantly less than $\sigma(2s)/\sigma(2p) = 13$, the value expected if peak I were pure 2s and peak III pure 2p in character.

To carry this analysis further we defined the ratios

$$R_{XPS}(E) \equiv I'(E)/\rho(E)$$

$$R_X(E) \equiv (I(E)/\nu^2)/\rho(E) \quad .$$

The values of $R_{XPS}(E)$ and $R_X(E)$, as deduced from the data in Fig. 2, are plotted in Fig. 4. Since ρ(E) did not line up exactly with the two spectra, it was necessary to expand the energy scale of ρ(E) slightly and to smooth the rather rough curve given by point-by-point calculations of $R_{XPS}(E)$ and $R_X(E)$. This may result in the loss of some meaningful fine structure.

To extract the fractional s and p characters from the ratios in Fig. 4, we define fractions of s and p character, $f_s(E)$ and $f_p(E)$, and assume $f_s(E) + f_p(E) = 1$ for all E. Since the K x-ray emission cross section is zero for 2s electrons, we can write

$$f_p(T)/f_p(B) = R_X(T)/R_X(B) = 5.6 \quad ,$$

where the number 5.6 was taken from Fig. 4 and T and B denote the top and bottom of the bands. Invoking the free-atom XPS cross-section ratio of 13, we have

$$\frac{f_p(B) + 13\, f_s(B)}{f_p(T) + 13\, f_s(T)} = \frac{R_{XPS}(B)}{R_{XPS}(T)} = 5.86 \quad .$$

Simultaneous solution of these equations gives

$$f_p(B) = 0.16$$

$$f_p(T) = 0.92$$

as the fractional p mixing at bottom and top of the diamond valence bands. By comparing $R_{XPS}(E)$ and $R_X(E)$ separately with these two end points, we can derive two estimates of the energy dependence of f_p that based mainly on XPS and x-ray emission spectra, respectively. These are shown in Fig. 5. The two estimates of f_p show satisfactory agreement, especially considering the difficulty of estimating f_p. At a more speculative level of interpretation, we can evaluate the mean fractional p character of the diamond valence bands as

$$\overline{f_p} = \frac{\int f_p(E)\ \rho(E)\ dE}{\int \rho(E)\ dE} = 0.695 \quad ,$$

which implies a configuration of $s^{1.2}p^{2.8}$ for diamond, in good agreement with chemical intuition, which would favor sp^3 over s^2p^2.

2. Graphite

The graphite structure has layers of fused hexagonal rings, with four atoms in the primitive cell.[12] Its valence band structure has eight filled bands instead of four. A band structure calculated by Painter and Ellis[13] is shown in Fig. 6. This ab initio variational calculation used an LCAO basis set of Bloch states,

$$\chi_i(\vec{k},\vec{r}) = \sum_\nu e^{i\vec{k}\cdot\vec{R}_\nu} u_i(\vec{r} - \vec{R}_i - \vec{U}_i) \quad . \tag{10}$$

Where U_i is a vector specifying the atomic position within the unit cell, and u_i is an atomic function. The matrix elements of the Hamiltonian were evaluated without resorting to tight-binding approximations.

The layered nature of the graphite structure causes the bands to be grouped into two distinct classes consisting of six σ bands and two π bands. The π bands are formed largely from the functions $u_i = 2p_z$, while the σ bands are formed from the remaining orbitals.

The valence-band XPS spectrum of graphite is shown in Fig. 7, together with the K x-ray emission spectra of Chalklin.[14] The C(1s) binding energy relative to the Fermi level, E_B^F(C 1s) = 284.68(20) eV was used to set the valence-band XPS spectrum on the same scale as the K x-ray emission spectrum. The value of E_B^F(C 1s) has recently been

estimated theoretically by Davis and Shirley[15] as E_B^F = 284.4(3) eV (after correction for a work function of 4.6 volts). This excellent agreement is very encouraging, especially so because a rather large relaxation energy term was involved in the theoretical estimate.

In contrast to diamond, peak I in the graphite structure is even more dominant, with a broad, flat top. This peak arises from the two nearly degenerate s-like σ_1 bands. Because a set of p-like atomic orbitals, the $2p_z$'s, are largely unmixed with the other bands, one would expect peak I to arise from purer s-like states than its analog in diamond. This explains, at least qualitatively, its greater relative intensity. The width of this feature ($\sim$5 eV) corresponds reasonably well with the value of 5.90 eV calculated by Painter and Ellis for the width of the σ_1 bands, while its flat top may arise from the shallowly sloping σ_1 and σ_2 bands between Q and P in the Brillouin zone.

Proceeding to lower binding energies we find a small peak located at 13.8 eV below E_F and separated from the σ_1 peak by a distinct minimum. This peak may be interpreted in light of the band structure calculation as being due to the high density of states near the point P_1^+ in the Brillouin zone, with the width of the valley reflecting the separation of the two σ_2 and two σ_3 bands at the symmetry point P. This peak drops off very sharply on the low binding energy side, reflecting the relatively steep rise of the σ_2 and σ_3 bands in this region. There is then an inflection in this descent in the region E_F - (8 - 12) eV. In this energy region K emission spectrum begins to show appreciable intensity. The σ and π bands are labeled after Tomboulian[16] according to the calculations of Coulson and Taylor.[17] From E_F - 10 eV up to E_F, corresponding

to a K-emission energy range of 275 - 285 eV, the XPS spectrum and the K-emission spectrum are discussed together below.

From E_F - 8 eV to E_F - 4 eV the XPS intensity I'(E) decreases very rapidly. We attribute this to the exhaustion of the σ_2 and σ_3 bands at $\sim E_F$ - 4 eV.[13] These bands, but not the higher π bands, can have some 2s character and hense a relatively large cross-section. The rapid decrease in I'(E) is largely due to the location of the top of the σ_2 and σ_3 bands at Γ, where the phase-space factor in the Brillouin zone goes to zero. The K-emission spectrum of the σ bands would probably behave in a qualitatively similar manner if it could be observed alone, but the $p\pi$ bands have an appreciable intensity of $\bar{I}(E)$, and the $p\pi$-band peak appears as a strong shoulder in the $p\sigma$ peak. The drop of the XPS intensity a low value at E_F - 4 eV constitutes strong independent evidence that the shoulder in I(E) is in fact attributable to $p\pi$ bands, on the basis of cross-section variation. The $p\pi$ peak location at E_F - (3 to 4) eV in I'(E) is in fairly good agreement with the energy E_F - (2 to 3) eV for the flat region of the π bands near Q in the band-structure calculation.[13] Both $\bar{I}(E)$ and I'(E) indicate a maximum in the σ-bands' density of states at $\sim E_F$ - 8 eV. This is probably related to the flat region of the σ_3 band near Q_{2g}^+, which lies at E_F - 7.7 eV.[13]

The reasons for the complete reversal of cross-section ratios in I'(E) and $\bar{I}(E)$ in graphite are simple and illuminating. As discussed above the XPS cross-section for 2s photoemission is about 13 times that for 2p photoemission. The general decrease of I'(E) with energy from the bottom of the valence bands to $\sim E_F$ - 5 eV, where the σ bands end, may be attributed to a decrease in the 2s/2p ratio as in diamond. It

is interesting to note the resemblance between I'(E) for this σ-band portion of the graphite valence bands and I'(E) for the diamond valence bands (Fig. 2). This similarity is pleasing, because the two spectra correspond respectively to two- and three-dimensional lattices of carbon atoms. As noted above, even the increased dominance of the I'(E) features in the bottom of the band in graphite relative to diamond can be explained as arising from a richer mixture of nominal s character in the σ framework (sp^2 vs sp^3). The K-emission spectrum is sensitive only to 2p character; thus that part of $I(E)$ that arises from pσ bands increases as I'(E) decreases near the top of the σ bands, as was the case for diamond.

A further, more striking extension of the reversal in cross-section between I'(E) and $I(E)$ is apparent for the pπ bands. The K-emission cross section for the $2p_z$ electrons that constitute the pπ bands is expected to be about the same as that of the 2p electrons in the σ bands. This expectation is borne out qualitatively by the relative intensities of the pσ-band and pπ-band peaks in Fig. 7 (the simple $sp^2 + p_z$ model would give this intensity ratio as $p\sigma/p\pi \sim 2$). The cross-section of the pπ bands for photoemission is very low, however. Only part of this low value can be attributed to the absence of s character in the pπ bans. The rest may arise from changes in the p_z wavefunctions at large radii due to the delocalized nature of the pπ orbitals.

Table II compares energies of graphite valence band symmetry points derived from the spectra in Fig. 7 with those calculated by Painter and Ellis.[13] The comparison is somewhat tentative because no calculated density of states is available. However, it appears that we now have a

good qualitative understanding of the graphite valence bands. There is some quantitative disagreement between experiment and theory; in particular our 24-eV bandwidth substantially exceeds the 19.3 eV value of Painter and Ellis. Two earlier estimates of the valence bandwidth should be commented upon at this point. The agreement between their bandwidth of 19.3 eV and the K-emission value of 18 eV noted by Painter and Ellis[13] is not valid because the latter applies only to p bands (Fig. 7). Also, the bandwidth of 31 ± 2 eV reported by Thomas, et al.[2] differs from our result mainly because of different data analyses: their raw data agree reasonably well with ours if differences in resolution are taken into account.

3. Glassy Carbon

In examining the valence band spectrum of glassy carbon, the following observations can be made: 1) The spectrum resembles that of graphite more than diamond in the region of peak III, showing a gradual decrease in intensity rather than a sharp cutoff, 2) The total width of the intense part of I'(E) is nearer that of graphite than that of diamond. Defining this width W as the energy separation between the points in I'(E) of half the maximum height on the low-energy side and of quarter height on the high-energy side, we find W = 15.5 eV (graphite), 18 eV (diamond), and 16 eV (glassy carbon), 3) Peak I is intermediate in relative intensity between diamond and graphite, and 4) The valley between peaks I and II is filled in.

It is actually not surprising that the XPS spectrum of the amorphous material should resemble the crystalline cases so closely. As Weaire and Thorpe[18] have pointed out and numerous XPS experiments have demonstrated,

the gross features of the density of states depend on atomic properties and the short-range order in the crystal, while the long-range order is responsible for the fine structure. The filling-in of the valley between peaks I and II is an example of the kind of fine-structure change observed earlier in amorphous materials.[19,20] The other features noted above are consistent with glassy carbon possessing both trigonally and tetrahedrally coordinated carbons, with more of the former than the latter.

Figure 8 shows the XPS spectra of the carbon 1s line and its associated characteristic energy losses (CEL's) of the four carbon specimens of this study. The values of the CEL's are tabulated in Table III. A detailed study of the role of CEL's in the XPS spectra of solids is given in Ref. 21. Qualitatively the CEL's of glassy carbon resembles graphite more than diamond. This is particularly evident in P_1 which has been attributed to either an interband transition[22,23] or a collective π electron excitation.[24,25] Since diamond also has a P_1 it is more likely that P_1 is due to an interband transition rather than a collective π electron excitation. Our diamond results agree well with the reflectance experiments of Whetten.[23] Our results for graphite, microcrystalline graphite, and glassy carbon agree reasonably well with other experiments for P_1, and P_2.[22,24] However, it appears P_3 has not been previously reported for graphite and glassy carbon. Our CEL results further support the interpretation of glassy carbon as being primarily graphitic.

A number of models for the structure of glassy carbon have been proposed on the basis of x-ray diffraction data.[26-28] Our results do

not rule out any of these, although they specifically support those that include both trigonal and tetrahedral bonding.

Further evidence is provided by the K-emission data of Saxena and Bragg[29] who noted that the position of the K emission band in glassy carbon falls midway between that of diamond and graphite.

E. Conclusions

High-resolution XPS spectra of atomically clean diamond graphite and glassy carbon were obtained. The diamond and graphite spectra were found to agree well with band-structure calculations after photoemission cross section effects were properly taken into account. By comparing the difference between valence-band and carbon 1s binding energies with k x-ray emission energies, the XPS and x-ray emission spectra of the diamond and graphite valence bands were rigorously placed on the same energy scale. The fractional p character increased from ∿16% at the bottom of the diamond valence bands to ∿92% at the top, and an average hybridization of $s^{1.2}p^{2.8}$ was derived. Comparison of XPS and x-ray emission data divided the graphite valence bands cleanly into σ and π bands, with the former being essentially a two-dimensional version of the diamond bands. Glassy carbon had an XPS spectrum between those of diamond and graphite, in agreement with the presence of both trigonal and tetrahedral coordination.

REFERENCES

*Work performed in collaboration with S. P. Kowalczyk, L. Ley, R. G. Cavell, R. A. Pollak, and D. A. Shirley and published in Phys. Rev. B9, 3573 (1974).

1. R. G. Cavell, S. P. Kowalczyk, L. Ley, R. A. Pollak, B. Mills, D. A. Shirley, and W. Perry, Phys. Rev. B7, 5313 (1973).
2. J. M. Thomas, E. L. Evans, M. Barber, and P. Swift, Trans. Faraday Soc. 67, 1875 (1972).
3. Our diamond sample was a 1.35 carat industrial diamond obtained from West Coast Diamond Tool Co.
4. Our graphite crystal was obtained from Picker Corp. where it had been used as an x-ray monochromator.
5. Our glassy carbon sample was a gift of Professor R. H. Bragg.
6. L. Ley, R. A. Pollak, F. R. McFeely, S. P. Kowalczyk, and D. A. Shirley, to be published.
7. I. G. Kaplan and A. P. Marklin, Sov. Phys.-Dokl. 14, 36 (1969).
8. L. L. Lohr, Jr., and M. B. Robin, J. Amer. Chem. Soc. 92, 7241 (1969).
9. U. Gelius, in Electron Spectrosocopy, ed. by D. A. Shirley (North-Holland, 1972), p. 311.
10. G. S. Painter, D. E. Ellis, and A. R. Lubinsky, Phys. Rev. B4, 3610 (1971).
11. Wiech and Zöpf, in Electronic Density of States, Nat. Bur. Std. Special Publication 323, p. 335 (1969).
12. R. W. G. Wycoff, Crystal Structures (John Wiley and Sons, 1963), Vol. 1, p. 27.

13. G. S. Painter and D. E. Ellis, Phys. Rev. B1, 4747 (1970). A modified version of this calculation was quoted by R. F. Willis and B. Fitton, J. Vac. Sci. Tech. 9, 651 (1972).

14. F. C. Chalklin, Proc. Roy. Soc. A194, 42 (1948).

15. D. W. Davis and D. A. Shirley, J. Electr. Spectrosc., to be published.

16. D. H. Tomboulian, Handbuch der Physik XXX, ed. by S. Flügge (Springer-Verlag, Berlin, 1957), p. 246.

17. C. A. Coulson and R. Taylor, Proc. Phys. Soc. (London) A65, 815 (1952).

18. D. Weaire and M. F. Thorpe, Phys. Rev. B4, 2508 (1971).

19. L. Ley, S. Kowalczyk, R. Pollak, and D. A. Shirley, Phys. Rev. Letters 29, 1088 (1972).

20. L. Ley, R. A. Pollak, F. R. McFeely, S. P. Kowalczyk, and D. A. Shirley, Phys. Rev. B8, 641 (1973).

21. R. A. Pollak, L. Ley, F. R. McFeely, S. P. Kowalczyk, and D. A. Shirley, J. Electr. Spectrosc.

22. E. A. Taft and H. R. Philipp, Phys. Rev. 138, A197 (1965).

23. N. R. Whetten, App. Phys. Letters 8, 135 (1966).

24. L. B. Leder and J. A. Suddeth, J. App. Phys. 31, 1422 (1960).

25. Y. H. Ichikawa, Phys. Rev. 109, 653 (1958).

26. T. Noda and N. Inagaki, Bull. Chem. Soc. (Japan) 37, 1534 (1964).

27. J. Kakinoki, Acta. Cryst. 18, 518 (1963).

28. K. Furukawa, J. Cryst. (Japan) 6, 101 (1964).

29. R. R. Saxena and R. H. Bragg, private communication.

Table I. Positions of characteristic points in the diamond valence bands (in eV).

Feature	E(x-ray)[a,d]	E(XPS)[b,d]	E(theo)[c,d]
Midpoint of top peak (3,B,III)	5.5	∿ 6	4.3
Shoulder (C)	9.0	--	7.5
Second peak (2,D,II)	12.9	12.6	11.0
Minimum	--	14.2	12.8
Bottom peak (I,E,1)	∿ 17	17.1	15.0
Bottom of valence bands	--	24.2	20.8

[a] Reference 11.

[b] This work.

[c] Reference 10.

[d] Energy below top of valence band.

Table II. Tentative comparison of positions of characteristic features and symmetry points in graphite valence bands (in eV below E_F).

Experimental Feature	Energy	Theoretical Feature	Energy[a]
π-band peak	3-4	flat π band near Q	2-3
top of σ bands	∿ 5	Γ^-_{3g}	4.5
σ-band peak	8 ± 1	flat σ_3 band near Q^+_{2g}	∿ 7.7
sharp peak	13.8	P^+_1	11.5
flat-top σ peak	17-19	P^+_3, Q^+_{1g}	13,15
bottom of bands	24	Γ^+_{1g}	19.3

[a]These numbers were read from the plots of Painter and Ellis (Ref. 13).

Table III. Carbon characteristic energy losses (eV).

	P_1	P_2	P_3
	Graphite		
XPS	6.3(1)	28.1(3)	33.3(3)
Other measurements[a]	7.2	24.9	--
Calc.	7.5[a], 12.5[b]	25.1	--
	Microcrystalline Graphite		
XPS	5.6(2)	22.0(4)	30.3(4)
Other measurements[a]	--	--	--
Calc.	6.7 - 7.2	22.3 - 24.1	
	Glassy Carbon		
XPS	5.6(2)	26.5(3)	31.6(3)
Other measurements[c]	5.6	21	--
Calc.	6.1	20.3	--
	Diamond		
XPS	11.3(2)	25.4(2)	34.1(3)
Other measurements[d]	12.5	23	31
Calc.	12.5	--	31.1

[a] Reference 24.

[b] W. Y. Liang and S. L. Cundy, Phil. Mag. 19, 1031 (1969).

[c] Reference 22.

[d] Reference 23.

FIGURE CAPTIONS

Fig. 1. Valence-band XPS spectra, before (left) and after (right) correction for inelastic losses, of diamond, microcrystalline graphite, crystalline graphite, and glassy carbon.

Fig. 2. Comparison for diamond of the XPS spectrum I'(E) (this work), the K x-ray emission spectrum $I(E)/\nu^2$ (Ref. 11) and the calculated density of states (Ref. 10). Characteristic features are denoted by roman numerals for I'(E), arabic numerals for $\rho(E)$, and letters for $I(E)/\nu^2$. Abcissa pertains to I'(E) and $I(E)/\nu^2$, as described in text: $\rho(E)$ was drawn my aligning peak 2 with peak II in I'(E). Ordinates are linear and start from zero. Dashed line indicates extrapolation of I'(E) to zero at the bottom of the valence bands to eliminate an artificial tail.

Fig. 3. Relation between photoemission valence-band spectra and x-ray emission energies, discussed in text. Because these are excited (hole) states the relationship between spectral <u>energies</u> is rigorous. <u>Intensities</u> can vary quite differently across the valence band, however, because the two spectroscopies involve different transitions. Thus in Fig. 2 the s-like bands are emphasized in XPS and the p-like bands in K x-ray emission relative to $\rho(E)$.

Fig. 4. Plot for the diamond valence bands of the ratios $R_{XPS} = I'(E)/\rho(E)$ (top panel) and $R_X(E) = (I(E)/\nu^2)/\rho(E)$.

Fig. 5. Fractional p character for the diamond valence bands. The endpoints were derived from XPS and K emission data together, as described in text. The intermediate values were then derived separately from XPS and K emission spectra.

Fig. 6. Graphite band structure, after Painter and Ellis. Symmetry designations are based on the modified version quoted by Willis and Fitton (Ref. 13).

Fig. 7. Graphite valence-band XPS spectrum I'(E) and K x-ray emission spectrum I(E) (Ref. 14). The ordinate is linear and begins at zero. The dashed line at the bottom of the bands is an extrapolation to eliminate artificial tailing. The other dashed lines denote a resolution of the p-band structure as described in text. The Fermi energy falls at 284.68(20) eV.

Fig. 8. Carbon 1s and characteristic energy loss spectra of microcrystalline graphite, graphite, glassy carbon, and diamond. The carbon 1s peaks, P_0 have been aligned.

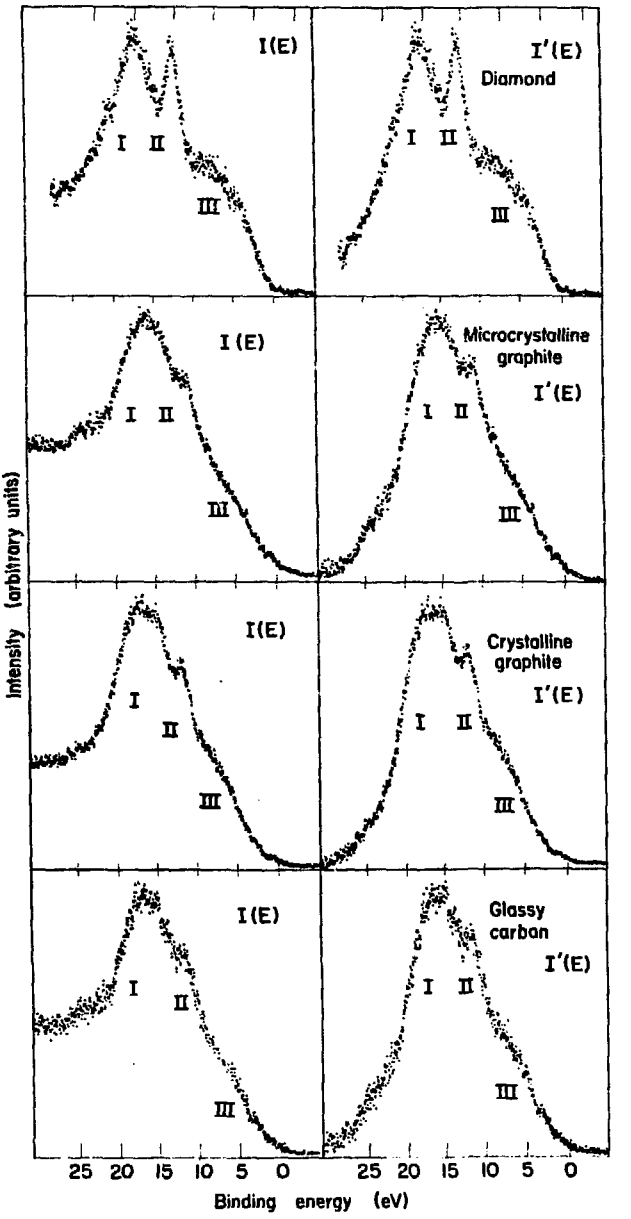
I(E)
I'(E)
Diamond
I
II
III
I (E)
Microcrystalline graphite
I'(E)
I(E)
Crystalline graphite
I'(E)
I(E)
Glassy carbon
I'(E)
Intensity (arbitrary units)
25 20 15 10 5 0
25 20 15 10 5 0
Binding energy (eV)

Fig. 1

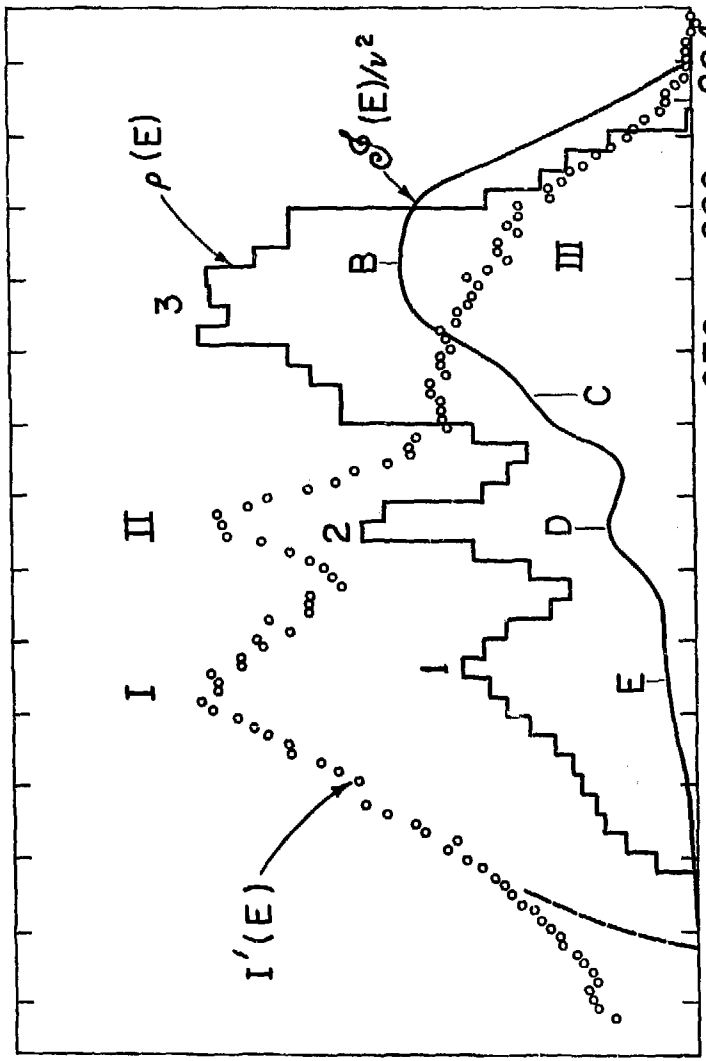

XBL739-4099

Fig. 2

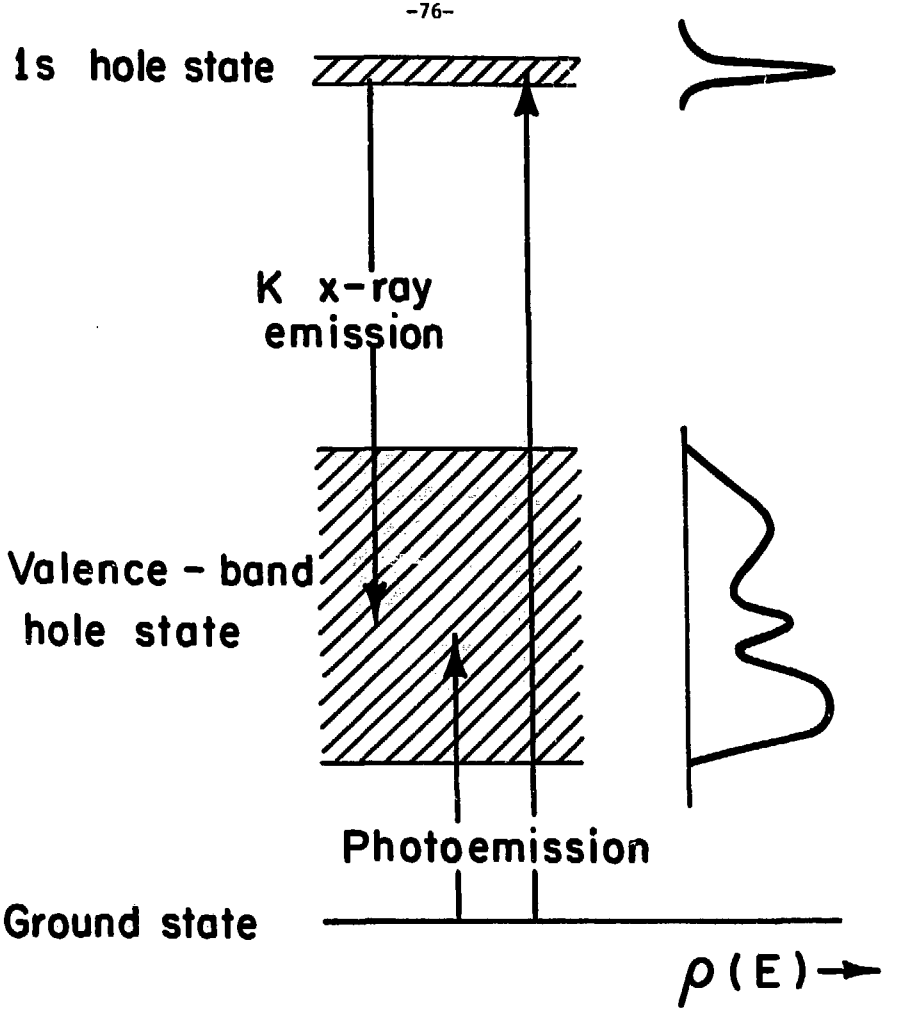

Fig. 3

XBL739-4097

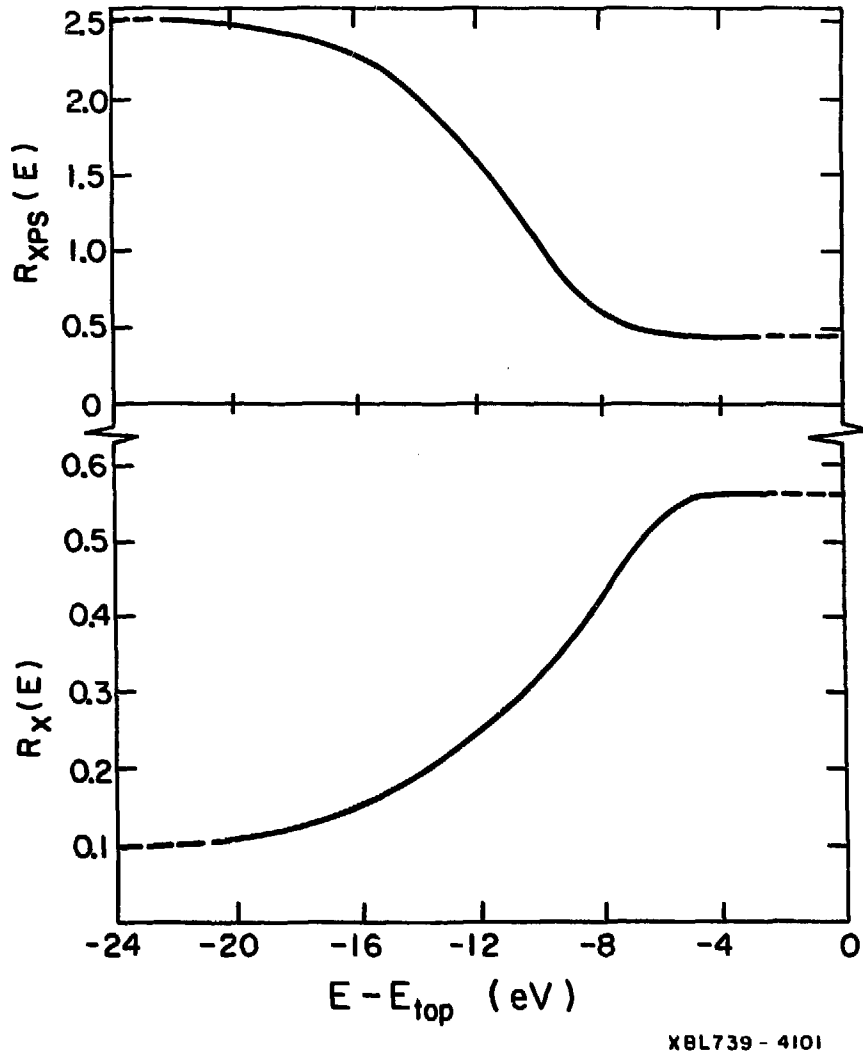
2.5
2.0
1.5
1.0
0.5
0
$R_{XPS}(E)$
0.6
0.5
0.4
0.3
0.2
0.1
$R_X(E)$
-24
-20
-16
-12
-8
-4
0
$E - E_{top}$ (eV)
XBL739-4101

Fig. 4

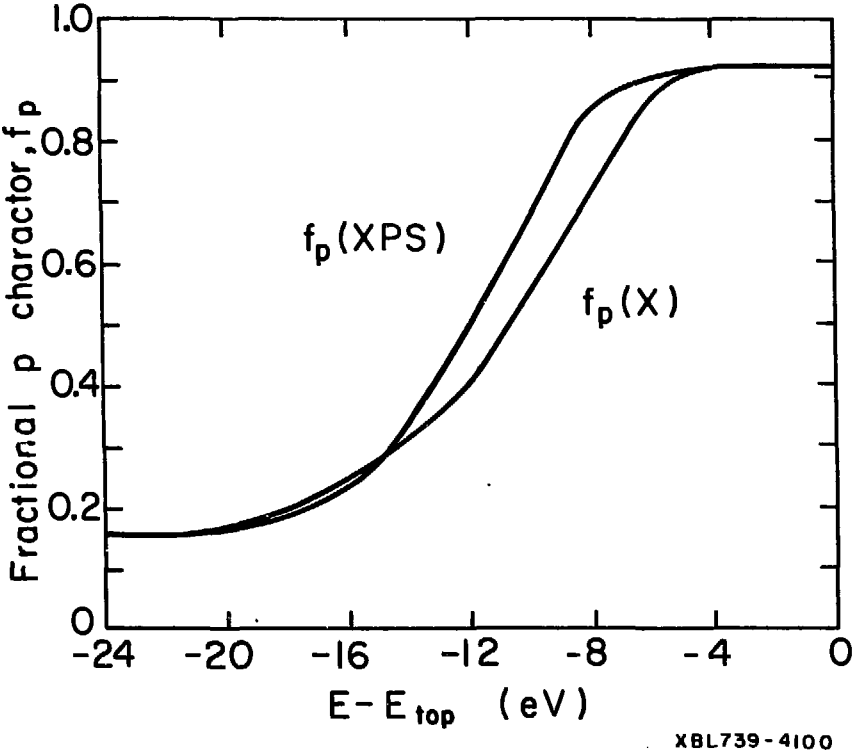
1.0
0.8
0.6
0.4
0.2
0
Fractional p character, f_p
f_p(XPS)
f_p(X)
-24
-20
-16
-12
-8
-4
0
E - E_{top} (eV)
XBL739-4100

Fig. 5

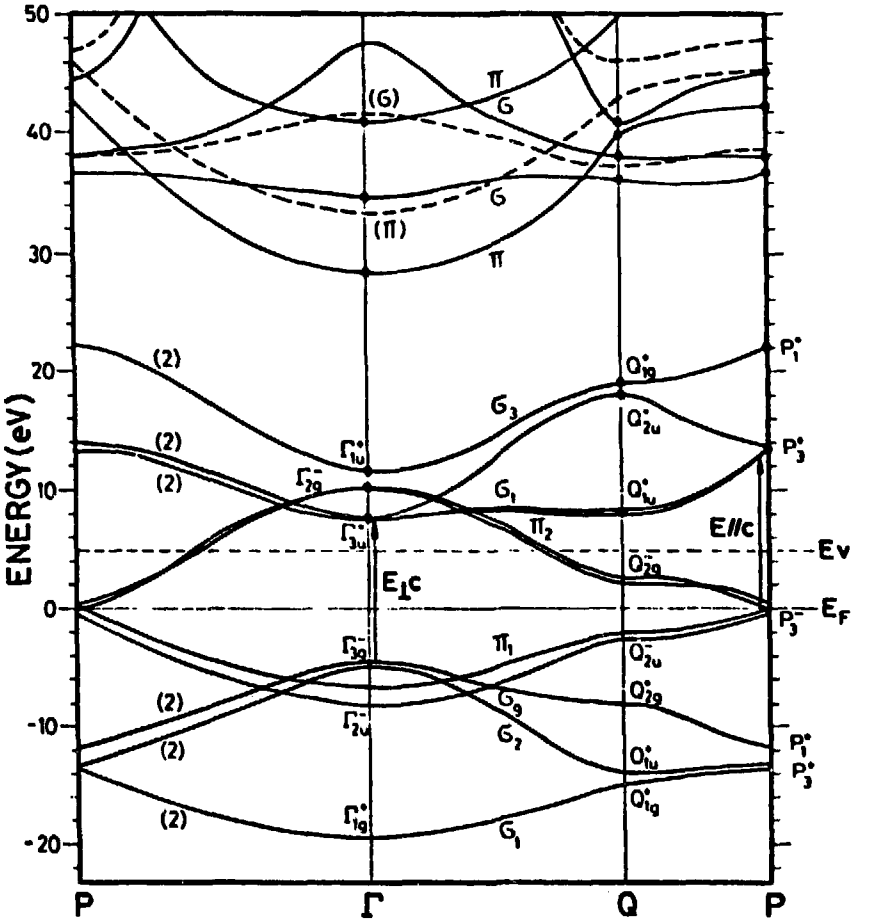

XBL 7311-1403

Fig. 6

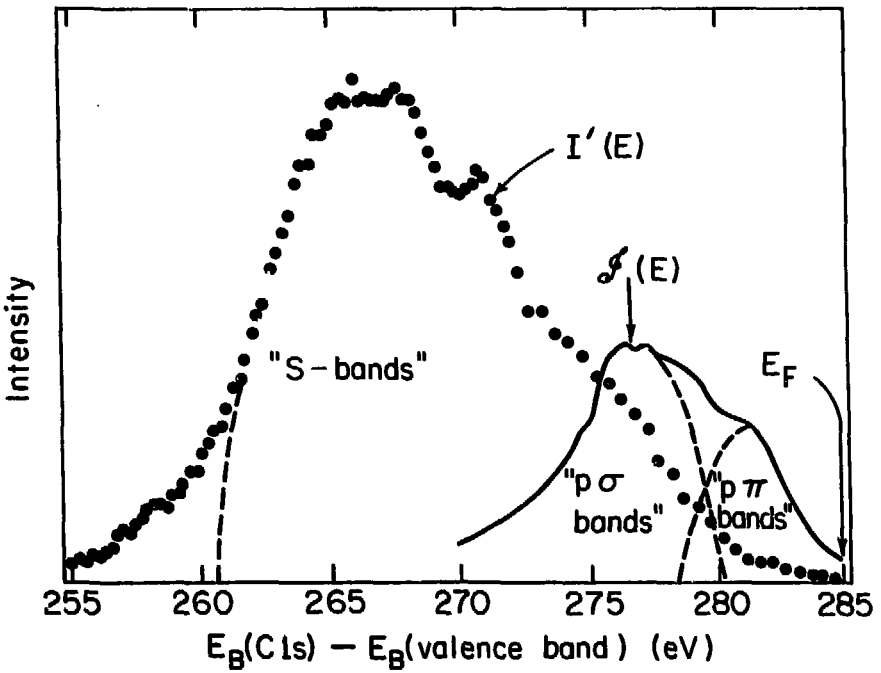

XBL739-4098

Fig. 7

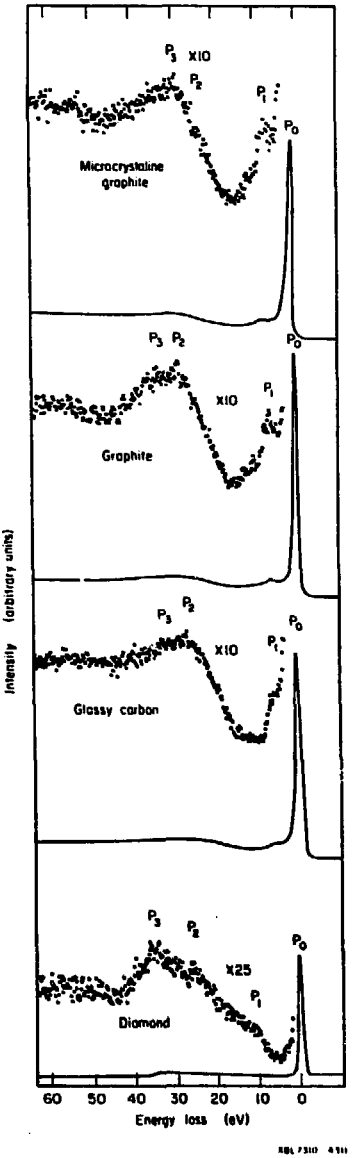
P3 x10
P2
P1
P0
Microcrystaline graphite
P3 P2
P0
x10
P1
Graphite
P3
P2
P0
x10
P1
Glassy carbon
P3
P2
x25
P0
P1
Diamond
Intensity (arbitrary units)
60 50 40 30 20 10 0
Energy loss (eV)

Fig. 8

III. d-ORBITAL DIRECTED PHOTOEMISSION FROM SILVER AND GOLD*

Abstract

An angular dependence in the photoemission spectrum from d bands, heretofore unappreciated, has been predicted and observed in single crystals of silver and gold. It is a symmetry effect, and is predicted to be observable widely in d shells of transition metals and their compounds independent of photon energy.

*Work performed in collaboration with J. Stöhr, G. Apai, P. S. Wehner, and D. A. Shirley.

In this chapter we report the theoretical prediction and experimental observation of an angular dependence in the valence-band x-ray photoemission spectrum of the noble metals silver and gold. The effect reported here should be ubiquitous in valence-level d shells, as it is an essential consequence of the breakup of the d shell into two distinct irreducible representations, $t_{2g}(\Gamma_{25'})$ and $e_g(\Gamma_{12})$ in a field of cubic symmetry. Because it is a symmetry effect, we expect it to be essentially independent of photon energy, provided only that the energy is above the region where final-state effects become important.

High-purity single crystals of silver and gold were cut to produce a (100) surface orientation, polished to 1 micron smoothness and etched repeatedly, in aqua regia for gold and a 1:1 solution of $NH_4OH:H_2O_2$ for silver, to remove the damage layer formed by polishing. Back-reflection Laue patterns taken to orient the crystals after this process showed sharp diffraction features, indicating the absence of a deep damage layer.

The crystals were spot-welded to rotatable platens and inserted into a Hewlett-Packard 5950A electron spectrometer, modified for ultra-high vacuum operation. The sample preparation chamber was then baked to achieve a base pressure of $\sim 8 \times 10^{-10}$ torr, and the surfaces were cleaned by argon ion bombardment. After this cleaning procedure the Cls intensity indicated less than 0.1 of a monolayer. The oxygen 1s peak was undetectable. The crystals were then heated to $\sim$800°C for 1 hr. to anneal out surface damage introduced by ion bombardment. Valence-band spectra taken on annealed and unannealed samples showed definite reproducible differences.[1-3] Numerous spectra were run with both elements,

analyzing electrons emitted along the [100], [111], and [110] directions. These directions were selected by tilting and azimuthally rotating the crystals. The orientation was adjusted optically to a precision of $\pm\frac{1}{2}$ degree. We estimate the total angular accuracy of ±2 degrees or less, with a spectrometer solid angle of acceptance of ±3 degrees. The take-off angles were high in each case (90°, 35.3°, and 45°, respectively). Although we studied both annealed and unannealed ("amorphous surface") single crystals, we shall for brevity present and discuss only those spectra taken with photoelectrons propagating along the [100] and [111] directions from well-annealed samples, as these directions show the largest effects and are the simplest to interpret.

Figures 1a,b and 2a,b show the photoemission spectra obtained for photoelectrons propagating along the [100] and [111] axes for silver and gold. The spectra are distinctively different, the major differences being the change of the peak height ratios for the high- and low-binding-energy d-band peaks, and the change in the shape of the leading edge of the d-band peak. The experimental resolution for the spectra shown in Figs. 1 and 2, estimated from the Au $4f_{7/2}$ full width half maximum (FWHM) was Au[100]:1.2 eV, Au[111]:0.8 eV, Ag[100]:1.0 eV, and Ag[111]:0.8 eV, respectively.

To develop a physical understanding of the effect, consider photoemission from the point $\Gamma(\vec{k} = 0)$ in the Brillouin zone (BZ). This is the ligand field theory case. In the absence of spin-orbit splitting, the five degenerate d states are split into $t_{2g}(\Gamma_{25'})$ and $e_g(\Gamma_{12})$ levels. If the final state is represented as a plane wave, photoemission from

the t_{2g} orbitals in [100]-type directions is forbidden because matrix elements of the form

$$(e^{iq_x x} | \vec{p} | d_{xy}\ ,\ d_{yz} \text{ or } d_{xz}) \qquad (1)$$

are forbidden by symmetry, while photoemission from t_{2g} states is allowed along the [111] axes. The exact reverse is true for the e_g states. Thus by selecting the photoelectrons emitted in the [100] and [111] directions one could observe a t_{2g} peak or an e_g peak alone. It may be argued that a plane wave description of the final state is unrealistic since such a state would not be orthogonal to the initial core states. However, as was recently shown by Gadzuk[4] a more realistic description of the final state does not significantly alter the initial state symmetry effects discussed here. For photoexcitation from d-states into the dominant f partial-wave channel, photoemission along the [100] direction is also found to be forbidden for t_{2g} and allowed for e_g states.[4] For photoelectrons emitted along the [111] direction the emission intensity for e_g states is no longer zero but still considerably lower than for t_{2g} states.[4] Spin-orbit coupling would reduce the anisotropy effect by mixing the t_{2g} and e_g states and splitting the t_{2g} level into Γ_8 and Γ_7 states; however, even for Au, the crystal field is still dominant, and the t_{2g}-e_g mixing is only 15%.

The effect persists throughout the BZ. Following Ehrenreich and Hodges[5] we can write the initial band state $|j>$ in the tight binding form

$$|j> = \psi^j_k(\vec{r}) = N^{-1/2} \sum_{\ell\mu} e^{i\vec{k}\cdot\vec{R}_\ell}\ \beta^j_\mu(\vec{k})\ \ \Phi_\mu(\vec{r} - \vec{R}_\ell) \qquad (2)$$

Here $\phi_\mu(\vec{r}) = R(r)d_\mu(\theta_r,\phi_r)$ are atomic wavefunctions, where the $d_\mu(\theta_r,\phi_r)$ are the e_g and t_{2g} functions given in Table I of reference 6. The coefficients $\beta_\mu^j(\vec{k})$ are obtained from the band structure calculation.[5,7] The cross section at a general $\vec{k}$ point is given by

$$\sigma(\vec{k}, j, \vec{q}) \sim \frac{|\vec{q}|}{\hbar\omega} \left| <e^{i\vec{q}\cdot r} |\vec{p}|j> \right|^2 \qquad (3)$$

Here we have assumed a plane wave final state. We shall neglect the s-part of the initial state wavefunction since its transition matrix element is small. In any case it may be omitted in discussing angular effects since it contribute no anisotropy to the photoemission spectrum. Equation (3) may be evaluated to yield[6]

$$\sigma(\vec{k}, j, \vec{q}) \sim \frac{1}{\hbar\omega} \sum_G |\vec{q}|^3 \left| \sum_\mu \beta_\mu^j(\vec{k})\, \phi_\mu(\vec{q}) \right|^2 \delta(\vec{k} - \vec{q} - \vec{G}) \qquad (4)$$

where $\phi_\mu(\vec{q}) = f(q)\ d_\mu(\theta_q,\phi_q)$ is the Fourier transform of the initial state wavefunction $\phi_\mu(\vec{r})$ and $\vec{G}$ is a reciprocal lattice vector. For a given photon energy (and hence $|\vec{q}|$), equation (4) simplifies to

$$\sigma(\vec{k}, j, \vec{q}) \sim \sum_G \left| \sum_\mu \beta_\mu^j(\vec{k})\ d_\mu(\theta_q,\phi_q) \right|^2 \delta(\vec{k} - \vec{q} - \vec{G}) \qquad (5)$$

In the XPS regime (Al K_α excitation) the final state wavevectors $\vec{q}$ are more than an order of magnitude larger than the maximum $\vec{k}$ in the first BZ. Thus the ±3° spectrometer acceptance angle is sufficiently large that $\vec{k}$ may be any value within the first BZ and still satisfy the $\vec{k}$-conserving delta function. However, in order for a transition to occur both $\vec{k}$ and energy must be conserved. At this point one must

realize that the true eigenstates of the (assumed infinite) crystal at 1500 eV above E_F are not plane waves but Bloch states of the form $e^{i\vec{k}\cdot\vec{r}} \sum_G a_G e^{i\vec{G}\cdot\vec{r}}$. The distinction is crucial. A plane wave final state model would predict that the bands become increasingly steep at higher energies and remain up to 48-fold degenerate. This would imply that for the case of angle-resolved measurements it becomes even more difficult to conserve both E and $\vec{k}$ at higher energies resulting in only a small region of the initial states in the first BZ being sampled. The high energy band structure calculations of Hoffstein and Boudreaux[8] for Al show that this result is a spurious artifact of the plane-wave model. The mixing of the plane waves under the influence of the crystal potential lifts the large degeneracies of the plane wave bands, and leads to many more nondegenerate bands which fill the gaps in the free-electron dispersion relation. In addition, the individual bands thus formed are less steep than their free-electron counterparts. The implications can be seen quite easily from an examination of Fig. 6 of Hoffstein and Boudreaux. The free-electron picture places unrealistically severe restrictions on the initial states which may undergo photoemission due to the unphysical gaps and degeneracies in its band structure. It is apparent from extrapolating the results of Hoffstein and Boudreaux that at Al K_α energies, and with our angular resolution of ±3°, all initial states in the first BZ are sampled. This points out the essential difference between the experiment presented here and low-energy UV angular resolved photoemission experiments.[9,10] At photon energies of $h\nu \lesssim 20$ eV and small spectrometer acceptance angles the experimental

restriction on $\vec{q}$ places a stringent restriction on $\vec{k}$ since $\vec{q}$ and $\vec{k}$ are of comparable magnitude. The dominant effect at low energies is the sampling of initial states only in small regions of the BZ. The matrix element effects we discuss here are present, but are obscured by this larger effect. The high energy experiment is angle-integrated with respect to the sampling of initial states, but angle-resolved with respect to the real-space orientation of the basis orbitals which lead to the matrix-element dependent effects reported here. Finally, we note that it is still approximately correct to describe our angle-resolved measurements by a matrix element involving a single plane wave final state because at XPS energies the plane waves that are strongly mixed by the lattice potential have nearly the same direction of propagation, i.e., into the analyzer. For the case of XPS, equation (5) may thus be simplified to

$$\sigma(\vec{k}, j, \vec{q}) \sim \left| \sum_{\mu} \beta_{\mu}^{j}(\vec{k}) \quad d_{\mu}(\Theta_q,\phi_q) \right|^2 \qquad (6)$$

and the angular intensity distribution may be discussed in terms of the functions $d_{\mu}(\Theta_q,\phi_q)$. Let us illustrate this by considering the two cases $\vec{q}\parallel[100]$ and $\vec{q}\parallel[111]$. For $\vec{q}\parallel[100]$ we have $\Theta_q = 90°$, $\phi_q = 0°$ and hence (compare Table I of reference 6) $d_{x^2-y^2} = -\sqrt{3}\, d_{3z^2-r^2} \neq 0$ and d_{xy}, d_{yz}, $d_{xz} = 0$. Thus the cross section given by equation (6) is just the e_g projection. Likewise for $\vec{q}\parallel[111]$ ($\Theta_q = 54.7°$, $\phi_q = 45°$) we obtain $d_{x^2-y^2} = d_{3z^2-r^2} = 0$ and $d_{xy} = d_{yz} = d_{xz} \neq 0$. In this case the cross section is given by the t_{2g} projection.

The anisotropy effects stand out most clearly in the gold spectra

(Fig. 1). In the [100] spectrum the higher binding energy (E_B) peak is relatively less intense (in terms of peak heights; an area ratio measurement would be ambiguous), and the lower E_B peak has relatively less intensity on the low E_B side. Both effects are predicted in the calculations. The first arises because of a slightly lower density of e_g character in the bands that contribute to the high binding-energy peak. Those bands must be considered in detail to explain this effect quantitatively; qualitatively it can be attributed to a tendency for bonding to nearest neighbors at the "bottom" of the d band. The second effect can be identified readily with the top occupied band, which acquired predominantly t_{2g} character at L, K, and X in the BZ. This band is responsible for nearly all of the state density in the low E_B shoulder of the low-E_B peak, which is thus absent in the [100] spectrum.

Both of the above effects are also clearly present in silver (Fig. 2), although the narrower bandwidth precludes a detailed analysis. The peak height ratio in silver is 1.16(2) for [111] and 1.27(2) for [100]. Note also the relatively gradual onset of the d-band emission in the Ag[100] spectrum, similar to the case of Au. This arises in both cases because the least tightly bound "pure" d-states lie about the L point where the bands are highly t_{2g}-like. These states are invisible in the [100] experiment and thus the onset of d-emission is effectively suppressed in both Au and Ag[100] spectra. The observation of this anisotropic angular distribution in two lattices and the close correspondence between theory and experiment appear to establish this effect unambiguously as arising from directed d orbitals.

d-orbital directed photoemission should be a rather general phenomenon. It should be present in the valence bands of other transition metals, and in some (e.g., platinum) it may be more pronounced than in silver or gold. Because it is a symmetry effect, it should be present at all photon energies, although the interaction between the final state and the ion core potential will in general lead to more complicated angular distributions for low photon energy. Remeasurement of XPS spectra of transition metals using oriented single crystals may therefore be expected to yield useful new information about the valence bands. Even more distinctive effects should be present in transition-metal complexes, for which the t_{2g} and e_g orbitals are resolved in energy. There may also be diagnostic applications to orientational problems in absorbates on single crystals.

d-orbital directed photoemission has been observed before, but not explained. Nilsson and Eastman[11] studied photoemission from single-crystal silver films, but did not use photon energies high enough to reach the d bands. Shirley[12] observed variations in the gold valence-band spectrum with crystal face, but gave no interpretation. These results can now be interpreted in terms of the electron propagation direction implied by the analyzer geometry; this interpretation is consistent with Fig. 1. We also note that indirect evidence for this effect has been available for some time in the different appearance of single-crystal[12] and polycrystalline[13] gold valence-band spectra. Recently Fadley[14] made the important step of correlating the spectrum variation with electron propagation direction, obtaining data very similar to the top two panels of Fig. 1. The above model appears to explain all

of these earlier results.

REFERENCES

1. There were observable changes in the spectra on annealing. Evidence for differences in XPS valence-band spectra were reported for semiconductors by Ley, et al. (Ref. 2) and for metals by Hüfner, et al. (Ref. 3).

2. L. Ley, S. Kowalczyk, R. A. Pollak, and D. A. Shirley, Phys. Rev. Letters 29, 1088 (1972).

3. S. Hüfner, G. K. Wertheim, and D. N. E. Buchanan, Solid State Comm. 14, 1173 (1974).

4. J. W. Gadzuk, Phys. Rev. B12, 5608 (1975).

5. H. Ehrenreich and L. Hodges, Methods in Computational Physics, Vol. 8, 149 (1968).

6. J. W. Gadzuk, Phys. Rev. B10, 5030 (1974).

7. N. V. Smith, Phys. Rev. B3, 1862 (1971).

8. V. Hoffstein and D. S. Boudreaux, Phys. Rev. B2, 3013 (1970).

9. N. V. Smith and M. M. Traum, Phys. Rev. B11, 2087 (1975).

10. P. O. Nilsson and L. Ilver, Solid State Commun. 17, 667 (1975).

11. P. O. Nilsson and D. E. Eastman, Physica Scripta 8, 113 (1973).

12. D. A. Shirley, Phys. Rev. B5, 4709 (1972).

13. K. Siegbahn, D. Hammond, H. Fellner-Feldegg, and E. F. Barnett, Science 176, 245 (1972).

14. C. S. Fadley, in Faraday Discussion on Electron Spectroscopy of Solids and Surfaces, Vancouver, British Columbia, July 1975 (to be published), and private communication.

FIGURE CAPTIONS

Fig. 1. X-ray photoemission spectra along [100] and [111] axes, partial E_g and T_{2g} state densities, and band structure of gold metal. Note changes in relative peak heights from [100] (E_g) to [111] T_{2g}, and absence of T_{2g} shoulder at 2-3 eV in [100] spectrum.

Fig. 2. X-ray photoemission spectra along [100] and [111] axes, partial E_g and T_{2g} state densities, and band structure of silver metal. As in gold the peak height ratios change with E_g/T_{2g} character, and the low-E_B edge of the d-band peak is steeper in the [111] case.

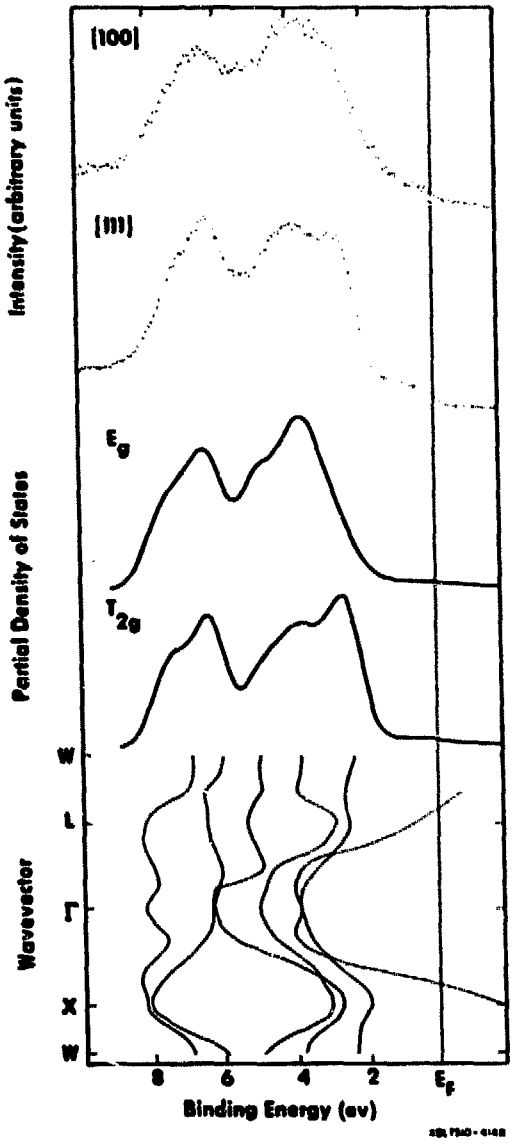
[100]
[111]
Intensity (arbitrary units)
E_g
T_{2g}
Partial Density of States
W
L
Γ
X
W
Wavevector
8
6
4
2
E_F
Binding Energy (ev)

Fig. 1

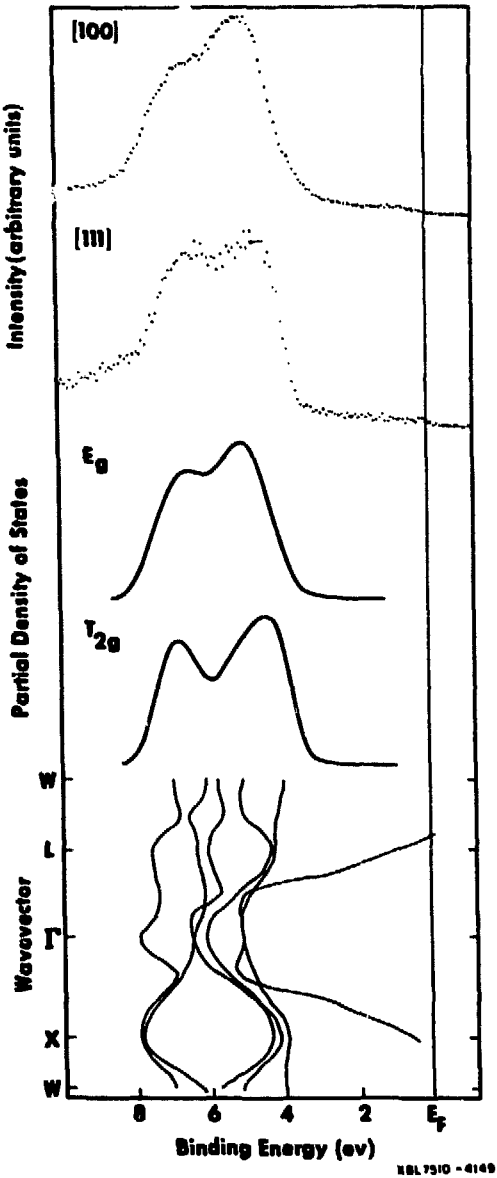
[100]
[111]
Intensity (arbitrary units)
Partial Density of States
E_g
T_{2g}
Wavevector
W
L
Γ
X
W
8
6
4
2
E_F
Binding Energy (ev)
XBL 7510 - 4149

Fig. 2

IV. PHOTOEMISSION FROM Cu VALENCE BANDS USING 50 - 175 eV SYNCHROTRON RADIATION*

Abstract

Photoemission spectra of the 3d valence band of polycrystalline Cu were studied using synchrotron radiation of energy 50 eV $\leq h\nu \leq$ 175 eV. The detailed shape of the spectrum was found to change distinctly with photon energy. The observed energy dependence was compared to calculated photoemission energy distributions (PED's) assuming a direct transition model. PED's obtained with this model predicted the experimental intensity distribution quite well for $h\nu > 70$ eV and $h\nu > 120$ eV but failed in the region $h\nu \approx 90$ eV. Fair agreement between experiment and theory was obtained when momentum broadening in the final state was included. The largest broadening was required around $h\nu = 90$ eV. A minimum in the photoelectron mean free path at this energy is discussed as a possible source of broadening. The observed changes in spectral shape for 50 eV $\leq h\nu \leq$ 70 eV are attributed to direct transitions; the changes are found to arise mainly from the angular part of the transition matrix element.

*Work performed in collaboration with J. Stöhr, P. S. Wehner, G. Apai, and D. A. Shirley.

A. Introduction

The photoemission energy distribution (PED) which is obtained by exciting valence electrons in solids depends mainly on three quantities: the initial density of states, the photoexcitation matrix element, and the final density of states. The latter two define the photoemission cross-section. In the past two basic types of cross section effects have been reported in photoemission spectroscopy of solids. In x-ray photoemission spectroscopy (XPS) frequency dependent variations in photoemission intensity from s-, p-, d-, and f-derived valence electrons have been observed.[1] They arise from different radial matrix elements for the respective transitions.[1] In ultraviolet photoemission spectroscopy (UPS) variations with photon energy in the PED's obtained by exciting valence electrons are usually discussed in terms of final state effects which are responsible for the observed line positions and transition matrix element modulations that determine the line intensities.[1]

The photoemission studies on Cu (3d) valence electrons reported here are in a sense a simple extension of the UPS studies mentioned above. However, at the photon energies (50 eV - 175 eV) used for our angle integrated experiments on polycrystalline samples, several new phenomena arise. In raising the photon energy the number of accessible final states increases.[2] While the UPS regime transitions occur only at special $\vec{k}$ points of the Brillouin zone (BZ) at higher photon energies a considerably larger part of the zone is sampled. Therefore the positions of the peaks which constitute the PED predominantly reflect the initial density-of-states structure and are expected to remain essentially unshifted. The peak intensities on the other hand may change

significantly with photon energy because of both the angular and radial parts of the transition matrix element. The study of these intensity changes with frequency is the main purpose of the present paper.

In contrast to the situation that prevails in the UPS regime, one other point is of considerable interest at higher photon energies. The photoelectron mean free path of most materials exhibits a broad minimum between 50 - 100 eV.[3] As discussed by Feibelman and Eastman[4] such inelastic damping which restricts the source region of the photocurrent near the surface results in an uncertainty or spread of the final state momentum component perpendicular to the surface.

In the following Sections B.1. and B.2. we describe the experimental arrangement and results, respectively. In Section C.1. we present a simple model to calculate the Cu 3d PED's under the assumption of direct optical transitions. In Section C.2. we show how to include momentum broadening in the final state in a simple stochastic fashion. We discuss the results of such calculations in Sections D.1. and D.2. In the concluding Section E we consider some future problems which have been stimulated by the present investigation.

B. Experiment

1. Experimental Arrangement

Experiments were performed using synchrotron radiation from the storage ring SPEAR at the Stanford Linear Accelerator (SLAC). The ultra-high vacuum grazing incidence monochromator has been described in detail elsewhere.[5] Photoelectrons were detected by a double pass, electrostatic deflection cylindrical mirror analyzer (CMA) operated in the retarding mode (constant resolution 0.35 eV).[6] Samples were prepared by *in situ*

evaporation of Cu from a tungsten filament onto a stainless steel substrate. The maximum pressure reached during evaporation was 2×10^{-3} torr. Experiments were carried out at $\sim 1 \times 10^{-9}$ torr.

2. Experimental Results

Experimental results for Cu are displayed in Fig. 1. Common features of all spectra are the three peaks at ~2.4 eV, ~3.5 eV, and ~4.6 eV binding energy (BE) relative to the Fermi level. The most distinct changes in the shape of the VB spectra occur between 50 and 70 eV. While the peak positions remain essentially unshifted the intensity of the peak at 3.4 eV BE increases with photon energy. Above 70 eV this trend continues in a less spectacular way. At the highest photon energies the spectra seem to approach the PED observed with Aℓ K_α radiation[7] (compare Figure 2a).

C. Theory

1. The Direct Transition Model

For the calculation of the PED's we have employed the familiar three step model of photoemission.[8] We assume independent excitation, transport and escape processes. The excitation process from an initial state j to a final state f at a general point $\vec{k}$ of the Brillouin zone (BZ) is described by a matrix element $t_{fj}(\vec{k})$. The matrix element is calculated in the dipole velocity approximation under the assumption of crystal momentum conservation during the excitation process (cp. Appendix A). Transport of the excited photoelectron to the surfaces is described by a term $D_f(\vec{k})$ which is proportional to the group velocity of the electron (cp. Appendix B). In our case of angle-integrated photoemission with final state energies much larger than the initial state band width a

surface transmission term may be neglected. The PED is then given by

$$I(E, \hbar\omega) \sim \sum_{j,f} \int_{BZ} d^3k \, D_f(\vec{k}) \, |t_{fj}(\vec{k})|^2 \, \delta(E_f(\vec{k}) - E_j(\vec{k}) - \hbar\omega) \, \delta(E - E_j(\vec{k})) \tag{1}$$

Details of the k- integration are discussed in Appendix C. The term $|t_{fj}(\vec{k})|^2 \, \delta(E_f(\vec{k}) - E_j(\vec{k}) - \hbar\omega)$ in equation (1) corresponds to the photoemission cross section. Let us discuss it first.

Evaluation of the cross section term requires the knowledge of initial- and final-state energies and wave functions. At excitation energies larger than 50 eV the description of the final Bloch state is a nontrivial problem, as band structure calculations generally do not exist at such high energies.[9] We shall therefore describe our final state by a free-electron model, for which the eigenstates in the reduced zone scheme are given by[10]

$$E_f(\vec{k}) = \frac{\hbar^2}{2m} |\vec{k} + \vec{G}|^2 \tag{2}$$

Here $\vec{k}$ is the crystal momentum within the first BZ and $\vec{G}$ is a reciprocal lattice vector. The "zero" of our free electron energy bands was adjusted to the bottom of the 4s type bands obtained from a tight-binding calculation described below. The final state wave function is taken to be an orthogonalized plane wave (OPW), also discussed in more detail below and in Appendix A. Smith's[11] parameterization of the linear combination of atomic orbital (LCAO) interpolation scheme of Hodges, Ehrenreich, and Lang[12] was adopted to yield the initial-state energies $E_j(\vec{k})$ and the coefficients $a_m^j(\vec{k})$ for the corresponding wave functions[12]

$$|j> = N^{-1/2} \sum_{\ell,m} e^{i\vec{k}\cdot\vec{R}_\ell} a_m^j(\vec{k})\, D_m(\vec{r} - \vec{R}_\ell) \qquad (3)$$

Here $D_m(\vec{r}) = R_d(r)\, d_m(\theta_r, \phi_r)$ are atomic d-wave functions. The real angular functions $d_m(\theta, \phi)$ are tabulated in Table I of reference 13. The radial parts $R_d(r)$ in the form of Slater orbitals were taken from reference 14. Equation (3) is the d-projection of the total LCAO wave function. For our calculation the s-part of the initial state wave function has been neglected because its transition matrix element is relatively small. The sum in equation (3) extends over the five angular d-functions and neighbor positions $\vec{R}_\ell$ in the fcc lattice. Assuming an OPW final state the matrix element $t_{fj}(\vec{k}) = <f|\vec{A}\cdot\vec{p}|j>$ may be evaluated as (Appendix A)

$$|t_{fj}(\vec{k})|^2 \sim C^2 \sum_{\vec{G}} \left| \sum_m a_m^j(\vec{k}) \; \vec{A}\cdot \left| \vec{q}\, D_m(\vec{q}) + \sum_n P_n(\vec{q})\, \vec{M}_{mn} \right| \right|^2 \delta(\vec{k} + \vec{G} - \vec{q}) \qquad (4)$$

Here C is a normalization constant for the OPW (equation A2), $\vec{G}$ is a reciprocal lattice vector, $\vec{A}$ is the vector potential and $\vec{q} = \vec{k} + \vec{G}$ is the wave vector of the photoelectron. The sum over n involves all wave functions of occupied atomic states $P_n(\vec{r})$ for which the transition matrix element $\vec{M}_{mn} = <D_m(\vec{r})|\vec{\nabla}|P_n(\vec{r})>$ (compare Appendix A) does not vanish. In our case of photoemission from 3d states only the atomic 2p and 3p functions need to be considered. $D_m(\vec{q}) = f_d(q)\, d_m(\theta_q, \phi_q)$ and $P_n(\vec{q}) = f_p(q)\, p_n(\theta_q, \phi_q)$ are Fourier transforms of the atomic d and p wave functions $D_m(\vec{r})$ and $P_n(\vec{r})$ respectively (Appendix A). The functions $p_n(\theta, \phi)$ are listed in Table III of Reference 13. The δ-function in

equation (4) represents the direct transition requirement of momentum conservation. For polycrystalline samples effects of light polarization may be neglected in evaluating equation (4).

2. Momentum Broadening in the Final State

The direct transition model presented above may easily be extended to include momentum broadening in the final state. While the physical reasons for such an extension are discussed in more detail below we will at this point present a simple stochastic way to include momentum broadening into the calculation. The idea of momentum broadening is to smear only the direction of the final state momentum vector $\vec{q}$ (i.e. the angles ϕ_q and Θ_q). The absolute value $|\vec{q}|$, which also defines the final state energy, is conserved. We employ the same equations as for the direct-transition case, except that we are less restrictive in the description of the final state. For a given free electron final state $\vec{k} + \vec{G}$ we allow all final states with wave vectors $\vec{p}$ and energy $E_f^1(\vec{k}) = \frac{\hbar^2}{2m} |\vec{p}|^2$ which satisfy $(\vec{k} + \vec{G}) - \vec{\Delta}|2 \leq \vec{p} \leq (\vec{k} + \vec{G}) + \vec{\Delta}|2$ and the energy conserving δ-function $\delta(E_f^1(\vec{k}) - E_j(\vec{k}) - \hbar\omega)$ in equation (1). Since our calculations apply for a polycrystalline sample we assume all directions $(\vec{k} + \vec{G})_i$ $(i = x,y,z)$ to be equally broadened where $\Delta_i = |\vec{k} + \vec{G}|B/100$. The broadening parameter B is chosen to minimize the difference between experimental and calculated PED's. The effect of the broadening factor B is to create more possible final states at a given $\vec{k}$ point. While all allowed final states are required to have the same energy $E_f^1(\vec{k})$ they are, however, characterized by different momentum vectors $\vec{p}$. Except for substituting $E_f^1(\vec{k})$ for $E_f(\vec{k})$ in equation (1) and $\vec{p}$ for $\vec{k} + \vec{G}$

in equation (4) the momentum-broadening and direct-transition calculations are identical.

D. Results and Discussion

1. Direct Transitions

Results of the calculation assuming direct transitions (compare Appendix C) are shown in Fig. 3a. The calculation predicts essentially constant line positions; i.e., the three-peak structure mentioned earlier, over the entire energy range, in complete agreement with experiment. When compared to the experimental PED's in Fig. 3b (which have been corrected for inelastic background) reasonable agreement in peak intensities exists for $h\nu < 70$ eV and $h\nu \geq 120$ eV. The observed peak intensities are not reproduced well around $h\nu = 90$ eV.

It is interesting to explore the origin of the calculated changes in peak intensities. At a general $\vec{k}$ point the final state of an allowed direct transition (i.e., $E_f(\vec{k}) = E_j(k) + \hbar\omega$) is characterized by a reciprocal lattice vector $\vec{G}$ (compare equation (2)).[10] Because of the δ-function in equation (4) the direction of $\vec{G}$ also fixes the direction of $\vec{q} = \vec{k} + \vec{G}$, i.e., the direction along which the photoelectron is allowed to leave.[16] The direction of $\vec{q}$ enters through the angular terms of the Fourier integrals $D_m(\vec{q})$ and $P_n(\vec{q})$ in equation (4) and it is this angular dependence which largely determines $|t_{fj}(\vec{k})|^2$. This is especially true for Cu since the 3d wave function does not have a radial node.[17] Fig. 4 shows a plot of the angle averaged radial dipole matrix element squared (compare equation A17) versus the kinetic energy of the photoelectron. It is seen that the energy dependence of the radial part of equation (4) is negligible over the width ($\sim$3 eV) of the

3d valence band. Thus, only the angular part of the transition matrix element can cause changes in relative peak intensities within the Cu valence band. The differences in peak intensities with photon energy is then easily understood in our model. At different photon energies the final states at a given $\vec{k}$ point will be characterized by different $\vec{G}$ vectors, leading to different angular matrix elements.

The effect of the angular as compared to the radial matrix element is demonstrated in Fig. 5. Here a calculation with an angle integrated, or because of the reasons given above essentially constant matrix element $\overline{|t_{fj}|^2}$ (dashed curve), is compared with a calculation including the total matrix element $|t_{fj}|^2$ (solid curve) for $h\nu$ = 50 eV and $h\nu$ = 90 eV. The former calculation yields similar results at both photon energies while the latter shows strong modulation effects. The difference in the angle integrated curves at $h\nu$ = 50 eV and $h\nu$ = 90 eV is a consequence only of final-state effects, which arise through the conserving function $\delta(E_f(\vec{k}) - E_j(\vec{k}) - \hbar\omega)$ in equation (1).

It is interesting to note the spectral variations implied by our model at higher photon energies. As the photon energy is raised the number of available final states increases. In the limit of large photon energy this causes the PED's to resemble the initial-state band structure shown in Fig. 2b. In the high-photon-energy limit, modulation effects due to the transition matrix element are also expected to be small, because the various allowed final states result in an effective angular integration. At this point we note that Nemoshkalenko, et al.[18] included angle-integrated matrix elements to account for the discrepancy between the measured Cu XPS valence band spectrum and the calculated

density of states. They claimed that this discrepancy arises because electrons with e_g symmetry have a higher transition probability than those with t_{2g} symmetry. Our expression for the angle-integrated matrix element (compare equation A17) is in disagreement with their result. Furthermore, equation (A17) reveals that for a polycrystalline sample the e_g and t_{2g} components of the density of states cannot be distinguished from one another. However, such a separation is possible in angle-resolved photoemission from single crystals, which has been reported for the cases of Ag and Au using Aℓ K_α radiation.[19]

2. Momentum Broadening in the Final State

In Fig. 3c we present the results of a calculation in which momentum broadening in the final state has been calculated. We have chosen the respective broadening factors listed in Fig. 3c to achieve optimum agreement between the calculated and experimental (Fig. 3b) PED's. Except for $h\nu$ = 120 eV all calculated curves were found to be quite sensitive to the choice of B, a finding which is demonstrated in more detail in Fig. 6. The calculated PED's including $\vec{k}$-broadening in the final state (Fig. 3c) are found to be in good agreement with the experimental spectra shown in Fig. 3b, except for the slightly too-pronounced peak structure. However, this difference arises entirely from the initial state band structure rather than from cross section effects. This is confirmed by Fig. 2b where the Cu 3d density of states (compare Appendix C) is compared to the density of states measured with Aℓ K_α radiation (Fig. 2a). Note that the peak structure is too pronounced generally and in particular the middle peak is too high.

The success of our calculation, which includes momentum broadening in the final state in describing the experimental, PÉD's is striking. Its description of the experimental spectra is considerably better than that obtained by the pure direct transition model. The fundamental difference between the two theoretical models lies in the description of the final state. To some extent the momentum broadening calculation covers up inadequacies in the description of the final state. It may be argued that the direct transition model does not reproduce the experimental spectra very well because of a poor description of the final state. This is indeed a problem since mixing of the various free-electron final states by the crystal potential has been ignored. The inclusion of momentum broadening somewhat simulates these effects. A direct-transition calculation of the kind presented here is not a stringent test because we are dealing with angle-integrated photoemission from a polycrystalline sample. In this case the whole BZ is sampled because all allowed transitions are also detected.

Despite the simplicity of the final state description employed in our direct transition calculation it is nevertheless very interesting to explore a possible physical reason for momentum broadening in the final state. As has been discussed in detail by Feibelman and Eastman[4] and recently by Grobman, Eastman, and Freeouf[20] and Feuerbacher and Willis,[21] momentum broadening in the final state may arise from a minimum in the photoelectron mean free path. Such a minimum is indeed known to occur in the energy range studied in the present investigation.[3] The magnitude of the broadening factors in Fig. 3c indicate that the region of highest surface sensitivity occurs around $h\nu$ = 90 eV (or a

kinetic energy of 87 eV), which agrees remarkedly well with the minimum of the mean-free-path versus energy curve in reference 3. It is interesting that in the energy range that is most highly surface sensitive the PED's resemble the one-electron density of states of the bulk. Final-state momentum broadening thus tends to weaken angular matrix element effects in photoemission. This is also clearly revealed by the model calculation in Fig. 6.

D. Conclusion

The experiments and calculations presented here may be regarded as a step toward understanding the influence of cross section and surface effects which arise in the transition region between UPS and XPS. An extension of such studies to other systems, in particular to 4d and $5d^{22}$ metals, seems to be very promising. Angle-resolved photoemission from single crystals in the soft x-ray range is another interesting problem which might help to clarify the role of cross-section and/versus surface effects. Finally, we hope that calculations which treat photoemission as a scattering problem[23] may be stimulated by the present investigation. Experimental and theoretical investigations of this kind seem to be most important in contributing to a quantitative understanding of the photoemission process per se in solids.

E. Appendix A: Dipole Matrix Elements

In evaluating the dipole matrix element $t_{fj}(\vec{k}) = \langle f|\vec{A}\cdot\vec{p}|j\rangle$ we follow Gadzuk[13] except that we assume an OPW instead of a plane wave (PW) final state. The initial state $|j\rangle$ is given by equation (3). The OPW final state is

$$|f\rangle = C\left\{|PW\rangle - \sum_n \langle P_n(\vec{r})|\ PW\rangle\ |P_n(r)\rangle\right\} \tag{A1}$$

where

$$C = (\langle PW\ |\ PW\rangle - \sum_n |\langle P_n(\vec{r})|\ PW\rangle|^2)^{-1/2} \tag{A2}$$

As has been discussed in Section C.1. the sum over n involves the atomic p-functions only. Following Gadzuk[13] the matrix element $t_{fj}(\vec{k})$ may now be readily evaluated in the dipole velocity approximation ($\vec{p} = im\vec{V}$) to yield equation (4).

The evaluation of the Fourier transforms $D_m(\vec{q})$ and $P_n(\vec{q})$ and the matrix element $\vec{P}_{mn}$ which occur in equation (4) should be discussed in more detail. The atomic d function has the general form

$$D_m(\vec{r}) = R_d(r)\ d_m(\theta_r, \phi_r) \tag{A3}$$

For Cu(3d) the radial part has the general Slater form

$$R_d(r) = ar^2 e^{-\alpha r} \tag{A4}$$

The atomic p functions are

$$P_m(\vec{r}) = R_p(r)\ P_m(\theta_r, \phi_r) \tag{A5}$$

The radial part of the 2p and 3p functions can be written

$$R_p(r) = cre^{-\gamma r} + dr^2e^{-\delta r} \tag{A6}$$

For our calculations the coefficients for the radial parts of the p and d wave functions were taken from reference 14. The Fourier transforms of the atomic d-function (A3) is

$$D_m(\vec{q}) = \int d^3r e^{-i\vec{q}\cdot\vec{r}} D_m(\vec{r}) \tag{A7}$$

$$= f_d(q)\, d_m(\theta_q, \phi_q) \tag{A8}$$

where

$$f_d(q) = -4\pi \int r^2 j_2(qr) R_d(r) dr \tag{A9}$$

For the atomic p functions the Fourier transform is

$$P_m(\vec{q}) = \int d^3r e^{-i\vec{q}\cdot\vec{r}} P_m(\vec{r}) \tag{A10}$$

$$= f_p(q)\, P_m(\theta_q, \phi_q) \tag{A11}$$

where

$$f_p(q) = -4\pi i \int r^2 j_1(qr)\, R_p(r) dr \tag{A12}$$

The functions $j_{\ell}(qr)$ in equations (A9) and (A12) are spherical Bessel functions.[24]

The matrix element

$$\vec{M}_{nm} = \langle D_m(\vec{r}) | \vec{V} | P_n(\vec{r}) \rangle \tag{A14}$$

may be separated into a radial and angular part according to

$$\vec{M}_{mn} = \vec{L}_{mn}\, h_{dp} \tag{A15}$$

All non-vanishing components of $\vec{L}_{mn}$ are listed in Table I. The radial integral h_{dp} is given by

$$h_{dp} = \langle R_d(r) \left| \frac{\partial}{\partial r} - \frac{1}{r} \right| R_p(r) \rangle \tag{A16}$$

and its evaluation is straight forward.

Finally, the result for the angle integrated quantity $\overline{|t_{fj}(\vec{k})|^2}$ should be given. A lengthy but relatively easy calculation neglecting effects of light polarization[15] yields

$$\begin{aligned}\overline{|t_{fj}(\vec{k})|^2} \sim C^2 \Big| & 5(f_d(q))^2\, q^2 \\ & + 2(f_p(q))^2\, h_{dp}{}^2 \\ & + 4 f_d(q) f_p(q) q h_{dp} \Big| \sum_m |a_m^j(\vec{k})| \Big|^2 \end{aligned} \tag{A17}$$

From equation (A17) it is seen that for the angle integrated case the matrix element separates into an atomic part given by the wavy brackets and a wave vector dependent "band-structure" part given by the sum. This latter part is exactly the total d-projection of the density of states.

F. Appendix B: Transport Term

In evaluating the transport term we have assumed that the inelastic mean free path is much less than the photon absorption depth. The transport factor for excited electrons is then given by[1]

$$D_f(\vec{k}) \sim (\vec{s} \cdot \vec{\nabla}_k E_f(\vec{k})) \tau(E_f) \tag{B1}$$

where $\vec{s}$ is a unit vector normal to the surface and $\tau(E_f)$ is the inelastic scattering lifetime in the "random-$\vec{k}$" or "phase-space" approximation.[25] Assuming the lifetime $\tau(E_f)$ to be a slowly varying function of the electron energy and taking the free electron value for the group velocity we can approximate $D_f(\vec{k})$ for a polycrystalline sample by

$$D_f(\vec{k}) \sim |\vec{q}| \tag{32}$$

Since the photon energies used in our study are much larger than the width of the d-band the effect of the transport term (B2) on the calculated PED's (equation (1)) is very small.

G. Appendix C: Calculation of the PED's

The PED's were calculated on a mesh of 308 points in the 1/48 of the BZ defined by $k_y > k_x > k_z \geq 0$. Calculations carried out at a larger number of points ($\leq$ 1729) indicated that a 308 point mesh was sufficient. In evaluating equation (1) the following steps were taken. At a given $\vec{k}$ point all initial ($E_i(\vec{k})$) and final ($E_f(\vec{k})$) energies were calculated. The energy conserving δ-function in equation (1) was treated by demanding that $E_f(\vec{k}) - E_i(\vec{k}) - \hbar\omega < W$. We chose $W = 0.01\, E_f(\vec{k})$ but it was found that the calculated PED's were insensitive to the actual value of W. A similar observation was made by Janak, et al.[26] who found their calculations to be insensitive to broadening of the electron states. For each pair of initial and final state energies that satisfied the energy conserving δ-function in equation (1) a transition matrix element $|t_{fi}|^2$ was calculated. The product

$|t_{fj}|^2 D_f(\vec{k})$ was taken as a weight factor for the density of states calculation. k-integration was performed using the Gilat-Raupenheimer method.[27] The PED's were then convoluted with a 0.5 eV FWHM Gaussian to account for experimental resolution and lifetime broadening of the hole state.

ACKNOWLEDGEMENTS

We would like to thank R. Z. Bachrach and the Xerox group, Palo Alto, for the use of their experimental apparatus and for experimental help during the initial phase of the project.

Helpful discussions with R. S. Williams are gratefully acknowledged.

REFERENCES

1. For a recent review see D. E. Eastman in Proc. IV International Conference on Vacuum Ultraviolet Radiation Physics, Hamburg, July 1974, ed. E. Koch, R. Haensel, and C. Kunz (Pergamon, Vieweg 1974).

2. This is most easily seen for the case of free electron final states where the number of final states increases as the square root of photon energy.

3. For a recent review see C. R. Brundle, Surface Science 48, 99 (1975).

4. P. J. Feibelman and D. E. Eastman, Phys. Rev. B10, 4932 (1974).

5. F. C. Brown, R. Z. Bachrach, S. B. M. Hagström, N. Lien, and C. H. Pruett in reference 1, p. 785.

6. P. W. Palmberg, J. Electron Spectrosc. 5, 691 (1974).

7. a) C. S. Fadley and D. A. Shirley, Electronic Density of States, Nat. Bur. Stds. Special Publication 323, 163 (1971).

   b) I. Lindau and L. Wilson, Phys. Lett. 42A, 279 (1972).

   c) G. K. Wertheim, D. N. E. Buchanan, N. V. Smith, and M. M. Traum, Phys. Lett. 49A, 191 (1974).

8. The various significant contributions which lead to this semiclassical model are listed in reference 4.

9. We are aware of only one band structure calculation which extends to ∿150 eV above the Fermi level, namely, V. Hoffstein and D. S. Boudreaux, Phys. Rev. B2, 3013 (1970), who calculated energy bands for Aℓ using a pseudopotential method.

10. See for example L. Pincherle, Electronic Energy Bands in Solids, (MacDonald, London, 1971), pp. 104 - 108.

11. N. V. Smith, Phys. Rev. B3, 1862 (1971).

12. L. Hodges, H. Ehrenreich, and N. D. Lang, Phys. Rev. 152, 505 (1966); H. Ehrenreich and L. Hodges in Methods in Computational Physics, edited by B. Alder, S. Fernbach, and M. Rotenberg (Academic, New York, 1968), Vol. 8, p. 149.

13. J. W. Gadzuk, Phys. Rev. B10, 5030 (1974).

14. E. Clementi and C. Roetti, Atomic Data and Nuclear Data Tables 14, 177 (1974).

15. We assume that our sample did not show any preferential crystalline orientation. For a true-polycrystalline sample the polarization of the incoming synchrotron light averages out with respect to the various crystalline orientations.

16. These emission directions lead to the "primary cones" in Mahan's terminology (G. D. Mahan, Phys. Rev. B2, 4334 (1970)).

17. For wave functions with a radial node, so called Cooper-Minima (J. W. Cooper, Phys. Rev. Lett. 13, 762 (1964)) may arise and the transition strength may vary strongly with energy. Effects of this kind have been observed by us for the 4d valence band in Ag metal. These results will be published separately.

18. V. V. Nemoshkalenko, B. G. Aleshin, Yu. N. Kucherenko, and L. M. Sheludchenko, Solid State Comm. 15, 1745 (1974).

19. F. R. McFeely, J. Stohr, G. Apai, P. S. Wehner, and D. A. Shirley, to be published.

20. W. D. Grobman, D. E. Eastman, and J. L. Freeouf, Phys. Rev. B12, 4405 (1975).

21. B. Feuerbacher and R. F. Willis, J. Phys. C9, 169 (1976).

22. Recently I. Lindau, P. Pianetta, K. Y. Yu, and W. E. Spicer, Phys. Rev. B13, 492 (1976), reported photoemission results on polycrystalline Au. In this case cross section effects due to the radial nodes of the 5d wave function may be present. Similar cross section effects have also been observed by us for the case of Ag(4d).

23. A. Liebsch, Phys. Rev. B13, 544 (1976).

24. P. M. Morse and H. Feshbach, Methods of Theoretical Physics, McGraw-Hill, New York (1953), p. 1573.

25. E. Kane, Phys. Rev. 159, 624 (1967).

26. J. F. Janak, A. R. Williams, and V. L. Moruzzi, Phys. Rev. B11, 1522 (1975).

27. G. Gilat and L. J. Raupenheimer, Phys. Rev. 144, 390 (1966).

Table I. Momentum Matrix Elements Between d and p Orbitals.

$\langle d_1 \mid L_x \mid P_2 \rangle = 1/\sqrt{5}$	$\langle d_1 \mid L_y \mid P_1 \rangle = 1/\sqrt{5}$	$\langle d_2 \mid L_z \mid P_2 \rangle = 1/\sqrt{5}$
$\langle d_3 \mid L_x \mid P_3 \rangle = 1/\sqrt{5}$	$\langle d_2 \mid L_y \mid P_3 \rangle = 1/\sqrt{5}$	$\langle d_3 \mid L_z \mid P_1 \rangle = 1/\sqrt{5}$
$\langle d_4 \mid L_x \mid P_1 \rangle = 1/\sqrt{5}$	$\langle d_4 \mid L_y \mid P_2 \rangle = -1/\sqrt{5}$	$\langle d_5 \mid L_z \mid P_3 \rangle = 2/\sqrt{15}$
$\langle d_5 \mid L_x \mid P_1 \rangle = -1/\sqrt{15}$	$\langle d_5 \mid L_y \mid P_2 \rangle = -1/\sqrt{15}$	

FIGURE CAPTIONS

Fig. 1. Photoemission spectra of the 3d valence band of Cu for a series of photon energies. The data have been corrected for the decay in photon flux from the synchrotron but no background substraction or deconvolution has been carried out.

Fig. 2. a) X-ray photoemission spectrum (Aℓ K_α radiation) of the Cu valence band recorded on an Hewlett-Packard spectrometer.

b) The Cu 3d density of states (equation (5)), using Smith's[11] parameters. The dashed curve represents the original density of states. The solid curve is a convolution with a FWHM = 0.5 eV Gaussian.

Fig. 3. a) PED calculated for Cu 3d assuming k-conservation (direct transitions).

b) Experimental results for Cu. The original data shown in Fig. 1 have been corrected for their inelastic background.

c) PED calculation for Cu assuming k-broadening in the final state. The broadening factor B discussed in the text.

Fig. 4. Square of the radial dipole matrix element $\overline{|t_{fj}|^2}$ for Cu 3d as a function of the kinetic energy of the photoelectron. PW means plane wave, OPW means orthogonalized plane wave final state.

Fig. 5. Calculated PED for Cu 3d at hν = 50 eV and 90 eV according to equation (1). The solid lines were calculated with the matrix elements given by equation (4). The dashed lines were calculated with an angle integrated (or essentially constant) matrix element given by equation (A17).

a) PED's convoluted with a FWHM = 0.5 eV Gaussian.

b) Unconvoluted PED's.

Fig. 6. Calculated PED for Cu 3d at $h\nu$ = 50 eV as a function of momentum broadening in the final state (B).

a) PED's convoluted with a FWHM = 0.5 eV Gaussian.

b) Unconvoluted PED's.

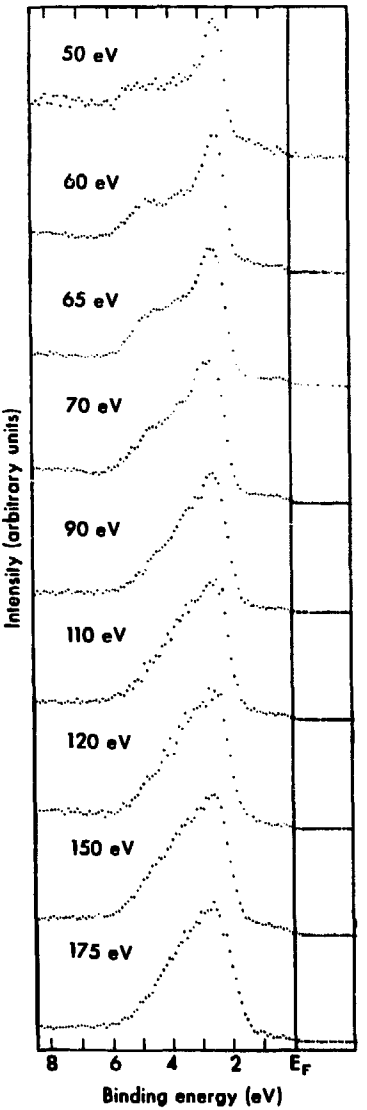

XBL761-2005

Fig. 1

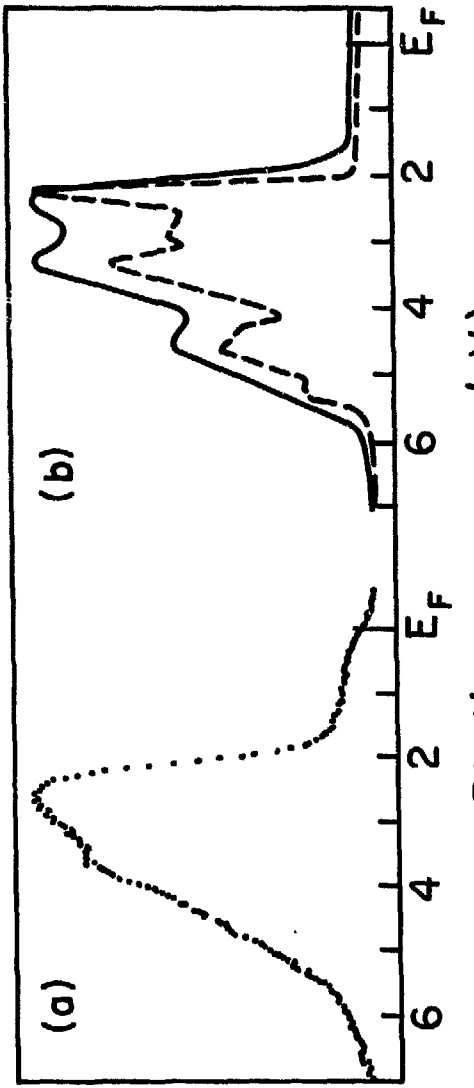

XBL761-2107

Fig. 2

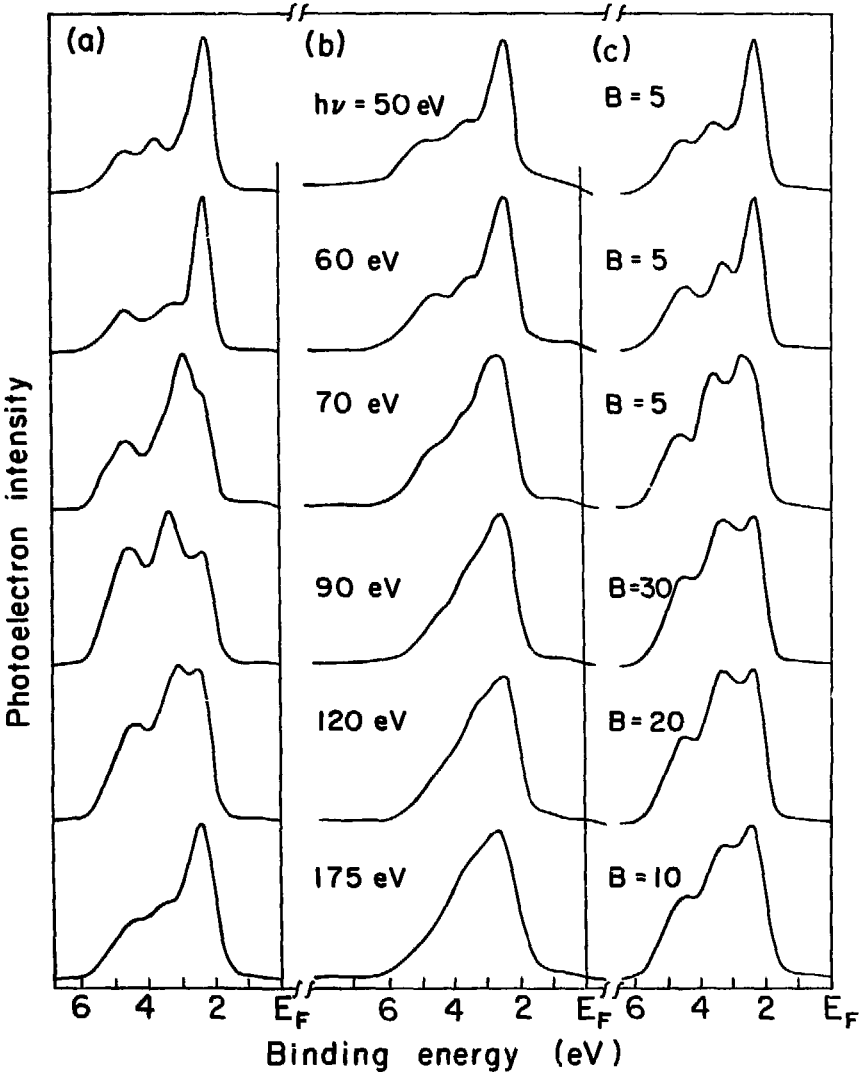
(a)
(b)
(c)
hν = 50 eV
60 eV
70 eV
90 eV
120 eV
175 eV
B = 5
B = 5
B = 5
B=30
B = 20
B = 10
Photoelectron intensity
6 4 2 E_F
6 4 2 E_F
6 4 2 E_F
Binding energy (eV)
XBL 761-2110

Fig. 3

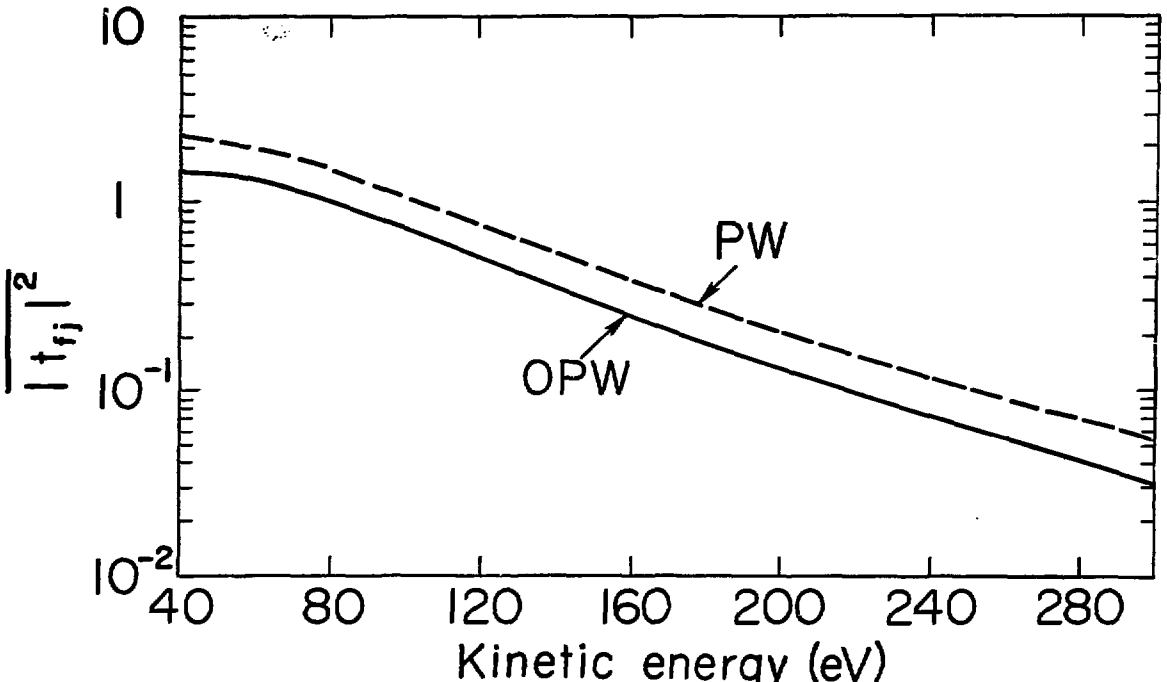

Fig. 4

XBL761-2113

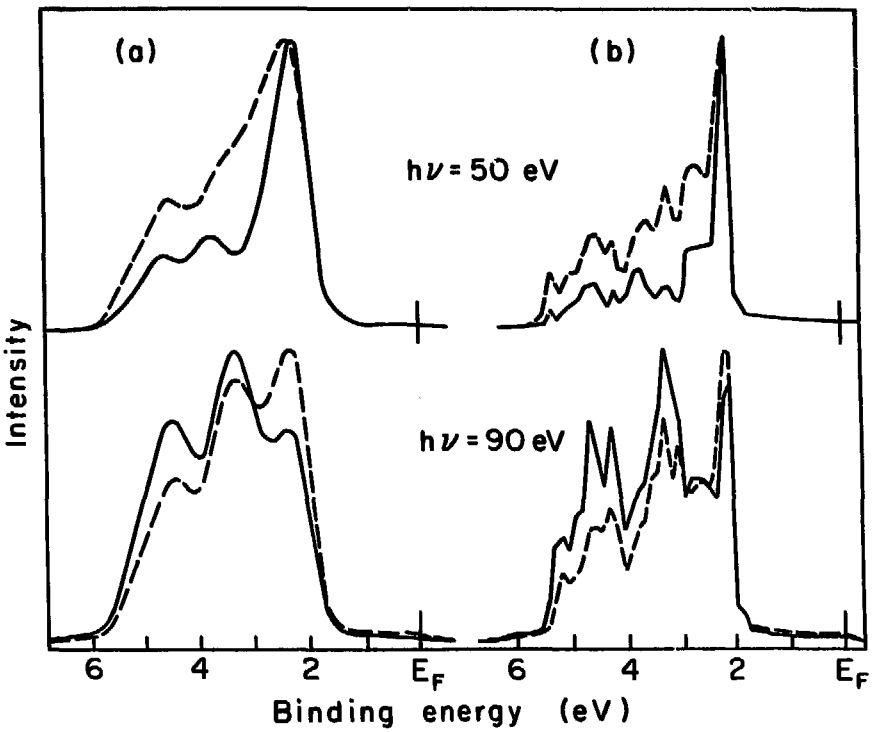

Fig. 5

XBL761-2108

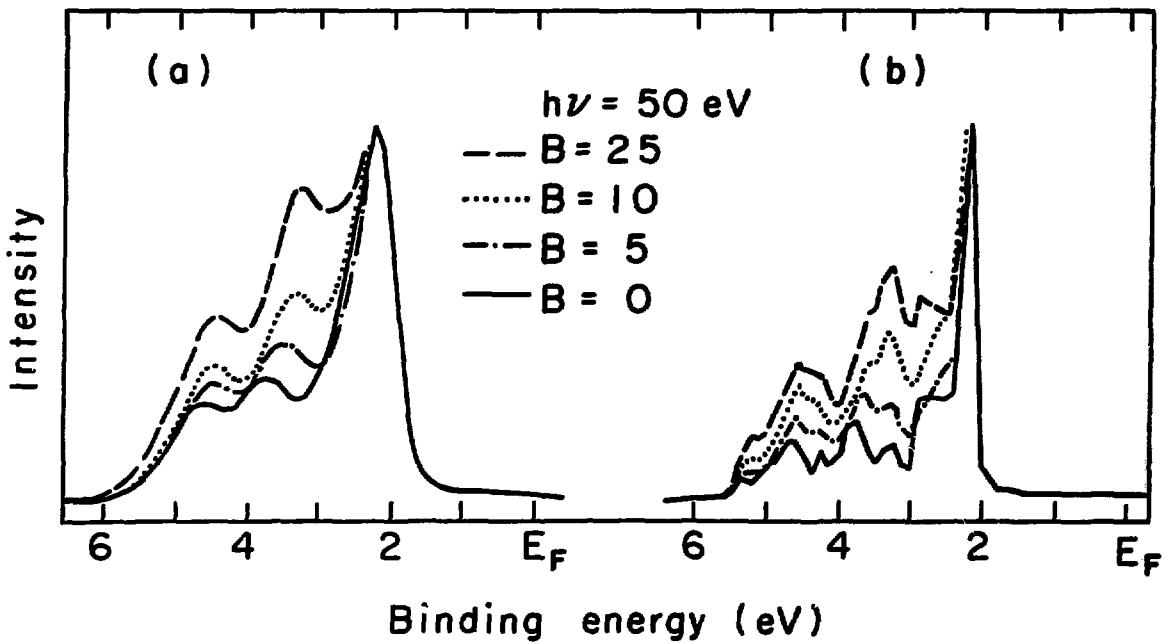

Fig. 6

XBL761-2109

V. CRYSTAL-FIELD EFFECTS ON THE APPARENT SPIN-ORBIT SPLITTING OF CORE AND VALENCE LEVELS OBSERVED BY X-RAY PHOTOEMISSION*

Abstract

Several anomalous relativistic effects in XPS spectra of metals and binary compounds are reviewed and explained in terms of combined spin-orbit and crystal-field interactions. The apparent spin-orbit splitting does not appear to be enhanced by renormalization effects, which would affect the expectation value of $\xi\vec{\ell}\cdot\vec{s}$ itself. The variation of $\xi\vec{\ell}\cdot\vec{s}$ with charge state is not large enough to be important in solids. Rather for both outer p and d shells, the splitting appears to be affected by "crystal-field" terms that carry the lattice symmetry. In III-V and II-VI compounds only the tellurium 4d shell may have a spin-orbit splitting different from the expected from free-atom data. However the enhancement is small (3%) and consistent with a tetrahedral crystal field. The enhancement of d-shell spin-orbit splitting in Zn and Cd arises from the Y_2 terms in the crystal field because of the large c/a ratio in these lattices. There is no enhancement for Cd in a cubic lattice, while the enhancement in several lattices follows the quadrupole coupling constant of ^{111}Cd, which presumably also arises from Y_2-symmetry terms. Finally the d-band density of states in fcc Au and Ag is consistent with a $\xi\vec{\ell}\cdot\vec{s}$ and a Y_4 interaction. The absence of enhancement splitting in valence-shell p shells in Pb and Bi is explained

*Work performed in collaboration L. Ley, S. P. Kowalczyk, and D. A. Shirley (Phys. Rev. B10, 4481 (1974)).

in terms of the lower symmetry of the p-wave functions as compared to those of the d-electrons and the only partial filling of p derived valence bands in these metals.

A. Introduction

A feature readily observed in x-ray photoelectron spectroscopy (XPS) of heavier elements is a splitting of core levels, commonly referred to as spin-orbit (s-o) splitting. This splitting reflects the two possible couplings of the core hole spin $\vec{s}$ with its angular momentum $\vec{\ell}$ forming total angular momentum eigenstates differing in energy by the differences in the expectation value $(\vec{\ell}\cdot\vec{s})$ multiplied by a factor ξ, the coupling strength.

Within the accuracy obtainable in earlier XPS work these splittings appeared to be equal in solids and gases and agreed as well as could be expected with the s-o splitting obtained from optical data[1] and relativistic Hartree-Fock calculations.[2] Improvement in the resolution obtained in XPS and the availability of UV sources in an energy range that gave access to the least-bound core levels improved the accuracy with which these splittings could be measured to an extent that made it possible to measure small deviations of the spin-orbit splitting in solids from those measured in the gas phase. Furthermore even changes in the splitting of the outermost d-levels in Zn and Cd have been observed in going from the metal to binary compounds containing one of these elements.[3,4]

In this chapter we discuss some of the effects responsible for the observed splittings and their changes. In Section B we review the experimental data that will be discussed. In Section C we present the results of a simple model calculation that explains some of the puzzling experimental findings in terms of the influence of crystal fields of low symmetry on the energies of final states.

B. The Experimental Evidence for Spin-Orbit Like Splittings in Elements and Compounds

We shall consider only electronic excitations extending to about 50 eV above the ground state. This allows us to compare data obtained from two or more of: optical spectroscopy, UV photoemission, and XPS. The resolution of photoemission spectroscopy then further restricts our study to levels split by a least ~0.4 eV; i.e., to the outermost d-levels of the group II to VII elements and the p-levels of some of the heavier elements in the sixth row of the periodic system. The available data on these levels are set out in Table I. The elements listed in Table I have d-levels bound by at least 10 eV. These levels do not exhibit measureable band effects and are therefore referred to as core-like. In addition, the splitting of the outer d-levels in Ag and Au and the p-levels in Pb and Bi are listed in Table II. Although the atomic d-levels are broadened into bands in these solids, the determination of an average splitting of the two broad peaks is still possible. The same observation holds for the p-like bands in lead and bismuth.

It is convenient to compare the splittings observed in solids to those for the free ions as a secure starting point for the discussion of various solid-state effects. To do this, we have extracted the free-ion spin-orbit splitting from the observed term values of the configuration $(d^9)^2D$ in the optical spectra of the ions.[1] While rendering the determination of the spin-orbit splitting straightforward and reliable, this method has the disadvantage that we have to deal in some cases with very highly ionized atoms. To assess the importance

of this effect, we show in Table III the effect of the ionic charge on the spin-orbit splitting of the d-electrons in Cu, Zn, Ag, and Cd. The values for the spin-orbit splitting are taken from Dunn's compilation.[5] This table makes two points clear: (i) for a given d-shell configuration, the spin-orbit splitting increases with increasing ionic charge by not more than 2% per unit charge; (ii) a change in the d-configuration ($d^9 \rightarrow d^8$) affects the spin-orbit splitting considerably more than the corresponding increase in ionic charge.

These two points are consequences of the approximate form of the spin-orbit Hamiltonian-operator:

$$\mathcal{H}_{s.o.} = \frac{\alpha^2}{2}\left(\frac{1}{r}\frac{\partial V}{\partial r}\right) \vec{L}\vec{S} \quad ,$$

neglecting exchange effects and the mutual spin-orbit and spin-orbit interaction of electrons in unfilled shells.[6] Here α in the fine-structure constant and V is the shielded nuclear potential. The dependence of the expectation value $\langle \mathcal{H}_{s.o.} \rangle_\psi$ mainly on the inner part of the electronic wavefunction ψ has been pointed out by many authors. The variation in the operator $\frac{1}{r}\frac{\partial V}{\partial r}$ upon charge transfer in outer shells is very small in this region.

From these considerations it is clear that the atoms chosen in Table III are very favorable examples because the charge radii for nd and (n + 1)s electrons are not too different. Progressing in the Periodic Table would improve that difference but the high degrees of ionization quoted in Table I for, e.g., Sb and Te makes the quoted free-atom values of the spin-orbit splitting upper limits by a margin of an estimated (3 ± 3)%.

Returning to the data obtained from solids in Table I, we can make the following observations. The apparent $\Delta E_{s.o.}$ of the 4d level in metallic Zn and Cd exceeds $\Delta E_{s.o.}$ in the atoms by 59% and 45%, respectively. This increase is unique among the entries of Table I. The apparent $\Delta E_{s.o.}$ of Cd in tetrahedrally-coordinated binary compounds agrees within experimental error with the free-atom value. Combining the results of all three compounds, the apparent $\Delta E_{s.o.}$ lies 0.08 eV above the free atom $\Delta E_{s.o.}$. The weighted mean value for the apparent $\Delta E_{s.o.}$ in In metal lies at 0.89 eV, or 4.7% above the free-atom value of 0.85 eV. The values for In in tetrahedral coordination agree well with the free-atom $\Delta E_{s.o.}$.

The Sb apparent $\Delta E_{s.o.}$ values agree within the error limits with the free ion value, for both compounds and the metal. The 4d splitting for InSb measured by Cardona et al.[7] seems to be low, as does their value for the Te 4d splitting in PbTe. With this one exception the Te 4d values are higher than the free-atom spin-orbit splitting by about 2.8% for the compounds and 7% for the metal.

The entries for Hg show no anomalous behavior, nor do those for Pb in various surroundings. The observed splittings in the valence d-bands of Ag and Au (Table II) are considerably larger than the free-atom $\Delta E_{s.o.}$. The p-bands of Bi and Pb, however, do not exhibit such an increase, as has been observed earlier.[8] We can summarize this section as follows:

(i) Core-like d-levels of elements in tetrahedral surroundings show no, or only a very small ($> 1\%$), increase in the apparent $\Delta E_{s.o.}$ compared to free-atom values. The only exceptions are the Te compounds

with an average increase of ∿2.8%.

(ii) In, Te, Cd, and Zn metals have an apparent $\Delta E_{s.o.}$ in the outermost d-levels which exceed the free atom values by 4.7, 7, 45, 59% respectively.

(iii) Pb and Sb show no such increase.

(iv) Valence d-bands in Ag and Au are split by amounts far exceeding the free-atom $\Delta E_{s.o.}$ value, in contrast to the valence p-bands (Bi, Pb) which are split by energies close to $\Delta E_{s.o.}$ for the free atoms.

In the next section, we will attempt to show that this behavior can be explained by the effects of crystal fields of different symmetries on atomic levels in the solid.

C. Discussion

In this section we will discuss the influences on the apparent spin-orbit splitting of "core-like" d-levels of an atom surrounded by other atoms in a solid. This applies to the case of Cd and other elements which do not show appreciable band-structure broadening of the d-levels, in contrast to, e.g., Au, where the width of the two components is comparable or even greater than the total splitting. We will refer to the latter as "band-like" levels.

This distinction implies that in the former category energy dispersion with wave vector $\vec{k}$ may be neglected. That is, we treat those levels as if the energy ordering at $\vec{k} = \vec{0}$ is retained throughout the Brillouin zone. The justification for this approach is derived directly from experimental evidence (i.e., line widths) rather than from assumptions about overlap-integrals and potentials: it therefore possesses a high degree of validity.

We note at the outset that we are dealing with final-state structure following photoemission from a closed shell. This is manifestly a one-electron (hole) problem. The appropriate d hole state Hamiltonian in the one-electron approximation has the form

$$\mathcal{H} = h_0 + h_{cryst} + h_{s.o.} \quad . \tag{1}$$

Here h_0 contains the kinetic energy operator and the spherical Coulomb potential of the nuclear charge[7] screened by the inner electrons forming closed shells. The h_{cryst} term summarizes the potentials due to the neighboring atomic cores and the valence electrons including the valence electrons of the atom under consideration, and $h_{s.o.}$ is the one-electron spin-orbit hamiltonian.

We wish to show that the differences in the value for the d-level splittings, $\Delta E_{s.o.}$ observed in different solid environments is a result of the influence of h_{cryst} rather than of a modification in $h_{s.o.}$. To do so, let us first consider $h_{s.o.}$ in more detail. The spin-orbit interaction is a first order effect in the expansion of the relativistic energy expression for a spinning electron in an electric field U.[9] The reduction to a non-relativistic form[10] gives the result (in atomic units):

$$h_{s.o.} = \xi \vec{\ell} \cdot \vec{s} = \frac{\alpha^2}{2} \left(\frac{1}{r}\frac{\partial U}{\partial r}\right)_{n\ell} \vec{\ell} \cdot \vec{s} \quad , \tag{2}$$

the expression already given in Section B. The brackets indicate the expectation value of $\frac{1}{r}\frac{\partial U}{\partial r}$ evaluated in the state $n\ell$. We can rewrite the Lande factor ξ as:

$$\xi_{n\ell} = \frac{\alpha^2}{2} \int_0^\infty \frac{(R_{n\ell})^2}{r} \frac{\partial U}{\partial r} \, dr \quad , \tag{3}$$

where $R_{n\ell}(r)$ is the normalized radial wavefunction of the electron in the state $n\ell$. A generalization of this result to a many electron system is not straightforward; we refer the reader to the article by Blume and Watson[6] for a detailed discussion of this problem. Their result can be stated as follows: $h_{s.o.}$ for electrons in an unfilled shell can be written as

$$h_{s.o.} = \frac{\alpha^2}{2} \left\langle \frac{1}{r} \frac{\partial U_{eff}}{\partial r} \right\rangle \quad \ell_i \cdot s_i$$

$$+ \text{ terms which include mutual spin-orbit interactions and spin-orbit interactions in the unfilled shell.} \tag{4}$$

The summation extends only over electrons in unfilled shells. Replacing U with U_{eff}, which is essentially a screened potential, including exhange, accounts for the mutual spin-orbit and spin-spin interaction between the open-shell and the closed-shell electrons. It has the effect of reducing the spin-orbit coupling constant.

With this operator in mind, let us now investigate the influence of different surroundings on $h_{s.o.}$ and thereby on the intrinsic spin-orbit splitting of outer d-electrons.

In Section B. we already showed, that the charge state of the ion has only a very small influence on $\langle h_{s.o.} \rangle$, even for changes of several units in $|e|$. Charge transfers of a fraction of the elementary charge that are to be expected in partially ionic solids therefore have a quite negligible effect on $\langle h_{s.o.} \rangle$.

So far we have dealt with the effects of charge transfer in the valence shell of the central atom on $\langle h_{s.o.} \rangle$. We must also consider direct changes in the wavefunction of the d-electrons itself upon entering a solid or molecule. These changes can be considered in two parts:

(i) Renormalization of ψ_d due to the necessary orthogonalization of ψ_d with respect to wavefunctions on neighboring atoms. In the simplest case of orthogonalization to one other orbital, this leads to a renormalization-factor of $(1 - S^2)^{-1/2}$, where S is the overlap integral between the two orbitals. The extension to more than two orbitals has been given by Löwdin.[11] This leads to an increase in the coefficient of ψ_d and therefore in the Lande factor ξ_d. The components added to the wavefunction upon orthogonalization make only vanishing contributions for small r, the region which determines ξ_d.

(ii) A mixing of the d-electrons with electrons of different symmetry located at the same atom. This mixing is always possible throughout the Brillouin zone but at $\vec{k} = 0$ it is possible only for certain symmetry components of the potential. This effect leads to a decrease in the spin-orbit splitting, because the orbital that will mix most strongly to the nd wavefunction is (n+1)p, with a Lande factor smaller than that of the d orbital. We can therefore dispense with the second effect in explaining increases in the apparent $\Delta E_{s.o.}$.

The renormalization discussed under (i) increases $\langle h_{s.o.} \rangle$ but the increase is overlap-dependent. Overlap also determines the extent to which an atomic level is broadened into a band. This excludes renormalization as a decisive factor in the increase of $\langle h_{s.o.} \rangle$ for core-like levels.

Renormalization might be thought to play a major role in the enhanced d-band splitting of silver and gold, to which these arguments do not apply, were it not for the absence of noticeable increases in the apparent $\Delta E_{s.o.}$ in the p bands of Pb and Bi, which would fall into the same category.

In summary, direct changes in the expectation value of $h_{s.o.}$ can not be responsible for the observed increases in the apparent $\Delta E_{s.o.}$ over their free-atom values. The explanation must therefore be sought in the h_{cryst} term if we are to explain the enhancement within the framework of the Hamiltonian in Eq. (1).

The matrix element of h_{cryst} can be expanded into a series of spherical harmonics $Y_{LM}(\Theta,\phi)$. The angular momentum $\vec{\ell}$ of the state under consideration limits this expansion to a sum over even orders in L. For d electrons the last nonvanishing term has $L_{max} = 4$, while for p-electrons $L_{max} = 2$. The matrix element $\langle h_{cryst} \rangle_i$ has the symmetry of the point group of the lattice and is in general given by

$$\langle h_{cryst} \rangle_i = \sum_{L=0,2,4,} A_L T_L(i) \quad , \tag{5}$$

where $T_L(i)$ is the linear combination of spherical harmonics of order L that transforms as the symmetrical irreducible representation of the point group of the lattice at the center of the Brillouin zone. A_L is the expansion coefficient, which contains the radial integral of the Coulomb and exchange interaction of the electron i with the valence electrons and the surrounding ion cores.[12]

Instead of calculating the A_L we shall treat them as free parameters. It should, however, be noted the for a normal expansion of the type of Eq. (5) A_L decreases with increasing L. We shall ignore the term with L = 0 which corresponds to a generalized Madelung energy and cannot contribute to a splitting in the atomic levels. In solids which crystallize in lattices of cubic symmetry the A_2 T_2 term in expression (5) vanishes. This applies to the face centered cubic (fcc) lattices of Ag, Au, and Pb and to the tetrahedrally coordinated binary compounds. All other symmetries encountered in this investigation require the retention of the L = 2 term.

It is evident from the data in Table I that all cases which exhibit an increase in $\Delta E_{s.o.}$ for the core d-levels fall into this latter group with the possible exception of the tellurium salts. The nonvanishing A_2T_2 term in expansion (5) seems therefore a necessary condition for an increase in $\Delta E_{s.o.}$.

Let us explore this possibility in more detail using Zn and Cd as examples. Zn and Cd crystallize in a hexagonal lattice. In this case it is convenient to divide the L = 2 term into three factors:

$$\langle h_{cryst} \rangle_i = f(\tfrac{c}{a}) \cdot A_2^{hex} \cdot T_2^{hex} + A_4^{hex} T_4^{hex} \qquad (6)$$

The geometrical factor $f(\frac{c}{a})$ depends on the ratio of the crystalline axes c and a. For c/a = 1.63, the ideal hexagonal lattice, $f(\frac{c}{a})$ is zero and the A_2T_2 vanishes for geometrical reasons. In Zn and Cd however, c/a is equal to 1.86 and the L = 2 term enters with a considerable geometrical advantage ($f(\frac{c}{a}) > 1$ in the point-ion model). We have diagonalized the two operators $h_{s.o.} + h_{cryst}$ in the sub-space of the

d-electrons. The method employed for this calculation uses standard angular momentum algebra as outlined in Edmonds.[13] The d^9 configuration is treated in the usual way as a d^1 configuration accompanied by a sign change in the coefficients A_L and the spin-orbit coupling constant ξ.

Fig. 1a shows the level scheme for a d^9 configuration in the ideal hexagonal field ($f(\frac{c}{a}) - 0$) as a function of A_4. All degeneracies are lifted, yet the increase in the apparent spin-orbit splitting is negligible for values of A_4 which preserve the observed pattern of two d-peaks, that is for $|A_4| < 0.4|\xi|$. Beyond this point the energy separation between individual levels becomes comparable to the experimental line width of each component line ($\sim$0.7 eV) and a spectrum would loose the character of a doublet.

Lifting the restriction of c/a = 1.63 introduces the A_2T_2 term, which changes the level pattern appreciably (Fig. 1b). As mentioned above, A_2 is expected to be greater than A_4 and we have therefore plotted the level scheme under the assumption that $A_4 = 0$. For positive values of A_2 the spin-orbit split doublet evolves into a pattern of two nondegenerate doublets and a single level, which would result in a three peak spectrum with relative intensities 1:2:2. For $A_2 < 0$ a drastic increase in apparent $\Delta E_{s.o.}$ is possible without destroying the general appearance of a spin-orbit split d-doublet with the correct intensity ratio of 2:3. The value of A_2 which gives the observed spin-orbit splitting in Zn and Cd is about $1.4|5/2\xi|$. A spectrum generated from the level scheme at this point does indeed resemble the observed Cd spectrum closely. The line-width was set to be $5/2\,\xi = 0.7$ eV and the increase in spin-orbit splitting as measured from the spectrum

appears to be 58%. The ratio of the amplitudes of the two components is reduced to 1.21 from the expected value 1.5 when equal line widths are assumed. This is in good agreement with the value 1.3 quoted in ref. 3. for the Cd 4d spectrum in Cd metal and lends further support to our interpretation.

The influence of a non-vanishing A_4 on the level scheme of Fig. 1b has been tested, and is found to be compatible with the above discussion as long as A_4 is negative and does not exceed ~30% of the absolute value of A_2.

This direct evidence that the increase in apparent $\Delta E_{s.o.}$ in Cd and Zn is symmetry-induced is supported by three pieces of additional experimental data.

(i) Fig. 2 shows the Cd 4d double and for a AgCd alloy (10% Cd). The substitutional introduction of the Cd atom into the cubic surrounding of the A_g lattice reduces $\Delta E_{s.o.}$ to the free atom value.

(ii) The photoemission spectrum of Cd deposited in submonolayer coverage onto a Au single crystal shows no increase in spin-orbit splitting of the 4d level (compare Fig. 2). We interpret that as the observation of single Cd atoms which are subjected to no crystal field. The existence of single Cd atoms in the presence of surface diffusion is favored by the exceptionally low dissociation energy of a Cd-cluster.[14] When the Cd coverage is increased to the extent, that the formation of Cd clusters becomes possible, the d-level splitting increases to the value in Cd metal.

(iii) Another physical property that is known to be proportional to the L = 2 term in an expansion similar to that of expression (5) is

the electric field gradient at the nucleus. This field gradient can be measured by observing the interaction of the nuclear quadrupole moment Q with the field gradient q. Values of the coupling constant eqQ/h for ^{111}Cd in host lattices of Pb, In, Zn, and Cd[15] are plotted against the increase in apparent $\Delta E_{s.o.}$ for these metals in Fig. 3. The plot shows a quite convincing correlation between the excess splitting and the quadrupole interaction of the few points available.

The only non cubic metal, that does not clearly exhibit the expected increase in $\Delta E_{s.o.}$ is Sb. The group V semimetals As, Sb, and Bi crystallize in the same rhombohedral structure which can be thought of as being composed of two interpenetrating, trigonally distorted fcc lattices.[16] The trigonal distortion decreases in this series with increasing atomic number. It appears that the distortion in Sb is already too small to result in a measurable increase in the splitting of the 4d-levels. This conclusion is corroborated by the results of the quadrupole interaction of ^{204}Pb in the series of As, Sb, and Bi host lattices.[15] The interaction strength eqQ/h decreases by factors of two from one lattice to the next. The $\Delta E_{s.o.}$ enhancement in In represents about the smallest value measurable by photoemission; therefore in Sb, where eqQ/h is reduced by a factor of 0.8 from its value in In, the enhancement should not be detectable.

We have used the analogy between the electric field gradient and the enhanced spin-orbit splitting as a diagnostic tool in the last few paragraphs. It should however be stressed, that this analogy extends only to the similarity in the geometrical conditions which make both effects possible. We cannot expect that the actual matrix elements

involved in the description of these quite different phenomena are equal. The nuclear quadrupole interaction deals with the field gradient at the nucleus of d-electrons in an ionized lattice atom with its surrounding.

Before we turn to the valence bands, let us consider the case of the tellurium salts. The level scheme for a d^9 configuration in a tetrahedral environment is shown in Fig. 4. as a function of A_4^{tet}. The degeneracy of the $d_{5/2}$ state is partially lifted into a singly degenerate state Γ_8 (excluding spin degeneracy). The degeneracy of $d_{3/2}$ (Γ_8) is preserved.

For $A_4 < 0$ the apparent splitting between the upper Γ_8 level and the lower $\Gamma_7 - \Gamma_8$ doublet could increase significantly over $5/2|\xi|$ without altering the overall appearance of the spectrum greatly provided that the natural width of the component lines is fairly large, as would be the case for the semi-conductors discussed here.

For $A_4 > 0$ no such increase in the apparent spin-orbit splitting would be observed for small A_4 ($A_4 < 1$) but rather the evolution of three separate lines which finally ($A_4 > 1.5$) resolve into two lines with a reversed intensity ratio of 3:2, in contrast to experimental observation.

The 3% increase in apparent $\Delta E_{s.o.}$ for the tellurides is therefore compatible with a negative A_4 of the order of $\sim 0.5|\xi|$, or ~ 0.75 eV. This is a magnitude entirely consistent with expectations for a Te ion surrounded tetrahedrally by four group II ions in the II-VI compounds or by 6 Pb ions in the NaCl structure of PbTe. The sign of A_4 is compatible only with primarily electronic contributions to the crystal

field Hamiltonian, however.

Because of the absence of any enhancement of $\Delta E_{s.o.}$ for the cations of these lattices and for the d-levels of all other binary compounds in Table I ($|\Lambda_4 < 0.2\ |\xi|$) we are reluctant to draw conclusions about possible enhancement of the apparent $E_{s.o.}$ in the tellurides.

Let us return now to the splittings observed in the valence d shells of Ag and Au and the p shells in Pb and Bi. These cases cannot be treated rigorously without taking the band character of these states into account. That is, level ordering at $\vec{k} = 0$ is not necessarily representative of the appearance of the density of states $\rho(E)$ as observed in an XPS-spectrum. The higher volume associated in reciprocal space with in the outer parts of the Brillouin zone (BZ) points makes these regions dominant in the determination of $\rho(E)$. It does seem clear that the renormalization effect mentioned earlier is not responsibel for the observed effects. It if were, we would expect comparable effects on d and p bands. This is not observed.

The elements Ag, Au, Pb, and approximately also Bi crystallize in the fcc structure; that is, the symmetries throughout the Brillouin zone are the same for all four elements. Nevertheless, the observed differences in the apparent $\Delta E_{s.o.}$ between d bands (increase) and p bands (no increase) is striking they can be understood in terms of the symmetry induced splittings at representative points of the Brillouin zone. The d-electrons of Ag and Au are already split into two groups of bands, Γ_{12} and Γ'_{15}, at Γ the center of the BZ which has the full octahedral symmetry. Towards the outer parts of the BZ, these bands split further accompanied by a rearrangement of levels according to the

various irreducible representations at symmetry points of lower than cubic symmetry. The maximum splitting occurs at X the center of the square face of the BZ. The pattern set by Γ and X can be regarded as representative for the two peaked structure in the density of states of Ag and Au. The spin-orbit interaction enhances this splitting further without being the dominant factor, however. The lower angular symmetry of the p-valence electrons in Pb and Bi preserves their orbital degeneracy at Γ. Along the symmetry directions on the surface of the BZ this degeneracy is partically lifted forming a singlet and a doublet level at each symmetry point except K.

The energy dispersion of these bands along the surface of the BZ is in general smaller than their splitting, giving rise to a two peaked density of states. In Pb and Bi, with 2 and 3 p-electrons respectively, only the bands in the lower peak of $\rho(E)$ are occupied, so that we would observe a single peak in the XPS-spectrum in the absence of spin-orbit interaction. In the presence of spin-orbit interaction, however, the two fold degenerate level at W splits and an inspection of the relativistic band structure of Pb by Loucks[17] reveals, that this splitting is preserved over much of the surface of the BZ giving rise to the observed doublet in the occupied part of $\rho(E)$. In the tight binding approximation, and in the absence of s-p hybridyzation the splitting at W equals the atomic splitting, a result that is in good agreement with experiment.

ACKNOWLEDGEMENT

We would like to acknowledge the assistance of D. Weissman in preparing the AgCd alloy.

REFERENCES

1. C. E. Moore, Atomic Energy Levels (U.S. Department of Commerce, NBS Circular No. 467 (1958).

2. T. A. Carlson, C. C. Lu, T. C. Tucker, C. W. Nestor, and F. B. Malik, Oak Ridge National Laboratory Report ORNL-4614 (1970).

3. R. A. Pollak, S. P. Kowalczyk, L. Ley, and D. A. Shirley, Phys. Rev. Letters 29, 274 (1972).

4. L. Ley, R. A. Pollak, F. R. McFeely, S. P. Kowalczyk, and D. A. Shirley, Phys. Rev. B9, 600 (1974).

5. T. M. Dunn, Trans. Faraday Soc. 17, 1441 (1961).

6. M. Blume and R. E. Watson, Proc. Roy. Soc. A270, 127 (1962).

7. M. Cardona, C. M. Penchina, N. Shevchik, and J. Tejeda, Sol. State Comm. 11, 1655 (1972).

8. L. Ley, R. A. Pollak, S. P. Kowalczyk, and D. A. Shirley, Phys. Letters 41A, 429 (1972).

9. P. A. M. Dirac, The Principles of Quantum Mechanics, (Oxford University Press, New York, 1947).

10. L. I. Shiff, Quantum Mechanics,(McGraw-Hill, New York, 1955).

11. P. O. Löwdin, J. Chem. Phys. 18, 365 (1950).

12. H. S. Jarrett, J. Chem. Phys. 31, 1579 (1959).

13. A. R. Edmonds, Angular Momentum in Quantum Mechanics, (Princeton University Press, Princeton, NJ (1957).

14. J. W. Geus, in Chemisorbtion and Reactions on Metallic Films, J. R. Anderson, editor (Academic Press, London 1971) p. 129.

15. H. Haas and D. A. Shirley, J. Chem. Phys. 58, 3339 (1973).

16. M. H. Cohen, L. R. Falikov, and S. Golin, IBM J. Develop. 8, 215 (1964).

17. T. L. Loucks, Phys. Rev. Letters 14, 1072 (1965).

Table I. Spin-orbit splittings in the free atoms and solids. Errors are given parenthetically. The roman numerals indicate the ionization state of the atoms (ZnII = Zn^+).

Element	Shell	Lattice	Splitting (eV)	Reference
Zn II	Zn3d	free ion	0.337	1
Zn metal	"	hex	0.54(2)	a
Cd II	Cd4d	hex	0.669	1
Cd metal	"	hex	0.95(3)	a
Cd metal	"	hex	0.99(5)	3
CdTe	"	z.b.[f]	0.70(5)	b
CdTe	"	z.b.	0.83(20)	c
CdS	"	z.b.	0.76(12)	c
CdSe	"	z.b.	0.87(16)	c
AgCd alloy	"	cubic	0.70(8)	this work
In III	In4d	free ion	0.849	1
In metal	"	tetragonal	0.90(1)	3
In metal	"	tetragonal	0.88(15)	b
In metal	"	tetragonal	0.86(3)	a
InSb	"	z.b.	0.83(3)	d
InSb	"	z.b.	0.85(5)	b
InSb	"	z.b.	0.84(8)	4
InP	"	z.b.	0.84(8)	4
Sb V	Sb4d	free ion	1.239	1
Sb metal	"	rhombohedral	1.25(4)	3
GaSb	"	z.b.	1.21(4)	4
InSb	"	z.b.	1.22(4)	4
InSb	"	z.b.	1.15(10)	d
InSb	"	z.b.	1.25(5)	b

(continued)

Table I. (continued)

Elements	Shell	Lattice	Splitting (eV)	Reference
Te VII	Te4d	free ion	1.409	1
Te metal	"	hex	1.51(1)	3
ZnTe	"	z.b.	1.47(2)	4
CdTe	"	z.b.	1.44(2)	4
HgTe	"	z.b.	1.44(2)	4
PbTe	"	NaCl	1.46(2)	4
PbTe	"	NaCl	1.35(10)	d
Hg I	Hg5d	free atom	1.800	1
Liquid Hg	"	-	1.83(9)	4
HgTe	"	z.b.	1.77(2)	4
HgTe	"	z.b.	1.91(10)	c
HgSe	"	z.b.	1.81(10)	c
HgS	"	z.b.	1.79(10)	c
Pb IV	Pb4d	free ion	2.643	1
Pb metal	"	f.c.c.	2.62(2)	8
Pb metal	"	f.c.c.	2.66(9)	a
PbS	"	NaCl	2.58(2)	e
PbSe	"	NaCl	2.61(2)	e
PbTe	"	NaCl	2.61(2)	e

[a] R. T. Poole, P. C. Kemeny, J. Liesegang, J. G. Jenkin, and R. C. G. Leckey, J. Phys. F., 3, L46 (1973).

[b] D. E. Eastman, W. D. Grobman and J. Freeouf (unpublished) D. E. Eastman, J. Freeouf and M. Erbudak, Congres du Centenaire de l' Societe Francaise de Physique, Vittel, France, (1973) unpublished.

[c] C. J. Veseley, R. L. Hengehold and D. W. Langer, Phys. Rev. B 5, 2296 (1972).

[d] M. Cardona, C. Penchina, N. Schevchik, and J. Tejeda, Solid State Commun. 11, 1655 (1972).

[e] F. R. McFeely, S. P. Kowalczyk, L. Ley, R. A. Pollak, and D. A. Shirley, Phys. Rev. B 7, 5228 (1973).

[f] z. b. = zincblende structure

Table II. Free atom spin-orbit splitting and the apparent splitting of valence-band peaks in Ag, Au, Pb and Bi.

Element	Shell	Lattice	Splitting (eV)	Reference
Ag I	4d	free atom	0.555	1.
Ag metal	"	f.c.c.	1.6(1)	3.
Au I	5d	free atom	1.522	1.
Au metal	"	f.c.c.	3.8(2)	a
Pb I	6p	free atom	1.746	1.
Pb metal	"	f.c.c.	1.80(5)	8.
Bi I	6p	free atom	2.163	b.
Bi metal	"	rhombohedral	2.16(8)	8.

[a] D. A. Shirley, Phys. Rev. B5, 4709 (1972).

[b] C. C. Lu, T. A. Carlson, F. B. Malik, T. C. Tucker and C. W. Nestor Jr., Atomic Data 3, Nr. 1 (1971).

Table III. Spin-orbit splitting of d-levels for various ionic charge states.

Element	Configuration	$\Delta E_{s.o.}$ (eV)	Reference
Cu I	$3d^9 4s^2$	0.253	1.
Cu II	$3d^9 4s$	0.257	5.
Cu III	$3d^9$	0.257	5.
Cu II	$3d^8 4s^2$	0.268	5.
Cu III	$3d^8 4s$	0.273	5.
Cu IV	$3d^8$	0.271	5.
Zn I	$3d^9 4s^2 p$	-	-
Zn II	$3d^9 4s^2$	0.337	5.
Zn III	$3d^9 4s$	0.281	5.
Zn IV	$3d^9$	0.341	5.
Ag I	$4d^9 5s^2$	0.555	5.
Ag II	$4d^9 5s$	0.567	5.
Ag III	$4d^9$	0.570	5.
Ag II	$4d^8 5s^2$	0.598	5.
Ag III	$4d^8 5s$	0.580	5.
Ag IV	$4d^8$	0.589	5.

FIGURE CAPTIONS

Fig. 1. Energies of a d^9 configuration as a function of the generalized crystal field parameter A_2.

(a) ideal hexagonal field: c/a = 1.63, $A_2 = 0$;

(b) general hexagonal field; A_4 is assumed to be zero. The insert shows a spectrum for $A_2 = 1.4\ |5/2\ \xi|$. The line width of each component is equal to ξ.

Fig. 2. The Cd 4d spectrum of (a) Cd metal, (b) a AgCd alloy (10% Cd), and (c) surface isolated Cd atoms.

Fig. 3. The excess in apparent spin-orbit splitting $\Delta E_{s.o.}$ versus the electrical quadrupole interaction strength eqQ/h of ^{111}Cd for a number of metals.

Fig. 4. Energies of a d^9 configuration in a crystal field of octahedral symmetry.

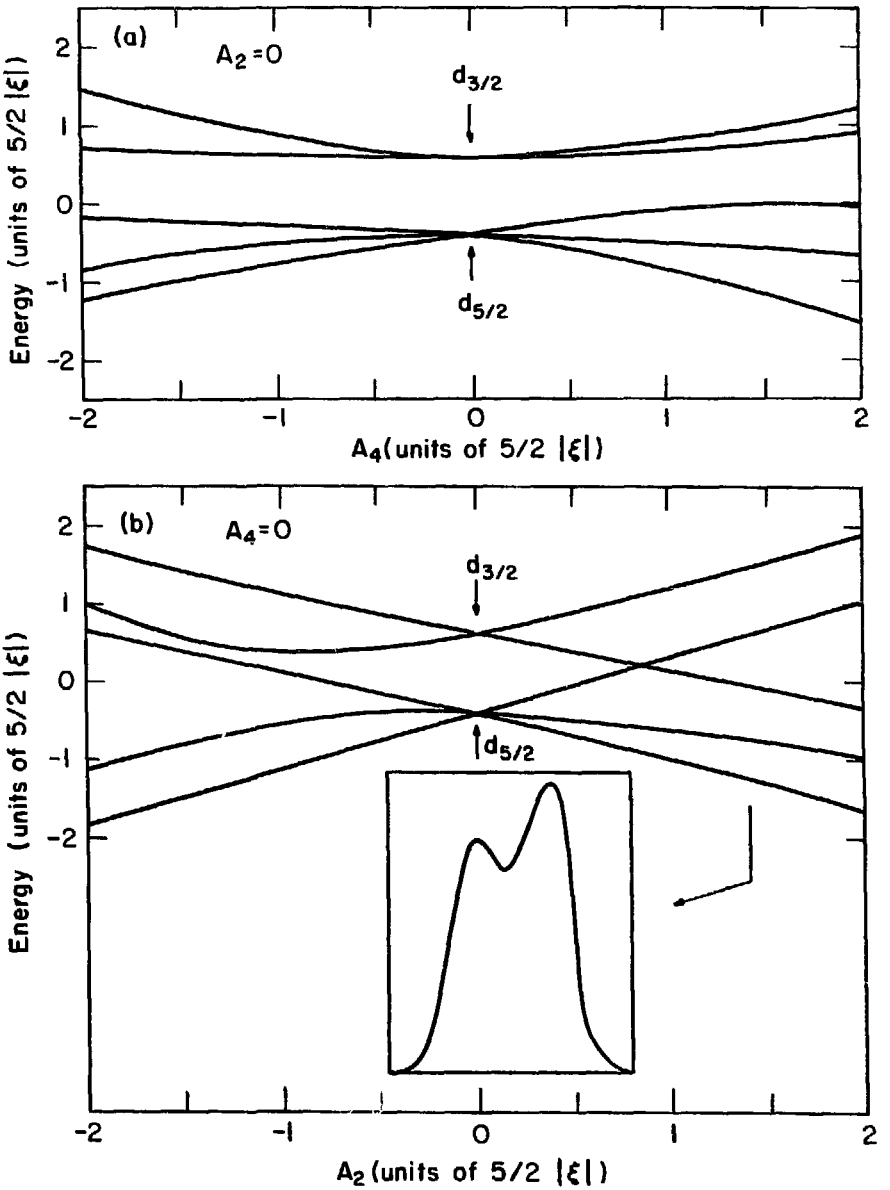

XBL 746-3462

Fig. 1

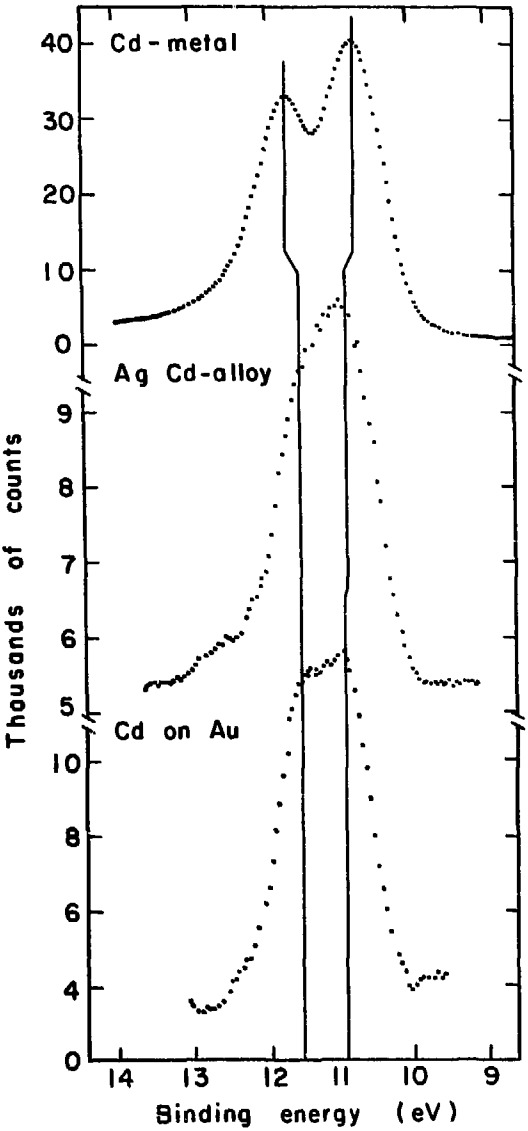

XBL744-2979

Fig. 2

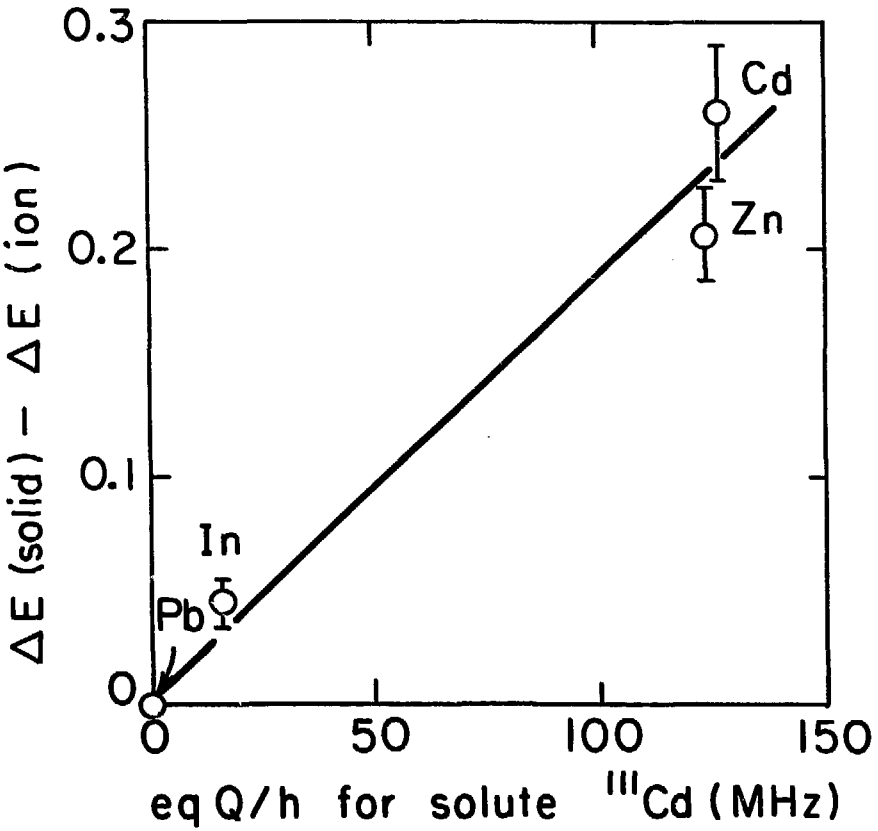

XBL744-2975

Fig. 3

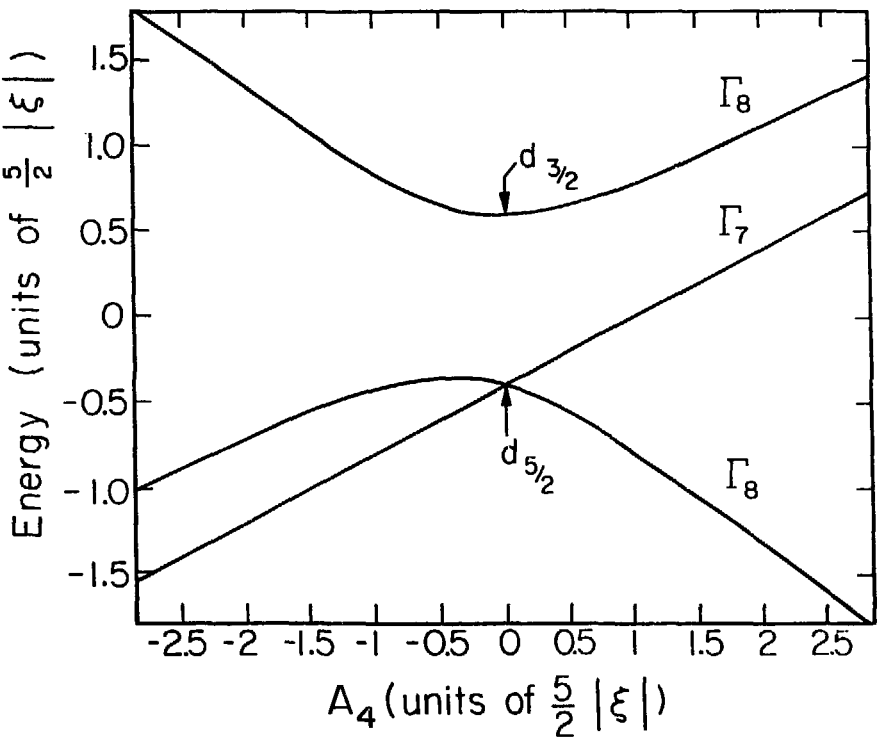

XBL735-2812

Fig. 4

VI. THE EFFECT OF SPIN-ORBIT SPLITTING ON THE VALENCE BAND DENSITY OF STATES OF LEAD*

Abstract

Tight-binding calculations are reported for the valence bands of lead, with and without spin-orbit splitting in the 6p bands. The addition of spin-orbit interaction is necessary to reproduce the two-peaked structure in the 6p density of states observed in x-ray photoemission, in contrast to the assertion by Breeze that crystal-field effects alone are enough. The observed splitting is, however, only fortuitously nearly equal to the atomic spin-orbit splitting. The tight-binding band structure, with spin-orbit splitting, gives better overall agreement with optical, Fermi surface, and photoemission data than did any of the three earlier band structures.

---

*Work performed in collaboration with S. P. Kowalczyk, L. Ley and D. A. Shirley (Solid State Comm. 17, 1415 (1975)).

A. Introduction

The electronic structure of metallic lead has been the subject of numerous experimental studies, mostly concerned with the elucidation of the Fermi surface. Naturally, the ultimate aim of these experiments is to provide the information necessary to construct a band structure which will explain the Fermi surface, optical spectra, photoemission spectra, and other electronic properties. Unfortunately, the difficulties involved in the calculation of a full relativistic band structure have apparently served to deter extensive first-principles calculations of the lead band structure and density of states. In an earlier paper, Ley et al.[1] reported a high-resolution x-ray photoemission (XPS) spectrum of the lead valence bands, and tentatively interpreted the two-peak structure at the top of the valence band as the result of spin-orbit splitting of the p bands. Recently, however, Breeze[2] has asserted, on the basis of a non-relativistic LCAO calculation, that the XPS splitting is instead simply the result of a crystal-field interaction. In this chapter we shall re-examine the origins of this feature of the XPS spectrum by means of parameterized LCAO calculations systematically including and excluding spin-orbit coupling. We shall show that the inclusion of spin-orbit effects is essential to a consistent understanding of the XPS, optical, and Fermi surface measurements.

B. The XPS Spectrum

Fig. 1 shows the XPS spectrum obtained by Ley et al.[1] using a Hewlett-Packard 5950A electron spectrometer which employed monochromatized Al K_α radiation (1486.6 eV). The high excitation energy and its

concomitant featureless density of final-states insures that the photoemission spectrum reflects the density of occupied valence band states, modulated by cross-section and final-state relaxation effects.[3] The photoemission cross-sections of the 6s and 6p atomic states of which the valence bands are composed should be essentially equal at this energy, and outer-shell relaxation effects are small.[4] Thus the features in the valence-band spectrum should be directly proportional to the density of states N(E).

We note again the important features in the spectrum; s-like and p-like bands split by ∿2.5 eV, a splitting of 1.8 eV in the p-like bands, and a total occupied p-bandwidth of ∿3.5 eV.

C. The Tight-Binding Calculations

The theory of tight-binding calculations, both as first-principles calculations[5] and as the basis of interpolation schemes,[6] has been discussed extensively. Basically it consists of using tight-binding Bloch functions of the form:

$$\phi_K^n(r) = N^{-1/2} \sum_{\ell} e^{iK\cdot\ell}\, U^n(r-\ell) \quad , \tag{1}$$

where $U^n(r-\ell)$ is an atomic function centered at site ℓ. There is, however, a problem connected with this approach. The $\phi_K^n(r)$ are not orthogonal, because the atomic functions $U^n(r-\ell)$ centered on different sites are non-orthogonal. This entails mathematical difficulties which can be avoided by orthogonalizing the $U^n(r-\ell)$ using a procedure due to Löwdin[7] which preserves the symmetry of the atomic function. Since we do not allow for non-orthogonality of basis functions in our Hamiltonian matrix, we tacitly assume that this has been done. As Slater and Koster[5]

have pointed out, however, the orthogonalization, by mixing functions on different sites, serves to increase the distance beyond which the matrix elements connecting different sites are negligible.

In these calculations a basis of one s- and three p-functions (p_x,p_y,p_z) for each spin were used. All nearest-neighbor interactions were included, and two second-nearest-neighbor interactions of the form s-s and p-p were treated. Mixing between s and p basis functions was treated only in nearest neighbors. The largest second-nearest-neighbor integral in the final parameterization was a factor of 6 smaller than the smallest nearest-neighbor term; thus the inclusion of third-nearest-neighbor interactions would have only a negligible effect. The neglect of 3-center terms was undoubtably of greater importance.

Since Breeze[2] calculated a density of states which matched the observed spectrum width reasonably well, we began by setting the spin-orbit coupling constant equal to zero and attempting to reproduce Breeze's band structure. We were able to match Breeze's energies exactly at the points Γ, X, W, and L in the Brillouin zone. At the point K, however, while we could fit the lowest p band and the s band quite easily, the splitting $K_4 - K_1$ in the upper two p-bands was 1.8 eV in our band structure as opposed to the value of ∿2.1 eV obtained by Breeze. The band structure thus obtained and the density of states calculated at 308 points in the irreducible 1/48th of the Brillouin zone are shown in Figs. 2 and 3. We shall hereafter refer to this calculation as the "zero spin-orbit splitting" case.

In dealing with the spin-orbit splitting, it is clear from the magnitude of the atomic spin-orbit coupling constant (ξ = 0.905 eV)[8]

that this term is too large to be treated by perturbation theory. Therefore the term $\xi_{6p}(r)\ \vec{\ell}\cdot\vec{s}$ was inserted into the Hamiltonian and the resulting matrix rediagonalized. We chose to use the atomic value for the spin-orbit coupling constant since this value must be at least approximately correct for the metal; $\frac{1}{r}\frac{\partial U}{\partial r}$ is dominated by the form of the atomic potential and cannot change drastically. While agreement with experimental data could be improved by adjusting $\xi(r)$, we feel that this is physically unwarranted, since beyond a certain point "better agreement" would merely reflect the improved cancellation with errors, such as the lact of 3-center terms, inherent in our approach. The band structure and density of states from this calculation are shown in Figs. 4 and 5. The only adjustment made to facilitate the agreement with experimental results was a $\sim$10% increase in the s-p off-diagonal matrix element.

D. Comparisons with Experiment

In this section we shall compare the two aforementioned band structures, the 4-OPW scheme of Anderson and Gold,[9] and the relativistic APW (RAPW) calculation of Loucks[10] with the available experimental data. We shall consider the XPS, Fermi surface, and optical results in succession.

The band structures of Loucks[10] and of Anderson and Gold[9] are both in serious disagreement with the XPS results. Their primary error is that they predict values of 4.5 eV and 4.0 eV respectively for the occupied p-bandwidth. This is somewhat in excess of the experimental value of $\sim$3.5 eV. Since both tight-binding calculations indicate that N(E) drops sharply to zero at the bottom of the p-bands, this experimental

value should be quite reliable. The OPW calculation has the further problem of giving almost no gap between the s- and p-bands while the experimental value is 2.5 eV. This splitting is, however, well matched by the RAPW calculation. Little more can be said about these band structures without actual N(E) calculations. The major conclusions are that they are somewhat too wide, and that the OPW calculation yields an anomalously small s-p band gap.

As can be seen from Figs. 2 and 3, the primary difference between the N(E) curves with and without spin-orbit splitting is the introduction of a square-shaped peak roughly 1 eV wide, centered around E_F. The origin of this peak becomes readily apparent upon comparison of the two respective band structures. In the zero spin-orbit case, there is a band crossing at 1.4 eV below E_F at the point W in the Brillouin zone. Since the slopes of the two bands near this point (W_3) are smoothly varying and non-zero everywhere in the vicinity of the crossing, there is no "peaking" of N(E) in this region. The highest energy W-point, W_2', is nearly degenerate (within $\sim$0.07 eV) with X_5', and the band connecting these two points is very flat; thus N(E) "peaks" in this region, giving rise to the sharp edge of the high-energy peak in N(E), as shown in the figure.

When the spin-orbit term is introduced into the Hamiltonian, the character of the bands in the region between X and W changes. The two-fold degenerate level X_5' is split into $X_6^-(X_5')$ and $X_6^+(X_1)$, separated by 0.75 eV, and the band crossing at W_3 is lifted with the introduction of a 1.1 eV gap between the two lowest p-bands at this point. It is this lifting of degeneracies that is responsible for the changes in N(E)

near the Fermi level. The primary change in this region is the appearance of a square-shaped peak for -0.2 to -1.2 eV. This peak arises almost totally from the middle p-band between X and W. The upper (0.2 eV) edge of this peak is due to the high-state-density region near $X_6^+(X_1)$, while the lower edge arises from the $W_6(W_3)$ region. In addition to this, the opening of the 1.1 eV gap between $W_6(W_3)$ and $W_7(W_3)$ has important consequences. As can be seen in comparing the N(E) curves with and without spin-orbit splitting, N(E) has a much lower minimum at -1.5 eV with spin-orbit splitting than without. The "missing" state density shifts to lower energy, raising the -3 eV peak in N(E) and giving it a square top.

The effects of these changes on the photoemission spectra were examined by truncating the N(E) curves at E_F and broadening them with a 0.6 eV FWHM Gaussian function in order to account for instrumental resolution. The results are seen in Fig. 6. It is evident that when instrumental resolution is considered the zero-spin-orbit N(E) gives only a peak and a shoulder, while the spin-orbit split N(E) yields two peaks.

In order to test our assignment of the p-band splitting in the photoemission spectrum, we systematically varied the parameters responsible for the p-band shape. This involved bascially 3 parameters, a p-p diagonal matrix element (e.g. $\langle p_y \mid H \mid p_x \rangle$) a p-p off-diagonal matrix element, (e.g. $\langle p_x \mid H \mid p_z \rangle$), and a matrix element mixing s- and p-functions, all between nearest neighbors. There was also a second nearest neighbor p-p diagonal matrix element in the calculations; however, it was a factor of seven smaller than the smallest of the

above and had a negligible affect on N(E). The observed spectrum allowed for surprisingly little variation in these parameters. The off-diagonal term determines the position of the lowest L-point and thus the total bandwidth. Its value is therefore fixed very accurately by the experiment. In addition the lowest X point must lie very near the absolute bottom of the bands, since, if it did not, an inflection point on the high-binding-energy wing of N(E) would be apparent, where in fact none is observed. This serves as a bound on the p-p diagonal matrix element, as it largely determines the position of this X point. The s-p mixing parameter is not essentially fixed by bandwidth considerations, and thus may be varied within reasonable limits without producing glaring inconsistencies. The most important effect of the variation of this parameter is that it alters the intensity of the two peaks in the spin-orbit split simulated spectrum. It had relatively little effect on the zero-spin-orbit spectrum, never producing anything more than a peak and shoulder structure. Our final choice for the value of this parameter represented a compromise between agreement with the photoemission spectrum and with the Fermi surface data discussed below.

Anderson and Gold[9] have given a very complete discussion of their de Haas-van Alphen effect measurements for lead. The band structure they calculate matches the extremal areas on the Fermi surface very well. It is therefore likely that this band structure is reasonably accurate in predicting the values taken by the wavevector $\vec{K}$ of the bands as they cross E_F. We have calculated some of these dimensions from our spin-orbit split band structure. These are shown in Table I compared with the analogous dimensions calculated by Anderson and Gold,[9] Loucks,[10]

and Breeze.[2] As can be seen, our calculations are quite comparable to the RAPW results. The one dimension, 3-11, where the discrepancy is serious is a region in which the band is nearly flat in crossing E_F, so that any slight adjustment of E_F could improve this value greatly without significantly affecting the other dimensions.

The optical properties of Pb have also been measured by Liljenvall et al.[11] by an ellipsometric technique. Table II indicates the position of several features in the spectrum with their tentative assignments. Our calculation and the RAPW calculation would appear to yield similar results. A Karmers-Kronig extropolation of these data, however, implies the existence of a peak at ~4.8 eV, which the authors suggest could be due to $X_6^-(X_4')$ - $X_6^+(X_1)$ transitions, on the basis of the RAPW band structure. If the band scheme proposed here is correct, these transitions would have to originate near the L-point. Higher energy optical data might help clarify this point. Mathewson et al.[12] generated an optical spectrum from Anderson and Gold's 4-OPW band structure[9] considering transitions throughout the Brillouin zone. As could be expected the results bore only qualitative similarity to the experimental spectrum.

E. Conclusions

This analysis of the Pb photoemission spectrum has shown the following:

1) The 2-peak structure in the spectrum is the direct result of spin-orbit splitting, through the lifting of degeneracies and introduction of gaps between bands and not due to the crystal field interaction,

2) The relative heights of the two peaks strongly reflects the degree of s-p mixing in the bands,

3) The observed splitting of 1.8 eV does not reflect any fundamental band splitting, but rather the placement of the Fermi level.

REFERENCES

1. L. Ley, R. A. Pollak, S. P. Kowalczyk, and D. A. Shirley, Phys. Letters 41A, 429 (1972).

2. A. Breeze, Solid State Comm. 14, 395 (1974).

3. J. Freeouf, M. Erdubak, and D. E. Eastman, Solid State Comm. 13, 771 (1973); L. Ley, R. A. Pollak, F. R. McFeely, S. P. Kowalczyk, and D. A. Shirley, Phys. Rev. B9, 600 (1974).

4. D. A. Shirley, Chem. Phys. Lett. 17, 312 (1972).

5. J. C. Slater and G. Koster, Phys. Rev. 94, 1498 (1954).

6. Henry Ehrenreich, and Laurent Hodges in Methods in Computational Physics, V. 8, pp. 89-92 (1968).

7. P. O. Löwdin, J. Chem. Phys. 18, 356 (1950).

8. C. E. Moore, Atomic Energy Levels, National Bureau of Standards circular 467 (1949).

9. J. R. Anderson and A. V. Gold, Phys. Rev. 139, A1459 (1965).

10. T. L. Loucks, Phys. Rev. Letters 14, 1072 (1965).

11. H. G. Liljenvall, A. G. Mathewson, and H. P. Myers, Phil. Mag. 22, 243 (1970).

12. A. G. Mathewson, H. P. Myers, and P. O. Nilsson, Phys. Stat. Sol. (b) 57, K31 (1973).

Table I. Comparison of Calculated Fermi Surface Dimensions. The Notation Follows Ref. 10. All Distances are in Atomic units.

	(LCAO) [a]	RAPW [b]	OPW [c]	This work [d]
3-4	.161	.158	.157	.162
5-6	.242	.259	.250	.244
7-9	.309	.338	.318	.322
8-9	.202	.184	.199	.193
10-11	.148	.146	.141	.167
12-13	.242	.239	.206	.251

a) Ref. 2
b) Ref. 10
c) Ref. 9
d) with ξ_{6p} = .905 eV

Table II. Comparison of the Prominent Optical Transitions with the Various Calculations. All Energies are in eV.

	This Work [a]	RAPW [b]	OPW [c]	LCAO [d]	Expt [e]
W_6-W_7'	1.3	1.1	1.2	1.8	1.1
Σ_3-Σ_1	∿1.5	∿1.7	∿1.4	∿1.1	1.5
W_7-W_7'	2.4	2.4	2.7	1.8	2.3
?					3.8
?					4.8

a) With ξ_{6p} = .905 eV
b) Ref. 10
c) Ref. 9
d) Ref. 2
e) Ref. 11

FIGURE CAPTIONS

Fig. 1. X-ray photoemission spectrum of the Pb valence band region from Ref. 1.

Fig. 2. Band structure of Pb without spin-orbit coupling.

Fig. 3. Band structure, density of states, and simulated XPS spectrum of Pb, without spin-orbit coupling.

Fig. 4. Band structure of Pb including spin-orbit coupling.

Fig. 5. Band structure, density of states, and simulated XPS spectrum of Pb, including spin-orbit coupling.

Fig. 6. a) XPS valence band spectrum

b) calculated spectrum with spin-orbit coupling

c) calculated spectrum without spin-orbit coupling.

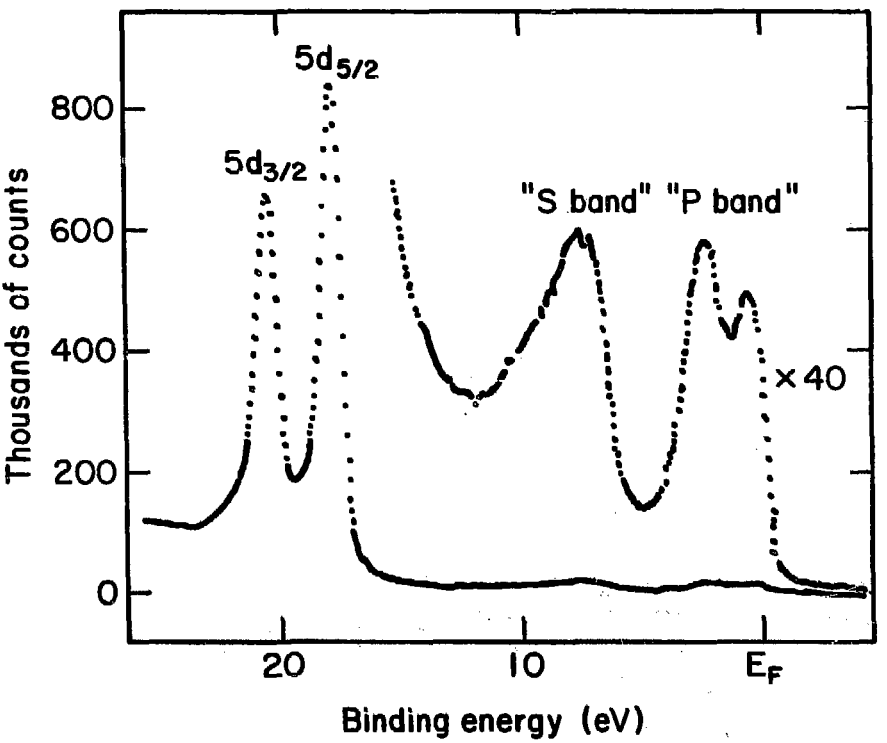

Fig. 1

XBL 752-2325

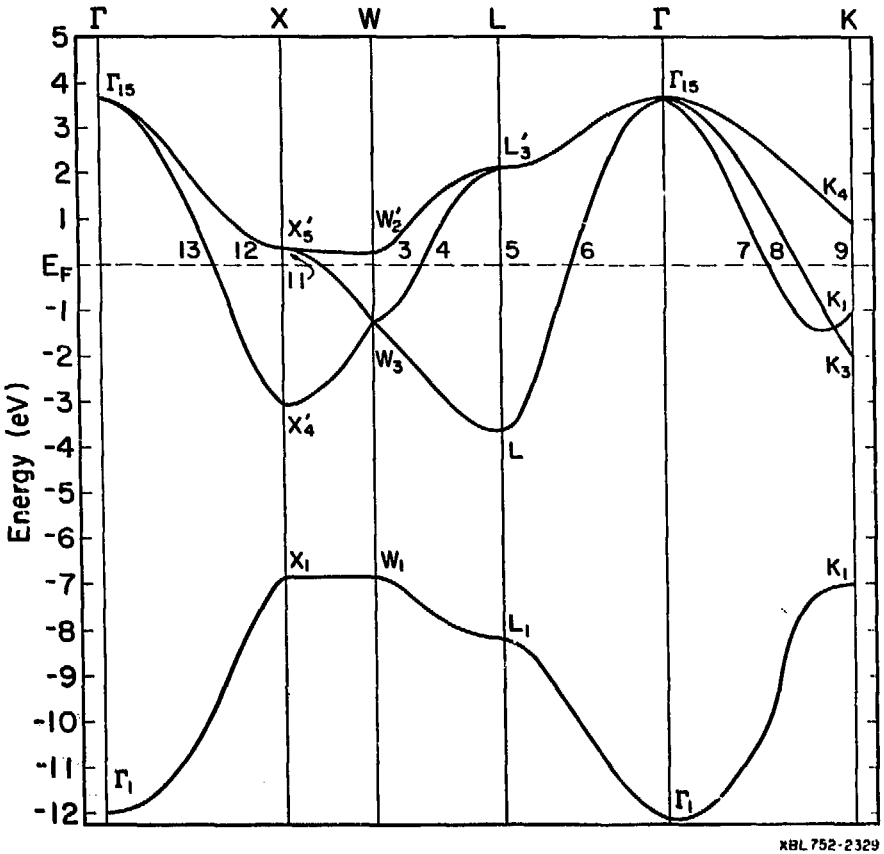
Γ
X
W
L
Γ
K
Energy (eV)
5
4
3
2
1
E_F
-1
-2
-3
-4
-5
-6
-7
-8
-9
-10
-11
-12
Γ15
X5'
W2'
L3'
K4
13
12
11
3
4
5
6
7
8
9
K1
W3
K3
X4'
L
X1
W1
K1
L1
Γ1
Γ1
XBL752-2329

Fig. 2

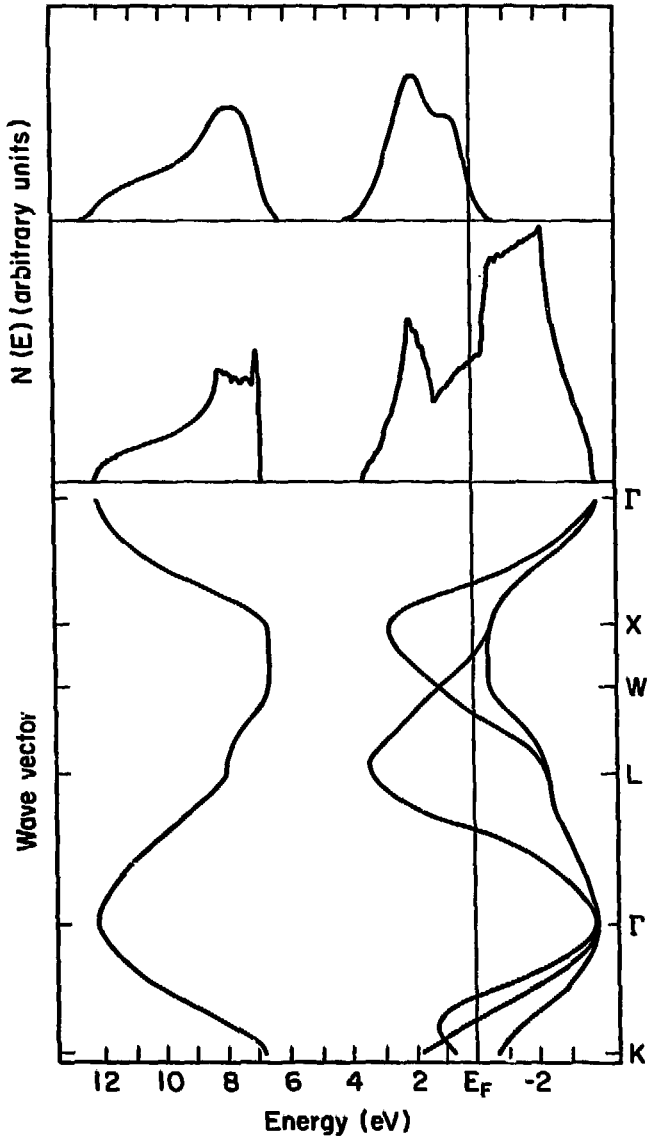

Fig. 3

XBL752-2326

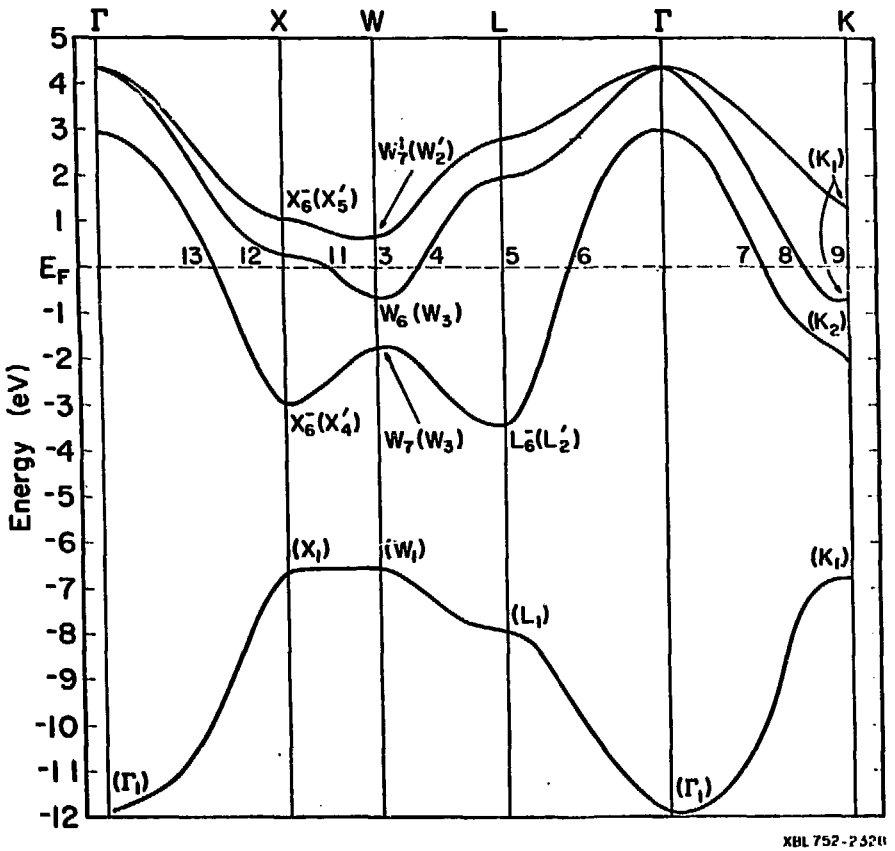
Γ
X
W
L
Γ
K
Energy (eV)
5
4
3
2
1
E_F
-1
-2
-3
-4
-5
-6
-7
-8
-9
-10
-11
-12
13
12
11
3
4
5
6
7
8
9
X_6^-(X_5')
W_7^1(W_2')
W_6(W_3)
X_6^-(X_4')
W_7(W_3)
L_6^-(L_2')
(K_1)
(K_2)
(X_1)
(W_1)
(L_1)
(Γ_1)
(Γ_1)
(K_1)
XBL 752-2320

Fig. 4

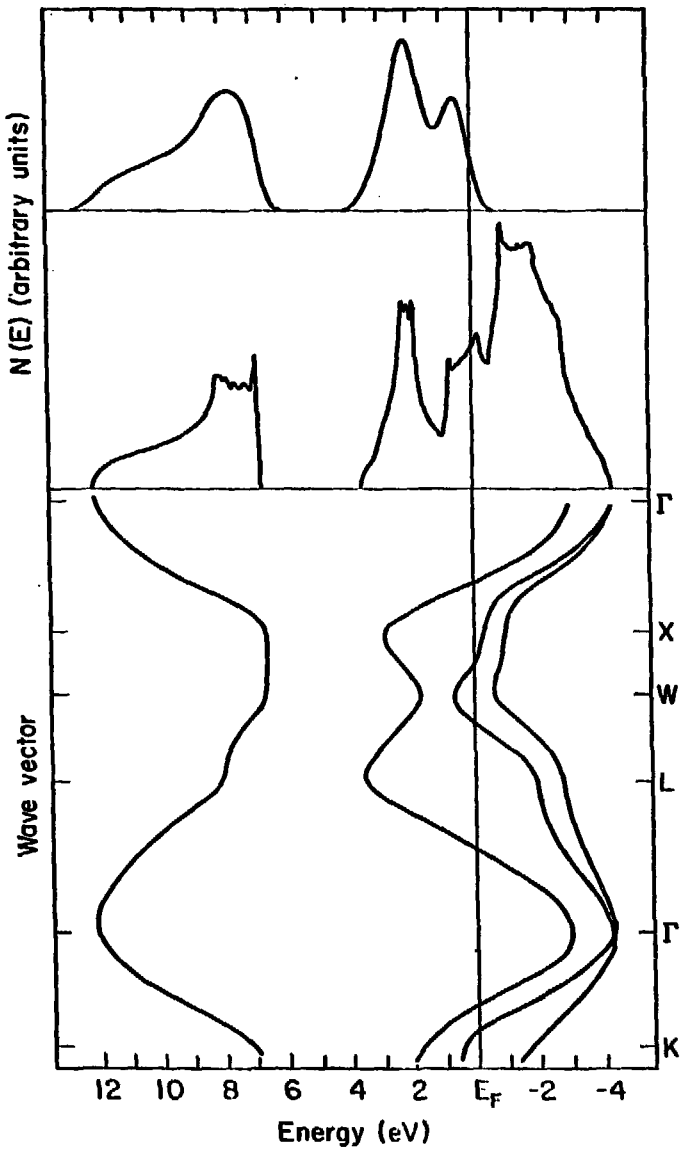

XBL752-2327

Fig. 5

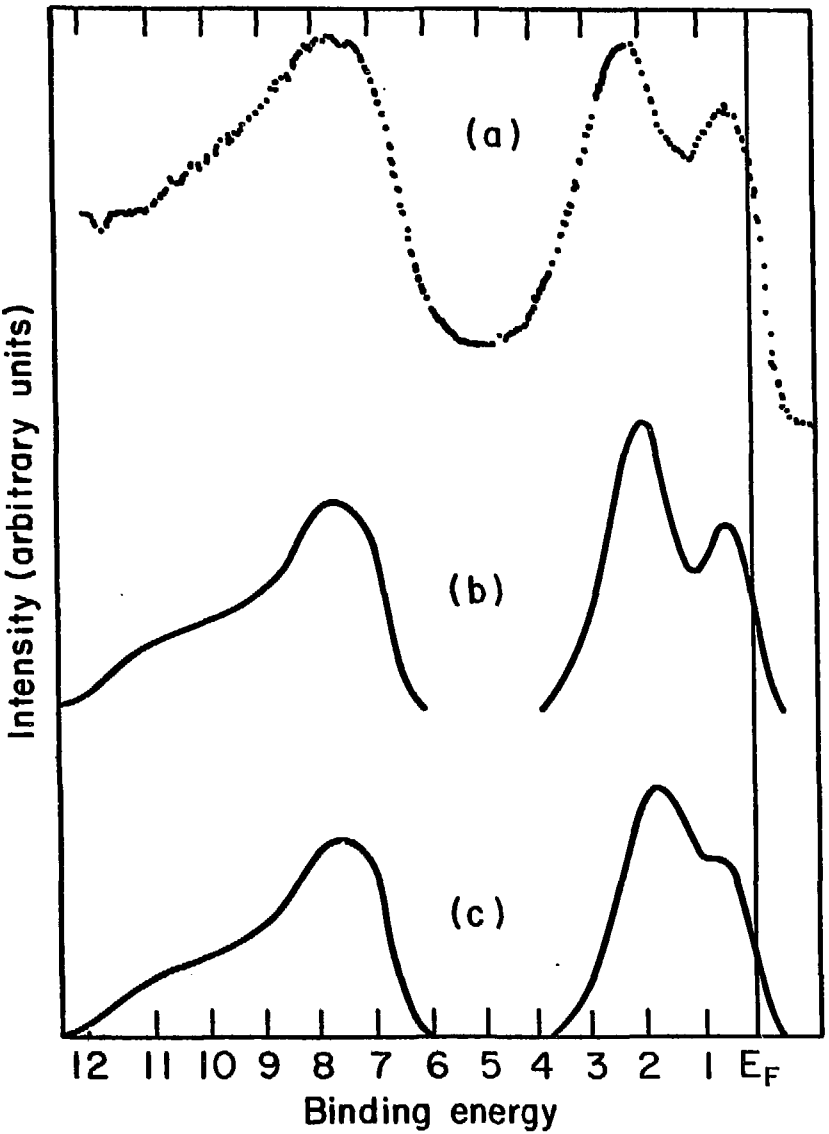

Fig. 6

XBL752-2324

ACKNOWLEDGEMENT

This work as done with support from the U. S. Energy Research and Development Administration.